

From Pleistocene Permafrost to Lena River Water – Organic Matter Characteristics using Biomarker Analysis and Isotope Hydrogeochemistry

Submitted by: Charlotte Haugk
Date: 28.06.2020

Supervision

1st supervisor Dr. Jens Strauss (Alfred Wegener Institute, Potsdam)
2nd supervisor Prof. Dr. Guido Grosse (University of Potsdam, Potsdam)
external supervisor Dr. Paul Mann (Northumbria University, Newcastle)



Table of content

LIST OF FIGURES.....	4
LIST OF TABLES	4
ABBREVIATIONS AND NOMENCLATURE	5
ABSTRACT	6
ZUSAMMENFASSUNG	6
1 INTRODUCTION	7
1.1 GENERAL BACKGROUND	7
1.2 AIMS AND GENERAL MOTIVATION	8
2 GEOLOGICAL AND GEOGRAPHICAL BACKGROUND.....	9
2.1 PERIGLACIAL ENVIRONMENT & PERMAFROST.....	9
2.2 YEDOMA.....	11
2.3 PERMAFROST DEGRADATION AND ORGANIC MATTER.....	11
2.4 NITROGEN CYCLING IN AQUATIC ENVIRONMENTS OF THE ARCTIC	12
2.5 REGIONAL SETTING: LENA DELTA AND SOBO-SISE ISLAND.....	14
3 METHODS.....	16
3.1 FIELD WORK.....	16
3.2 BIOGEOCHEMICAL PARAMETERS.....	19
3.3 BIOMARKERS	19
3.4 DISSOLVED ORGANIC CARBON	23
3.5 DENITRIFIER METHOD	24
3.5.1 ANALYSIS OF $\Delta^{15}\text{N}$ OF NITRATE (NO_3^-).....	25
3.5.2 ANALYSIS OF $\Delta^{15}\text{N}$ OF TDN	28
3.6 CALCULATING $\delta^{15}\text{N}$ OF DON.....	28
3.7 GEOCHRONOLOGY.....	29
3.8 DATA ANALYSIS AND STATISTICS.....	29
3.8.1 HIERARCHICAL CLUSTERING WITH R.....	30
3.8.2 SPEARMAN'S RANK CORRELATION.....	30
3.8.3 KRUSKAL-WALLIS-TEST	30
4 RESULTS	31
4.1 SEDIMENTOLOGICAL PARAMETERS.....	31
4.2 BIOMARKER PARAMETERS	33
4.3 WATER PARAMETERS	37
4.4 DISSOLVED ORGANIC MATTER	37
4.5 NITROGEN ISOTOPIC SIGNATURES	41
4.6 ORGANIC MATTER PROCESSING	43
4.6.1 OM OF SOBO-SISE CLIFF	43
4.6.2 OM DURING FLUVIAL TRANSIT	44
5 DISCUSSION	46
5.1 TERRESTRIAL FOCUS.....	46
5.1.1 DEPOSITIONAL ENVIRONMENT	46
5.1.2 ORGANIC MATTER QUALITY	47
5.1.3 OM AT THE PERMAFROST TO RIVER INTERFACE	49
5.2 AQUATIC FOCUS	50
5.2.1 WINTER SIGNAL IN THE LENA RIVER.....	50
5.2.2 NITROGEN PATHWAYS.....	52
5.2.3 IMPLICATIONS FOR THE ECOSYSTEM	55
5.2.4 FURTHER STUDIES	57

6	CONCLUSION	59
7	REFERENCES	60
8	APPENDIX	68
8.1	R-CODE FOR CLUSTERING	68
8.2	N-ALKANE PARAMETERS	70
8.3	N-FATTY ACID PARAMETERS	72
8.4	N-ALCOHOL PARAMETERS	73
8.5	WATER PARAMETERS, NITROGEN SPECIES AND NITROGEN STABLE ISOTOPES	74
8.6	STABLE WATER ISOTOPE DATA	75
8.7	DISTRIBUTION CPI AND ACL OVER CLIFF HEIGHT IN CLUSTER GROUPS	76
9	CERTIFICATE OF GOOD CONDUCT	77
10	ACKNOWLEDGEMENTS	78

List of Figures

FIGURE 1: CHANGE IN ANNUAL MEAN SURFACE TEMPERATURE	7
FIGURE 2: CROSS-SECTION OF A TYPICAL PERIGLACIAL ENVIRONMENT	9
FIGURE 3: PERMAFROST EXTENT AND DISTRIBUTION IN THE NORTHERN HEMISPHERE	10
FIGURE 4: OVERVIEW OF THE MARINE N CYCLE.....	14
FIGURE 5: STUDY AREA: OVERVIEW OF THE LENA DELTA BORDERING THE LAPTEV SEA	15
FIGURE 6: YEDOMA IC PROFILES STUDIED AT THE SOBO-SISE CLIFF	16
FIGURE 7: FROM: SAMPLING LOCATIONS CACOON ON ICE REPORT 2019.	17
FIGURE 8: IMPRESSIONS OF THE FIELD AND SAMPLING PROCEDURES DURING THE CACOON ON ICE.....	18
FIGURE 9: RELATIVE FREQUENCY OF N-ALKANE CHAIN LENGTH IN DIFFERENT ORGANISMS.....	20
FIGURE 10: SCHEMATIC OF LIPID BIOMARKER ANALYSIS.....	22
FIGURE 11: SCHEMATIC OF STABLE ISOTOPIC ANALYSIS.....	25
FIGURE 12: STEPS OF DENITRIFIER METHOD	27
FIGURE 13: SCHEMATIC OF HIERARCHICAL CLUSTERING	30
FIGURE 14: SOBO-SISE CROSS SECTION	31
FIGURE 15: OVERVIEW OF SEDIMENTOLOGICAL PARAMETERS.....	32
FIGURE 16: N-ALKANE CONCENTRATION.....	34
FIGURE 17: GC-MS CHROMATOGRAMS OF ANALYSED BIOMARKER COMPOUNDS	33
FIGURE 18: OVERVIEW OF BIOMARKER NSO FRACTION	35
FIGURE 18: SCATTERPLOTS FOR SELECTED ORGANIC MATTER DEGRADATION MARKERS.....	36
FIGURE 19: TEMPERATURE AND SALINITY PROFILES ACROSS ALL STATIONS	37
FIGURE 21: N SPECIES AND DOC TRENDS	39
FIGURE 21: SURFACE AND SECTION PLOTS	40
FIGURE 22: NITROGEN ISOTOPIC SIGNATURES AND TRENDS.....	42
FIGURE 23: CLUSTERING OF PERMAFROST SAMPLES AND RESULTING BOXPLOTS	43
FIGURE 24: BOXPLOTS FOR N SPECIES RESULTING FROM CLUSTER ANALYSIS	44
FIGURE 26: BOXPLOTS FOR N ISOTOPES RESULTING FROM CLUSTER ANALYSIS.....	45
FIGURE 26: TOC VARIATIONS FROM DIFFERENT YEDOMA STUDY SITES IN SIBERIA AND ALASKA	47
FIGURE 27: PERMAFROST THAW SIGNAL FOR N SPECIES	51
FIGURE 29: IMPRESSIONS FROM THE FIELD DURING THE CACOON ON ICE EXPEDITION	52
FIGURE 30: CHANGING NITROGEN EXPORT TO ARCTIC RIVERS.....	53
FIGURE 31: OVERVIEW OF NITROGEN CYCLING PATHWAYS AND FRACTIONATION PROCESSES	54
FIGURE 32: NITROGEN CYCLING PATHWAYS	55
FIGURE 32: ΔD OVER $\Delta^{18}O$ DIAGRAM OF RIVER WATER SAMPLES.	58
FIGURE 33: DON IN $\mu\text{G/L}$ AND NITRATE IN $\mu\text{G/L}$ OVER TRANSECT MOVING SEAWARDS.	58

List of Tables

TABLE 1: SOBO SISE CLIFF SAMPLING SCHEME OVERVIEW	16
TABLE 2: OUTCOME OF STATISTICAL TESTING WITH SPEARMAN'S CORRELATION COEFFICIENT.....	36
TABLE 3: NITROGEN AND CARBON SPECIES IN WATERS ALONG THE TRANSECT.....	38
TABLE 4: OVERVIEW OF ISOTOPIC SIGNATURES	41
TABLE 5: RESULTS OF KRUSKAL-WALLIS RANK SUM TEST FOR TERRESTRIAL SAMPLES.....	44
TABLE 6: RESULTS OF TWO SAMPLE T-TEST WITH UNEQUAL VARIANCES FOR N SPECIES	44

Abbreviations and nomenclature

Abbreviation/unit	Meaning
µg/l	microgram per litre
µM	Micro molar
‰	Parts per thousand/per mil
ACL	Average chain length
C	Carbon
CACOON	Changing Arctic Carbon cycle in the cOastal Ocean Near-shore
cal ka BP	calibrated kilo years before present
CPI	Carbon Preference Index
CTD	Conductivity, temperature, and depth sensor
DIN	Dissolved Inorganic Nitrogen
DOC	Dissolved Organic Carbon
DON	Dissolved Organic Nitrogen
ESAS	East Siberian Arctic Shelf
GC-MS	Gas Chromatography-Mass Spectrometry
HCl	Hydrochloric acid
IC	Ice Complex
IRMS	Isotope Ratio Mass Spectrometry
KPS	Potassium persulphate
LGP	Last Glacial Period
MAAT	Mean Annual Air Temperature
marl	Meters above river level
milliQ	Ultrapure water
ml	millilitre
N	Nitrogen
N ₂ O	Nitrous oxide
NED reagent	N-(-1-naphthyl)-ethylenediamine dihydrochloride solution
nmol	nanomole (10 ⁻⁹ moles)
NO ²⁻	Nitrite
NO ³⁻	Nitrate
O	Oxygen
OM	Organic matter
rpm	Revolution per minute
TDN	Total Dissolved Nitrogen
V-SMOW	Vienna Standard Mean Ocean Water
wt %	percentage by mass
µmol/l	Micromole per litre (10 ⁻⁶ moles per litre)

Abstract

Organic matter stored in permafrost represents one of the largest terrestrial carbon pools. This pool is especially vulnerable due to its susceptibility to thaw and mobilisation caused by climate warming across the Arctic. However, the amount and quality of the stored carbon (C) and nitrogen (N) as well as its composition during river transit is mostly unknown. The aim of this master's thesis is to characterize and define the source and fate of riverine C and N from the delta interior to the nearshore zone and its possible effect on primary productivity in Arctic coastal waters using a multi-proxy approach. Organic matter quality and degradation state of a rapidly degrading yedoma cliff in the central Lena Delta (Sobo Sise Island) was analyzed using lipid biomarker analysis. To grasp the winter thaw impact, a transect of water samples from the cliff going seawards were primarily investigated for N species and stable isotope composition using a hydrochemical approach. Laboratory analyses showed an overall high organic matter quality and a relatively low degradation state in yedoma deposits which suggests freeze-locking immediately after deposition. While the dominant winter water source was attributed mainly to supra-permafrost flow, it was found that dissolved organic nitrogen (DON) rather than nitrate is the main N species to be released into the riverine environment and was susceptible to alteration by remineralization and denitrification. Describing organic matter associated with thawing permafrost at the terrestrial-marine interface in a season-explicit study leads to a better understanding of C and N dynamics and thus the effects of a warming climate in Arctic environments.

Keywords: *Lena River, Arctic, Yedoma, DON, Laptev Sea, Nitrate, Dual isotope technique*

Zusammenfassung

Große Mengen an organischem Material, hauptsächlich Kohlenstoff (C) und Stickstoff (N), sind im Permafrost gespeichert und stellen aufgrund ihrer Anfälligkeit für Tauwetter und nachfolgender Mobilisierung durch die Klimaerwärmung einen der größten aber auch verwundbarsten der terrestrischen Kohlenstoffspeicher dar. Jedoch ist die Menge und Qualität des somit freigesetzten C und N sowie deren genaue Zusammensetzung während des fluvialen Transports weitgehend unbekannt. Das Ziel dieser Masterarbeit ist es die Quelle und den Stofffluss von C und N vom zentralen Delta bis zur küstennahen Zone und deren möglichen Auswirkungen auf die Primärproduktion in arktischen Küsten- und Schelfgewässern durch einen Multi-proxy-Ansatz zu charakterisieren. Ein rapid erodierendes Yedoma Kliff im Lena-Delta auf der Sobo-Sise Insel wurde untersucht um die Qualität der organischen Stoffe und den Degradationszustand mittels Lipider Biomarkeranalyse zu bewerten. Des Weiteren wurde eine Abfolge von Wasserproben, beginnend am Kliff und sich weiter fortsetzend in die Laptev See, auf N-spezies und stabile Isotopenzusammensetzung mit einem hydrochemischen Ansatz untersucht. Laboranalysen zeigen eine hohe Qualität und relativ niedrige Degradation des organischen Materials für das Yedoma Kliff, was auf direktes Einfrieren direkt nach der Ablagerung hinweist. Während die vorherrschende Wasserquelle im Winter hauptsächlich einem Supraperafrost-Strom zugeschrieben wird, wurde festgestellt, dass gelöster organischer Stickstoff (DON) anstatt Nitrat die vorherrschende Stickstoffquelle ist. DON wird in der Flussumgebung freigesetzt und ist hier anfällig für Veränderungen durch Remineralisierung und Denitrifikation. Die detaillierte und saison-explicite Untersuchung organischen Materials assoziiert mit auftauenden Permafrostböden an der terrestrisch-marinen Schnittstelle führt zu einem besseren Verständnis der C- und N-Dynamiken im Kontext der Klimaerwärmung in arktischen Lebensräumen.

1 Introduction

1.1 General Background

Global warming is enhancing greenhouse gas emissions into the atmosphere, a process leading to further warming. According to the Intergovernmental Panel on Climate Change the global mean surface temperature will be increasing until the end of the 21st century (2081-2100) and will likely be in the range between 1.5 and 2.0°C due to an increased greenhouse effect (Pachauri et al., 2014).

Polar Regions are expected to warm approximately twice as much compared to the global mean (Figure 1). This process is called polar amplification. The Arctic is especially vulnerable to climate change as large areas are underlain by permafrost and therefore an area of rising scientific interest. Changes affect all components of the Arctic ecosystem and have consequences to their geomorphological, hydrological and biological processes from a local to regional scale with possible global impact.

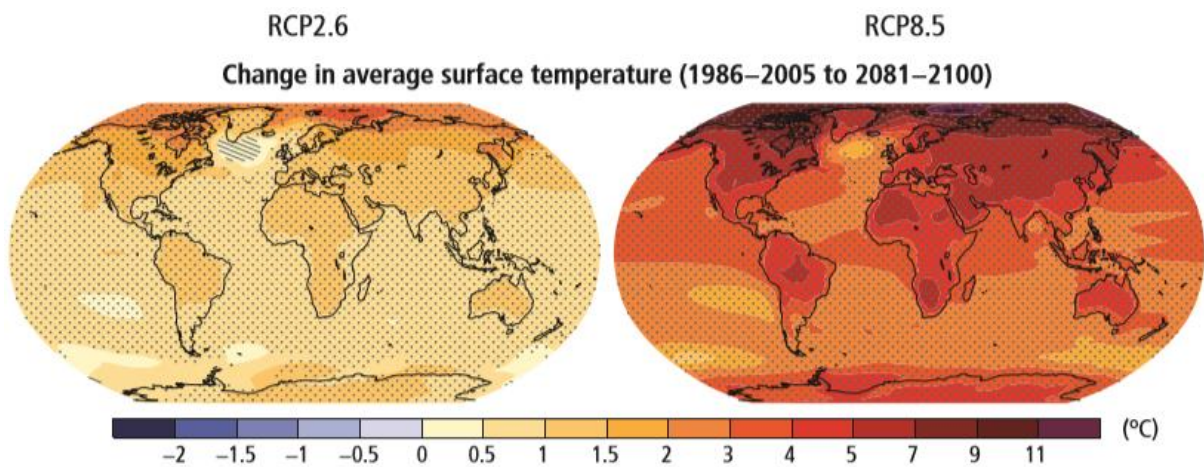


Figure 1: Change in annual mean surface temperature based on modelled projections for 2081-2100 in comparison to 1986-2005. RCP2.6 – warming scenario with rigorous mitigation strategies and RCP8.5 –warming scenario with extremely high greenhouse gas emissions. From (Pachauri et al., 2014)

Arctic rivers annually carry ~13% of all dissolved organic carbon transported globally from land to ocean, despite the Arctic Ocean making up only approximately 1% of the total global ocean volume (Holmes et al., 2012). This makes the Arctic Ocean the most riverine influenced on the planet. Rivers that carry large loads of nutrients, organic matter and ions to coastal areas, discharge onto an extensive Arctic continental shelf area. Those are characterised by a low salinity surface layer above more saline deep water from the Atlantic (Tank et al., 2012; Thibodeau et al., 2017). The largest shelf system in the Arctic Ocean is the East Siberian Arctic Shelf (ESAS) comprising the Laptev Sea, the East Siberian Sea and the Chukchi Sea.

Warming air and sea water temperatures are extending both the thaw and open water season as well as increasing erosion of ice and carbon rich deposits (Günther et al., 2013). This results in an increase of Arctic river discharge (Holmes et al., 2012) transporting organic-rich waters to the nearshore. Very ice-rich permafrost deposits such as the yedoma Ice Complex (Schirrmeister et al., 2013; Strauss et al., 2017) are particularly at risk to rapid, strong thaw processes and erosion (Fuchs et al., in review). Additionally, estimations yield that almost twice as much carbon is locked in the permafrost region than there is currently in the atmosphere (Hugelius et al., 2014). Total estimated Soil Organic carbon (SOC) storage for the permafrost region is ~1300 Pg with 181 ± 54 Pg attributed to Yedoma regions below 3m depth (Strauss et al., 2013; Hugelius et al., 2014). Sedimentary input from coastal erosion and river to

the Arctic nearshore zone and shelf areas have been reported to rise significantly in the past decades (Holmes et al., 2012). However, the importance of the nearshore region, consisting of several tightly connected ecosystems including rivers, deltas, estuaries and the continental shelf is often overlooked. Moreover, seasonally-explicit studies are lacking, severely limiting our ability to predict the impact of shifting seasonality (Strauss & Mann, 2018).

Although there has been considerable research into the effects of permafrost thaw on organic matter and carbon fluxes (e.g. Frey et al., 2007; Vonk et al., 2013; Mann et al., 2015), there are fewer studies on nitrogen fluxes in Arctic rivers and fewer still on cycling processes. However, nitrogen acts as a limiting factor for primary productivity in the coastal Arctic. While the mean riverine nitrate contribution to ocean primary production is generally low in the Arctic with about 5% in the Laptev Sea (Le Fouest et al., 2013), rapid uptake of dissolved inorganic nitrogen (DIN) coupled with relatively high rates of DON regeneration in N-limited nearshore regions could potentially lead to high rates of localized riverine-supported photosynthesis (Tank et al., 2012).

Dissolved organic Nitrogen (DON) represents a 5 times greater influx to Arctic shelf waters from rivers than nitrate across the entire Arctic but 70% of the DON is removed in shelf waters before reaching the open marine environment. The processes involved in this removal are largely unclear (Thibodeau et al., 2017). Stable isotopes of nitrate can be used to determine some of the processes affecting the nitrate concentration of the river. It is important, therefore, to understand how permafrost degradation may impact nitrogen species from delta to nearshore environments and subsequently address potential changes to the riverine and coastal nitrogen cycle.

As part of the CACOON project (Changing Arctic Carbon cycle in the cOastal Ocean Near-shore), this thesis investigates organic matter characteristics of permafrost in the Lena Delta and contributes to quantifying future effects of terrestrial thaw on aquatic nearshore ecosystems in the Laptev Sea.

1.2 Aims and general motivation

Getting a step closer to define source and fate of riverine carbon and nitrogen and its potential effect for primary productivity in Arctic riverine to nearshore waters will lead to better understanding of the nutrient load associated with permafrost thaw, and thus warming climate in Arctic environments. This general motivation in mind I aim to investigate the role of permafrost degradation on changing riverine dissolved organic matter, represented here with an example from the Lena Delta, Siberia. In short, the three major objectives of my thesis are:

- 1) **Terrestrial Focus:** Characterising organic matter of permafrost by lipid biomarker analysis to define potential source (i) and assess quality of stored organic matter (ii)
- 2) **Aquatic Focus:** Characterising nitrogen isotope signals at a seasonal snapshot to relate carbon and nitrogen compounds to permafrost as potential source and (iv) to find out nitrogen transformation processes in permafrost thaw zones (v)
- 3) Providing a **seasonal snapshot of winter organic matter characteristics** (iii) and fluxes in the Lena Delta by investigating the distribution of organic matter.

2 Geological and Geographical Background

2.1 Periglacial environment & permafrost

Periglacial means “around glaciated areas” (greek: *peri* – around; latin: *glacies* – ice). Periglacial environments are characterized by freeze-and-thaw cycles of the ground. Permafrost is one of the striking features of the periglacial environment. Permafrost occurs in non-glaciated Arctic and Antarctic regions, as well as in alpine regions that provide mean annual temperatures below 0 °C. Depicted in Figure 2 and Figure 3 are permafrost distribution and extent in the Arctic and a cross section of a periglacial environment, respectively. Following Zhang et al. (2000) approximately 22% of the exposed land area on the Northern Hemisphere is underlain by permafrost. Permafrost conditions are influenced e.g. by topographic features, snow cover, vegetation, moisture content of the ground and subsurface material (see Figure 3(a) by Overduin et al., (2020) for color-coded permafrost distribution). Depending on the percentage of coverage, permafrost can occur as

- **continuous** (90-100% area coverage); this type dominates in high latitudes of the Northern Hemisphere and has mostly been formed during or before the last glacial period
- **discontinuous** (50-90%); characterized by bodies of frozen ground which are separated by areas of unfrozen ground
- **sporadic** (10-50%); can be either relict permafrost currently in degradation or young permafrost formed during the last thousands of years
- or **isolated** (<10%); which means patches of frozen ground in an unfrozen area that often occurs beneath peaty organic sediments and is the result of advanced degradation.

At the surface lies the active layer, which is seasonally unfrozen and can vary in thickness from a few centimetres to several meters (Schuur et al., 2008). The active layer covers the perennial frozen permafrost, where the temperature stays below 0°C all year. The temperature profile of permafrost shows seasonal variation down to the depth of zero annual amplitude. Below this depth, the temperature profile is influenced by the geothermal gradient. The permafrost base is located at the point where the mean annual temperature is above 0°C. Permafrost can reach as deep as approximately 1450 m below surface in Eastern Siberia (Kitover et al., 2016). According to Mackay (1990), permafrost can form in two ways: Epigenetic permafrost occurs when the ground is exposed to perennial freezing after its formation, also called downward freezing. In contrast to that, syngenetic permafrost is formed during sedimentation, which means the formation happens at the same time as deposition of soil material takes place.

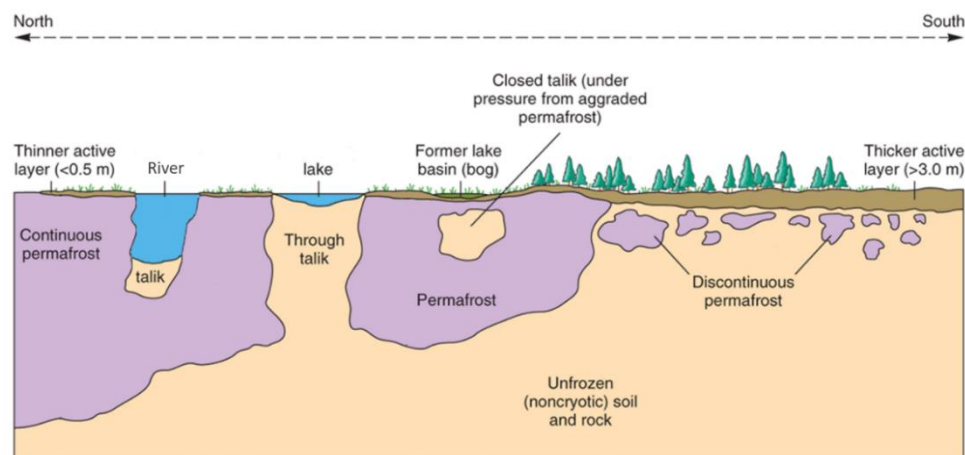
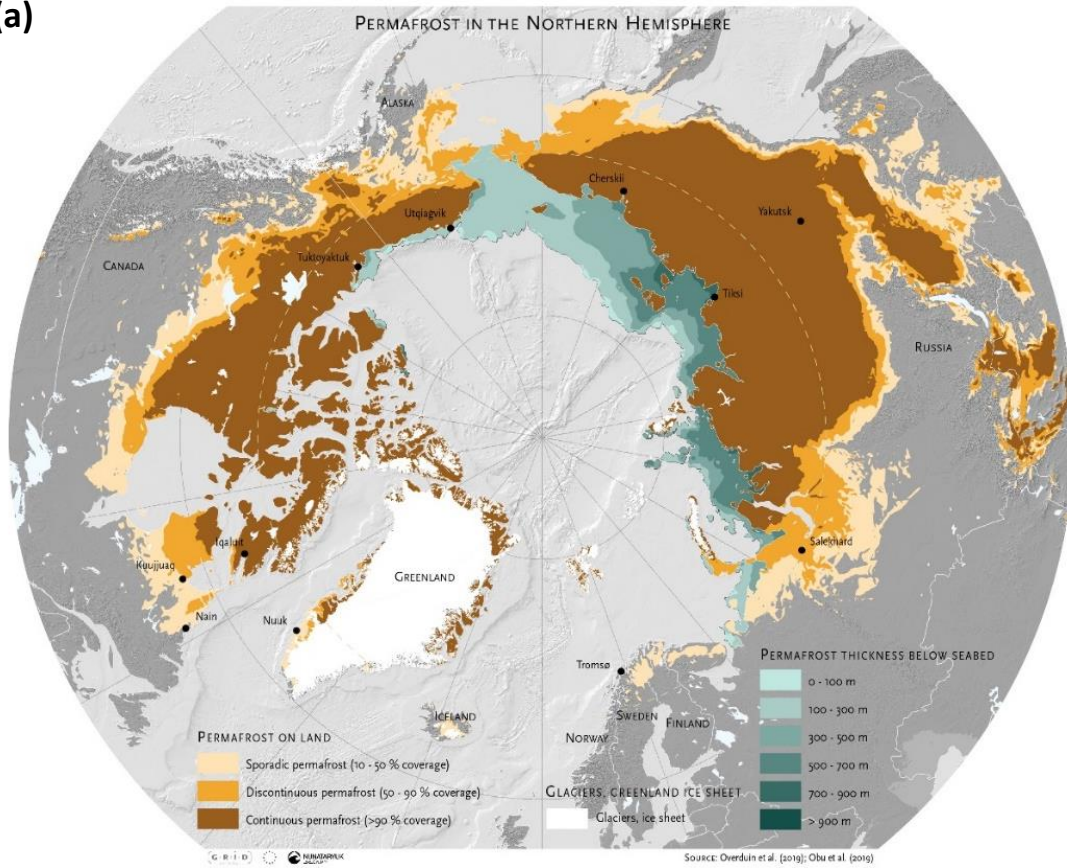


Figure 2: Cross-section of a typical periglacial environment, after (Christopherson, 1997).

(a)



(b)

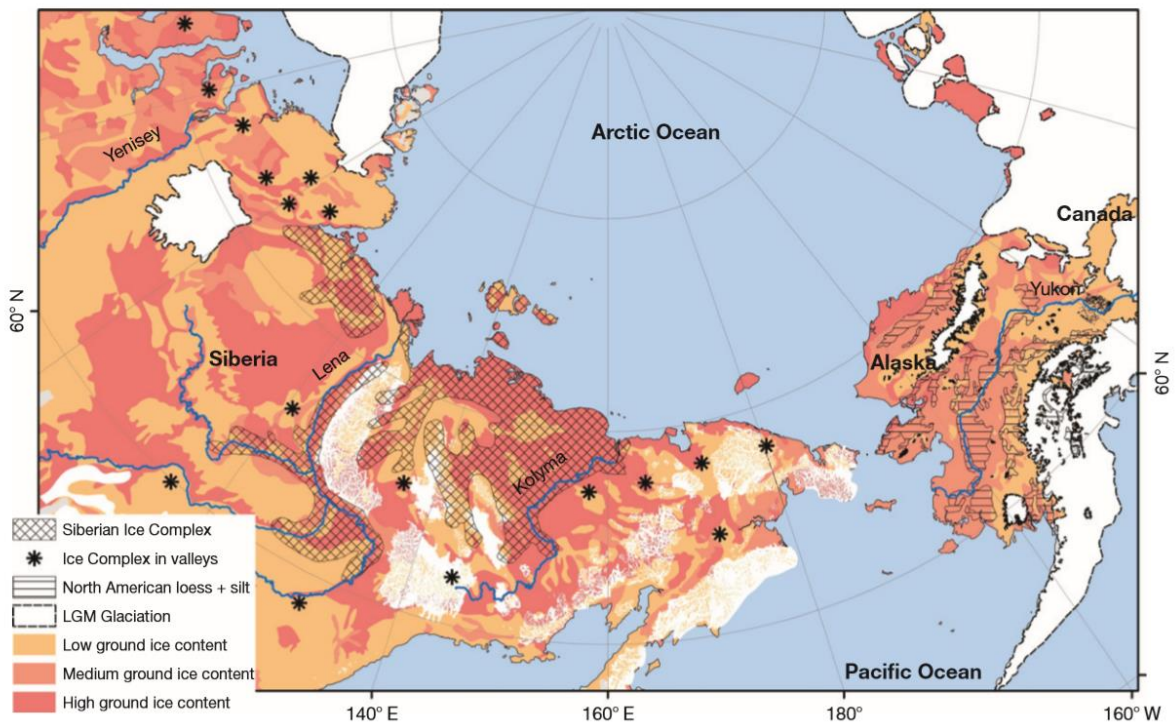


Figure 3: (a) Permafrost extent and distribution in the Northern hemisphere, also showing regions of mountain permafrost, from (Overduin et al., 2020). (b) Distribution of ice-rich permafrost deposits (Yedoma) in Arctic and Subarctic lowlands in the region of late Pleistocene Beringia adapted from Schirmer et al (2013).

Ground ice is another characteristic used to classify permafrost: ground containing >25 vol% ice is called ice-rich permafrost and <25 Vol% is called ice-poor (Brown et al., 1997). It can occur in form of ice wedges, pore ice, segregated ice or intrusive ice. Intrusive ice results from the intrusion of water under soil water pressure and occurs as sill or pingo ice (French, 2017). Segregated ice expresses as ice layers or lenses which can be from a few millimetres to tens of meters thick. When pore water freezes in situ, it is referred to as pore ice. Repeated thermal contraction cracking and infill of water in repeated freeze-and thaw-cycles can lead to the formation of ice wedges (Lachenbruch, 1963). They form superficially visible polygonal networks that are very characteristic features of periglacial environments.

2.2 Yedoma

Yedoma is a term used for ice-rich permafrost (50-90% in volume) that contains a substantial quantity of organic matter. Extensive parts of Alaska and Siberia are covered by Yedoma deposits (Strauss et al., 2017) and the Yedoma region is calculated to reach about 1 387 000 km² (Strauss et al., 2013). The Yedoma itself is subsequently formed during repeated cycles of concurrent sediment accumulation, ground ice segregation, syngenetic ice wedge growth, peat aggradation, cryosol formation and cryoturbation (Schirrmeister et al., 2008). It can be dated back to >55 ka BP and continued to 12 ka BP (Schirrmeister et al., 2013). It is assumed that the cycles are varying in intensity on a spacial scale.

Yedoma genesis was under scientific debate for a long time. Recent publications on this have in common that a polygenetic deposition of sediment from more local sources was deposited on a vast accumulation plains with low topographic gradients. The deposition mechanisms is expected involve at least alluvial, fluvial and partly aeolian transport, as well as in-site frost weathering (Schirrmeister, 2012; Schirrmeister et al., 2013, 2017; Murton et al., 2015). Yedoma can reach up to 50 m in thickness and contain tall and wide ice wedges, which measure up to 3-4 meters in width on ground level (Kanevskiy et al., 2011). The term Ice Complex is also used widely to describe Yedoma, which stands for a high ice content of such deposits. As there are more Ice Complexes besides Yedoma, however for simplicity, in this thesis will Ice Complexes will be referred to as Yedoma. An overview of Yedoma and the distribution of ice-rich permafrost deposits Figure 3 in Arctic and sub-arctic lowlands from Schirrmeister et al (2013).

2.3 Permafrost degradation and organic matter

Permafrost thaw generally can lead to a number of transformation processes that reshape the landscape and are especially significant at the land to ocean interface. Along permafrost-dominated coasts, heat transfer and melt of ground ice is added to the mechanical erosion forces of waves and ice (Günther et al., 2013), which is referred to as thermo-erosion. Thermo-erosion includes two related processes that work temporally and quantitatively differently together: thermo-denudation (thawing of exposed permafrost with propagation of a retreating headwall influenced by insolation and heat flux) and thermo-abrasion (defined as the combined action of mechanical and thermal energy of sea water at water level) (Günther et al., 2015). This is of great importance for Yedoma regions since a large share of those deposits are located in coastal areas. The same processes are acting in permafrost dominated river systems. On Sobo-Sise Cliff, fluvio-thermal river bank erosion is taking place meaning mechanical erosion by an unfrozen river against ice-rich soils and sediments are combined with thermal erosion and thaw of permafrost, sometimes causing parts of the river bank to collapse into the river.

Currently, approximately 70% of the Yedoma region is affected by thermokarst degradation (Strauss et al., 2013). Thermokarst is defined as process by which characteristic landforms result from the thawing of ice-rich permafrost or the melting of massive ice (Morgenstern et al., 2011). One of those landforms are thaw lakes, also referred to as thermokarst lakes. They generate in closed depressions (Allasses)

formed by lake water induced settlement of ground, following thawing of ice-rich permafrost or massive ground ice (Van Everdingen, 2005). Talik formation is a fundamental process of thermokarst lake development. A talik is defined as a layer or body of unfrozen ground occurring in a permafrost area due to a local anomaly in thermal or hydrological conditions. Taliks can form during thermokarst lake cycle or due to top-down thaw processes. They can occur by active layer deepening, where the top layer of the soil becomes deeper due to increased summer temperatures. This increases the depth of the active layer-frozen ground margin. If active layer deepening increases in magnitude to such an extent that the soil does not completely refreeze in the winter, then a talik is formed. A talik is defined as a residual soil layer that remains unfrozen with freezing conditions present around (van Everdingen, 1976). It has a high moisture content and heat capacity so is favourable for degradation processes. Active layer deepening and talik formation are gradual processes, but some degradation processes can be much more rapid. This can occur, when there is a high ice content present, which can potentially be melted and can cause dramatic volume losses. For these rapid processes we need a high ice content, which can be melted, which cause dramatic volume loss.

As mentioned above, Yedoma is very ice-rich permafrost deposit, which makes it more vulnerable to rapid and strong thaw erosion (Günther et al., 2013) or surface subsidence, called thermokarst (Olefeldt et al., 2016). With subsidence and lake formation on top, permafrost is exposed even more to the atmosphere, promoting a positive feedback cycle of more permafrost thawing in thermokarst affected areas. Rapid and sometimes dramatic thaw events can occur through the collapse of permafrost when exposed to riverbank or coastal erosion. More importantly, the organic carbon freeze-locked in Yedoma is decomposable after thaw (Strauss et al., 2013; Vonk et al., 2013). The main source of OM stored in Yedoma deposits is late Pleistocene vegetation. Its origin, biogeochemical composition, and state of preservation determine the OM vulnerability (Strauss et al., 2017). The estimated carbon content of Yedoma by Zimov et al., (2006) and Schirrmeister et al., (2008) is thought to reach between 2-5 weight percent TOC (total organic carbon values). Strauss et al. (2013) calculates that the total Yedoma region contains 211 + 160/ -153 Gt of organic carbon (OC), excluding the active layer and deeper OM deposits below Yedoma or below frozen thermokarst deposits. Considering this, thawing of Yedoma can be a significant source of greenhouse gas emissions (Schneider von Deimling et al., 2015), due to deep thermokarst caused degradation.

2.4 Nitrogen Cycling in aquatic environments of the Arctic

The Arctic Ocean contains only 1% of global ocean volume but receives 10% of the total global riverine discharge (Holmes et al., 2012). This unique situation together with the large amount of shelf area of the Arctic Ocean results in estuarine like conditions throughout most of its area (Francis, 2019). This is characterised by a low salinity surface layer above more saline deep water from the Atlantic (Tank et al., 2012). Especially close to the river mouth like in the bigger study area of this thesis, there is a freshwater lense above salt water (CACOON Spring Expedition Report - Strauss et al., 2019). Any changes in riverine biogeochemistry will most likely have significant implications on marine chemical, physical and biological processes of the Arctic Ocean (Holmes et al., 2012).

Nitrogen (N) is a major nutrient required for biological productivity, and its availability can limit primary production on a variety of spatial and temporal scales (Casciotti, 2016). It exists in many different forms in aquatic environments. The most abundant one N_2 is not bioavailable to the majority of primary producers. In aquatic environments, nitrogen appears as dissolved inorganic nitrogen (DIN) in forms of nitrate, nitrite and ammonium. The DIN value is calculated as the sum of these three forms (McCrackin

et al., 2014). These forms are biologically available and can be taken up by primary producers (Tank et al., 2012). Nitrite and ammonium are highly unstable and so only persist for a short time before being converted into nitrate or assimilated. Hence, the principal form of fixed N is nitrate (NO_3^-), which accounts for ~88 % of the marine N reservoir (Gruber, 2008).

TDN describes all dissolved nitrogen phases: Dissolved inorganic nitrogen (DIN) and dissolved organic nitrogen (DON). The organic form of nitrogen (DON) can be amino acids in proteins, nucleotides etc. but for uptake by species, it has to be broken down/remineralized into DIN (Tank et al., 2012). DON can be calculated as the difference between TDN and DIN (Frey et al., 2007):

$$[DON] = TDN - (\text{NO}_3^- + \text{NO}_2^- + \text{NH}_4^+)$$

Equation 1

However, as discussed above, nitrate is expected to be the dominant species in aquatic environments, so the calculation can be simplified to:

$$[DON] = TDN - \text{NO}_3^-$$

Equation 2

Most of the biological production converting inorganic carbon and nutrients to OM, is happening in the upper surface ocean penetrated by sunlight. The majority of this organic matter is remineralized (or nitrified) back into dissolved N species within the euphotic zone, but a small proportion of organic matter is exported to the subsurface (Tuerena, 2015). Through the process of biological fixed-N uptake and organic matter export, there is an accumulation of NO_3^- with depth and a depletion of NO_3^- within surface waters (Tuerena, 2015). To fill the depleted surface layers, NO_3^- is physically recirculated from deeper layers of the ocean. This loop is also called “carbon-pump” and the main responsible mechanism for carbon fixation in the ocean from the atmosphere.

Figure 4 gives an overview of the aquatic nitrogen cycle. Atmospheric deposition via e.g. rainfall can transfer N to the river and to the ocean. There are two major processes that are influencing the fixed N budget: N_2 – fixation or anaerobic ammonium oxidation (anammox) and N – loss (denitrification). During N_2 fixation, N_2 is reduced to ammonia, which is utilised for production and growth. Denitrification occurs in low oxygen environments. Here oxygen is replaced by nitrate as the electron acceptor, reducing NO_3^- to N_2 which is unavailable to most phytoplankton. This process occurs both in anoxic conditions and in sediments. However, the described cycle holds true for nitrogen dynamics in the open ocean and shelf area. This particular study is investigating a river transect in an estuary environment of the Lena Delta. In the coastal Arctic Ocean, currently all production is limited to a brief bloom period in summer where all the nitrogen is consumed (Thibodeau et al., 2017). This means that arctic shelf areas are N-limited. Mean riverine nitrate contribution to ocean primary production is generally low in the Arctic with about 5% in the Laptev Sea (Le Fouest et al., 2013). However, rapid uptake of DIN coupled with relatively high rates of DON regeneration in N-limited nearshore regions could potentially lead to high rates of localized riverine-supported photosynthesis (Tank et al., 2012).

As part of the nitrogen cycle, exchange between nitrogen pools can occur in riverine and coastal areas depending on the external environmental conditions. The analysis of nitrogen isotopes is vital in this study to help determine cycling and source processes. Specifically, nitrogen and oxygen isotopes of dissolved nitrate ($\delta^{15}\text{N}\text{-NO}_3^-$ & $\delta^{18}\text{O}\text{-NO}_3^-$), and nitrogen isotopes of TDN and DON ($\delta^{15}\text{N}\text{-TDN}$ & $\delta^{15}\text{N}\text{-DON}$) were utilised.

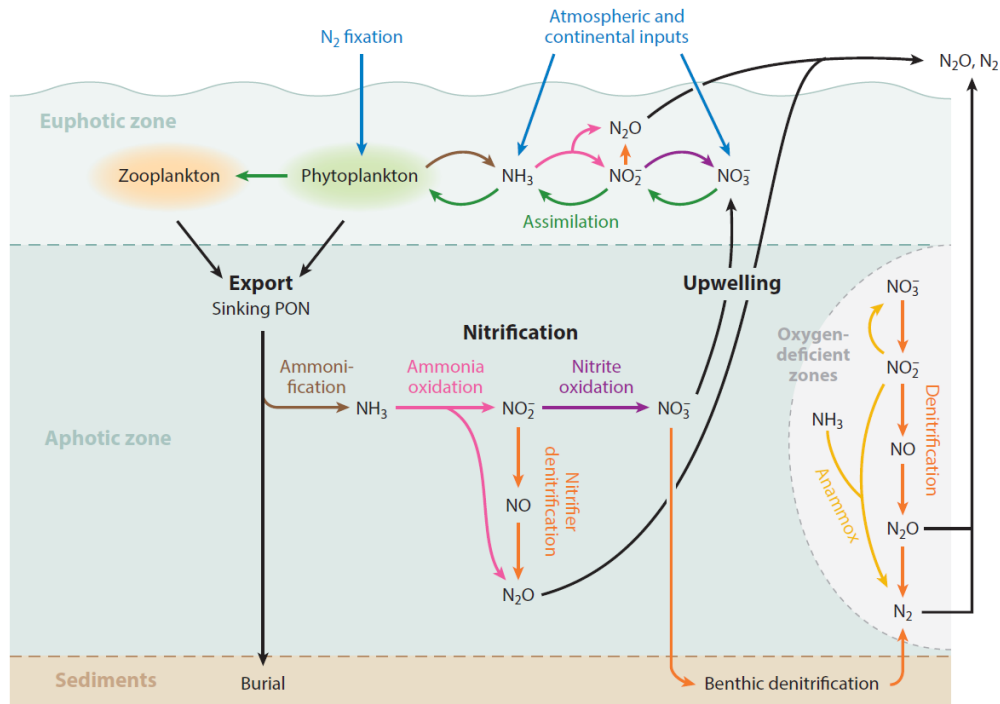


Figure 4: Overview of the marine N cycle featuring important processes in the water column after Casciotti (2016).

2.5 Regional Setting: Lena Delta and Sobo-Sise Island

The Lena River has the largest delta in the Arctic with an area of $3.2 \times 10^4 \text{ km}^2$ (Gordeev & Shevchenko, 1995). The Lena has a mean annual discharge of $525 \text{ km}^3/\text{yr}$, the second highest in the Arctic. The Baikal Mountains being the source area, the Lena River flows through a large part of Siberia to the north and discharges into the Laptev Sea. According to Grigoriev, (1993), the Lena Delta can be subdivided into three geomorphological units. The first unit is characterised by ice-wedge polygonal tundra, large thermokarst lakes and active flood plains. Formed during the Holocene, it occupies most of the central and eastern parts of the delta. The second unit comprises sandy sediments with low ice content and many large thermokarst lakes, and occurs in the north-western part of the delta; it was formed between the Late Pleistocene and early Holocene. The third and oldest unit is the above-mentioned Yedoma, an erosional remnant of a Late Pleistocene plain consisting of fine-grained, organic-rich and ice-rich sediments, characterised by polygonal ground and thermokarst processes. Although yedoma is located in the delta, it has been there before the delta formed.

Sobo-Sise Island is located on the third unit and in the Siberian zone of continuous permafrost which is characterized by late Pleistocene, ice rich yedoma deposits (Schwamborn et al., 2002). The terrain is affected by rapid thermokarst processes (Nitze & Grosse, 2016) and surface subsidence (Günther et al., 2013). According to the landform classification by Fuchs et al., (2019) where they investigated Sobo-Sise Island and Bykovsky Peninsula, 43% of the land surface are occupied by Yedoma uplands and Yedoma slopes, 43% are thermokarst basins and 14% are lakes. On Sobo-Sise Island, shoreline retreat is at a remarkably fast rate: $20\text{m}/\text{yr}$ based on Landsat data detected between 2000-2013 by Nitze & Grosse (2016).

The Sobo-Sise Cliff (72°32 N, 128°17 E) is located on Sobo-Sise Island, which sits in the eastern part of the delta between two of the main channels: Sardakhskaya and Bykovskaya channel. The island stretched 45 km in east–west direction and has an area of total 336 km² (Fuchs et al., 2019). The Cliff stretches 1,660 m and is facing north to the Sardaskhskaya channel (Figure 5), which has a water discharge of ~8000 m³/s (Fedorova et al., 2015).



Figure 5: Study area: overview of the Lena Delta bordering the Laptev Sea. The red triangle represents Sobo-Sise Cliff with main channels visible. Cliff face during ice free season in the background. Map from (Fuchs et al., in review).

Climate on Sobo-Sise Island is characterized as continental, despite the close proximity to the coast. . Peel et al. (2007) also mentioned the influence of polar tundra climate. The tundra vegetation can be described as sparse and limited by a short growing season from June to September (Fuchs et al., 2019). The vegetation composition is dominated by sedges, grasses, mosses, lichen, and sporadic dwarf shrubs (*Salix* species). On Samoylov Island (the closest weather station around 50 km to the west) the mean annual air temperature (MAAT) is -12.5 °C and the approximate mean annual precipitation is 180–200 mm including mean summer rainfall and mean snow water equivalent (between 1998–2011, after Boike et al., 2012). The landscape is covered by snow and ice for the greater part of the year. The Lena River is ice-covered for about 8 months (October - May) during winter time. Ice thickness on the Lena River is up to 2 m while the water depth at the onset of the Sardakhskaya channel can reach 22 meters (Fedorova et al., 2015) and around 11 meters in front of Sobo-Sise Cliff allowing constant water flow underneath also in winter (Fuchs et al., in review).

3 Methods

To answer the three overarching scientific questions of my study I investigated two datasets

- i) terrestrial samples of 3 permafrost cores were analysed for lipid biomarkers and
- ii) a transect of water samples were analysed for nitrogen compounds and their isotopic composition.

3.1 Field Work

The field work on Sobo Sise Island took place from 11 July to 25 July 2018 as part of the LENA 2018 expedition of AWI Potsdam. The Yedoma Ice Complex (IC) stretching 24.2 m above river level (arl) was cryolithologically described and sampled by repelling down on a rope from the top of the cliff (Figure 6). Three overlapping permafrost sections of the IC were sampled (SOB18-01: 24.1 to 15.7 m arl, SOB18-03: 18.2 to 10.2 m arl and SOB18-06: 13.4 to 0.9 m arl), where the first two were sampled close together but SOB18-06 approximately 100 m further east (Figure 14). 61 sediment samples were collected, where 28 were chosen for biomarker analysis (see Table 1).

Table 1: Sobo Sise Cliff sampling scheme overview - Three permafrost sections were taken to cover the length of the cliff: SOB18-01, SOB18-03 and SOB18-06 all of them analysed in this thesis.

Core ID	Landscape Unit	Coordinates	Sample amount
SOB18-01	Yedoma IC	72.53877 °N, 128.27983 °E	10
SOB18-03	Yedoma IC	72.53877 °N, 128.28012 °E	5
SOB18-06	Yedoma IC	72.53812 °N, 128.28267 °E	13
Total			28

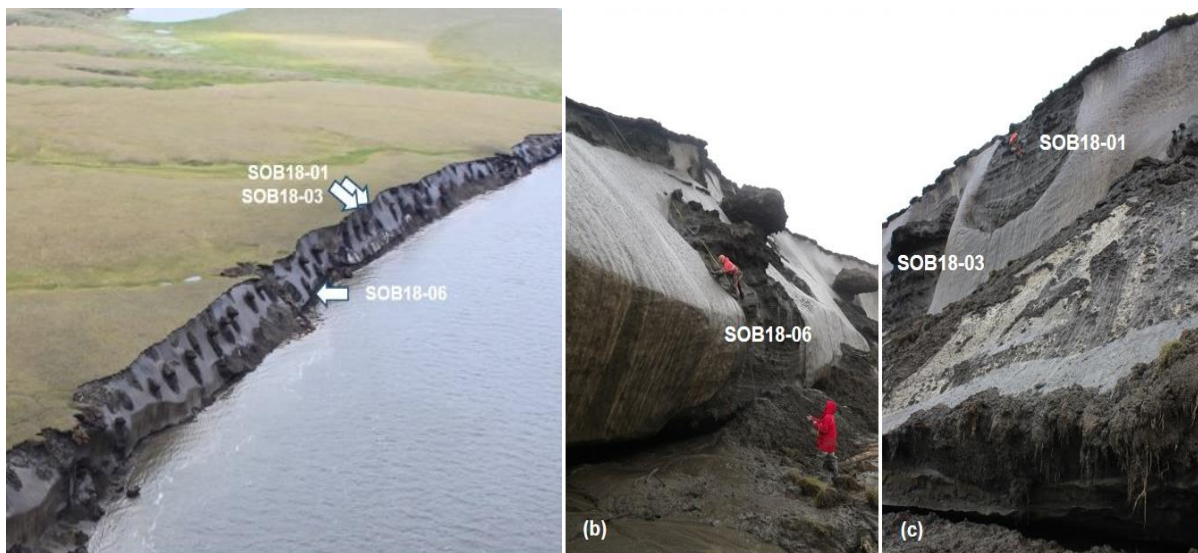


Figure 6: Yedoma IC profiles studied at the Sobo-Sise cliff shown as (a) overview with the thermoerosional valleys incising the Yedoma cliff and draining into the Lena River, (b) detail of SOB18-06, (c) detail of SOB18-01 and SOB18-03 (Wetterich et al., 2018).

In the Sardakhshaya channel of the Lena River and during the CACOON on Ice field campaign from 26th of March to 10th April 2019, water samples were taken from ice core holes using a water sampler. The plan was to sample an approximately 100 km transect with 12 sites east to west over 9 field days from the Lena channel to the open shelf. However, there appeared to be an unbreachable crack (72.5255°N; 129.8648°E) to the north and to the east of approximate 5m width with very thin ice to open water

(Figure 8), where the expedition participants were not able to do the transect on the shelf. Adapting to this situation, the alternative sampling strategy was now to sample upstream to a heavily eroding permafrost cliff ~40 km upstream the Sardakhshaya channel with sampling locations every 5 km as shown in Figure 7 (CACOON on Ice Expedition Report, Strauss et al., 2019).

Immediately after the water was sampled, the work continued in the provisional laboratory (Balok) where the water was filtered and decanted into pre-cleaned HDPE bottles. The 13 samples (Table 3) were taken first to Northumbria University facilities, where they were frozen for storage. In early December 2019 they were unfrozen again to be shipped to the laboratory facilities at the University of Edinburgh to undergo analysis of stable isotopic composition. CTD measurements were conducted using a handheld Sontek™ CastAway conductivity, temperature, and depth (CTD) sensor.

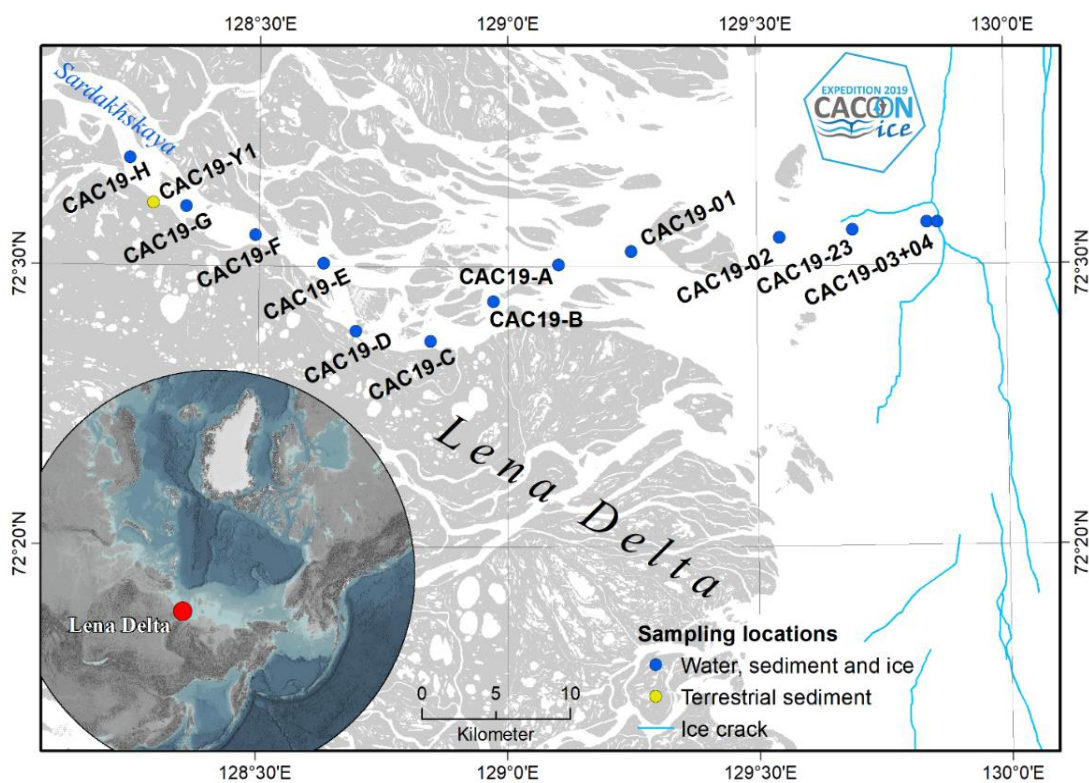


Figure 7: from: Sampling locations CACOON on ice report 2019. Sobo Sise Cliff marked yellow in the left part of transect and light blue lines indicate ice cracks, modified after M. Fuchs.

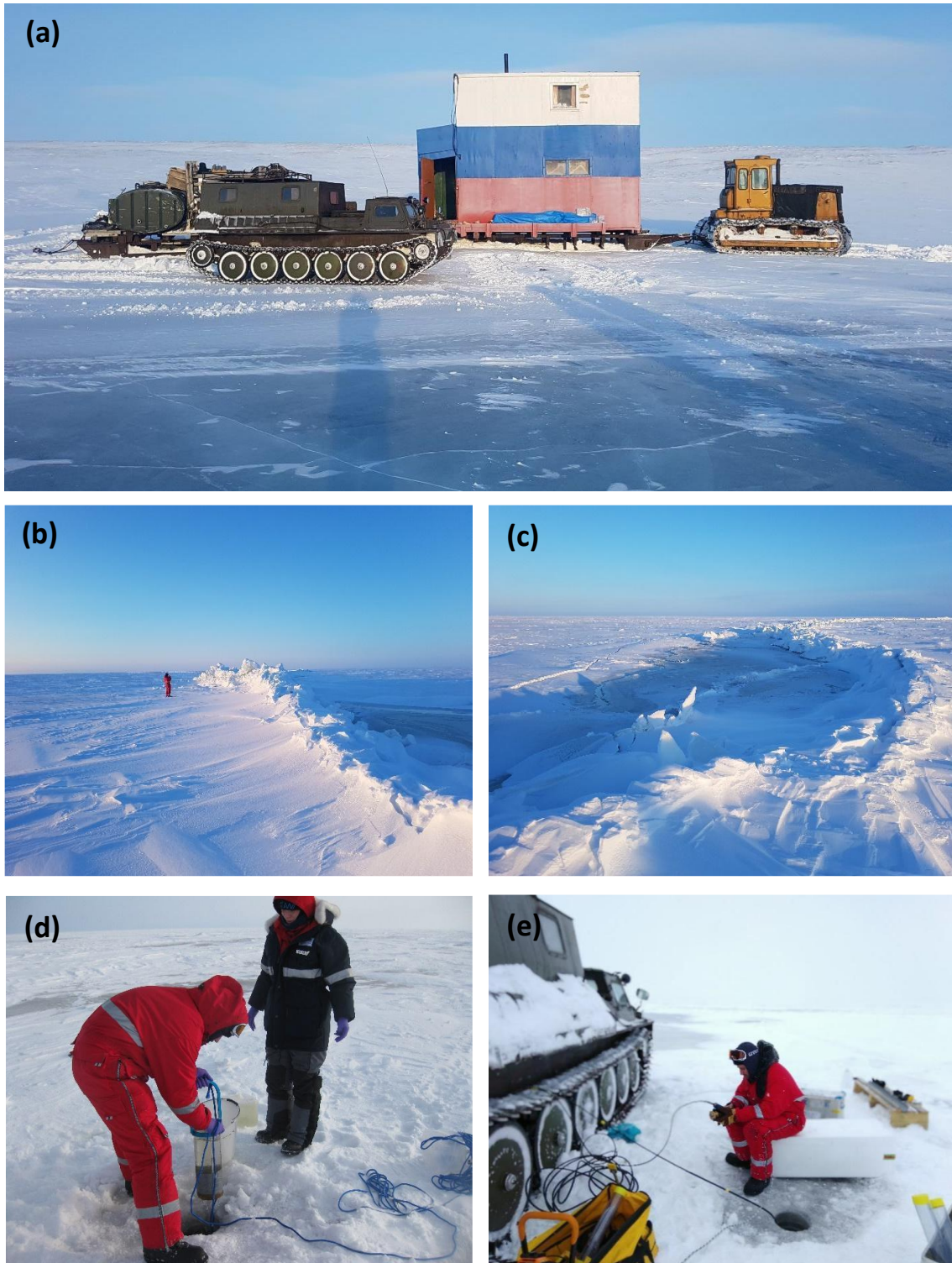


Figure 8: Impressions of the field and sampling procedures during the CACOON on Ice field campaign in March/April 2019: (a) Expedition vehicles for sampling, living and transportation on the ice (b) & (c) crack in the sea ice blocking the way with open water segment behind, (d) water sampling and (e) CTD measurements. Pictures from CACOON on ICE Expedition report (Strauss et al., 2019).

3.2 Biogeochemical parameters

Sedimentological parameters (TC, TN, TOC, $\delta^{13}\text{C}$) were investigated of all SOB18 samples taken in the field and analysed (Schirrmeyer & Wetterich, 2020) and made available for this thesis in order to facilitate biomarker subsampling and result interpretation. In the following section the measurement principles are presented in short.

TC and TN were quantified using the Elementar Vario EL III (Elementar Analysensysteme GmbH) (detection limit: 0.05% for carbon and 0.1% for nitrogen). About 8 mg of homogenized sample material were encapsulated in duplicate into small tin capsules on a Sartorius micro MP3 scale. Tungsten (VI)-oxide was added as a catalyser. The measurement is based on combustion chromatography, which implies the burning of samples at 950°C in an oxygen-saturated helium atmosphere. The elements of a sample (C and N) are oxidized into the gas phase and molecular N_2 . Carbon dioxide (CO_2), elemental nitrogen (N_2), nitrogen oxide (NO) and nitrogen dioxide (NO_2) are formed. TC and TN values are calculated in wt%, as a result of the context between the amount of gas and the initial weight of the sample. The TOC measurement was performed using the Elementar Vario Max C. This device follows a similar measurement principle as the TC and TN analyser, but at a combustion temperature of 580°C and a detection limit of 0.1 wt%. The samples were weighted into steel crucibles twice for each sample. The explicit mass was calculated, based on the TC values. Blank crucibles and control units were run in between the actual samples for calibration.

The stable carbon isotope ratio ($\delta^{13}\text{C}$) describes the ratio of the heavy stable ^{13}C and the light stable ^{12}C atoms. Samples were treated with hydrochloric acid, heated on a hotplate and washed with distilled water to remove carbonate from samples. The measurement of $\delta^{13}\text{C}$ was realized with a Flash 2000 Organic Elementar Analyzer by ThermoFisher Scientific, using helium as a carrier gas. The sample is combusted at 1020°C, transferring the OC to CO_2 . The isotope ratio is determined relative to a laboratory standard of known isotopic composition. Calibration and standard capsules were run in between the measurements. The $\delta^{13}\text{C}$ value was measured for samples with a TOC content above the detection limit only. The measuring unit is per mill (‰) and the ratio is compared to the $^{12}\text{C}/^{13}\text{C}$ standard ratio, defined by the Vienna Pee Dee Belemnite (VPDB).

3.3 Biomarkers

Biomarkers, also called geochemical fossils, are generally used as geochemical parameters in petroleum geology for source rock deposition, thermal maturity and biodegradation of oils (Peters et al., 2007) but are increasingly utilized in environmental science. Especially lipid biomarkers are well preserved in many geological archives and increasingly used to reconstruct past environmental and climate conditions (Schäfer et al., 2016). Lipid membranes are present in all living organisms and therefore they can provide information about e.g. the source of organic matter, environmental conditions during deposition, the diagenesis of sediments and the degree of biodegradation. In this study, the focus lies on *n*-alkanes of the aliphatic fraction as well as *n*-alcohols and *n*-fatty acids of the NSO fraction.

Hydrocarbons are divided into two broad classes: 1) aliphatic hydrocarbons, including alkanes and hopanes and 2) aromatic hydrocarbons. In addition, most definitely compounds such as sulfur, nitrogen and oxygen will be present when analysing biomarkers. They are called NSO-compounds which are subdivided into acidic and neutral fractions. The acidic fraction entails the fatty acids and the neutral fraction the alcohols. Typically changes in their relative abundances can be seen as a degree of biodegradation (Kim et al., 2005).

n-alkanes

N-alkanes are long chained aliphatic hydrocarbons with a single-bond. The absolute lipid concentration can be used to roughly determine organic matter preservation (Strauss et al., 2015). Meyers (2003) state, that because of their low susceptibility to microbial degradation relative to other types of organic matter, aliphatic hydrocarbons are generally robust recorders of the origins of organic matter. Specifically long chain n-alkanes (> C₂₅) are essential constituents of epicuticular leaf waxes and thus serve as specific biomarkers for higher terrestrial plants (Schäfer et al., 2016). In comparison to that, lower chain lengths indicate bacterial or algae origin (Figure 9).

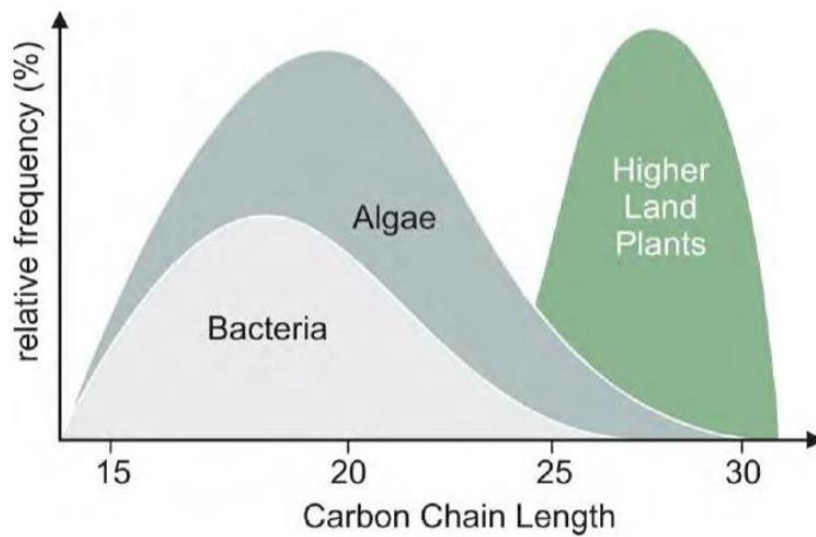


Figure 9: Relative frequency of n-alkane chain length in different organisms. Adapted from Jongejans et al. (2018), modified from Killops & Killops (2013).

Following that, the total absolute n-alkane concentration was calculated as the sum of all detectable chains of each sample, C₁₄ to C₃₅, and given in µg/gSed as well as µg/gTOC. The main chain was identified manually.

$$[n\text{-alkanes}] = \sum C_i$$

(C-concentration, i-carbon number)

Equation 3

The n-alkane Average Chain Length (ACL) is the weighted-average number of carbon atoms of higher land plants and is used for determining organic matter sources. When Poynter & Eglinton (1990) first described the index, they based it on the n-alkanes C₂₇, C₂₉ and C₃₁; chains, that are frequently used for identifying higher land plants. For calculations, the equation after Schäfer et al. (2016) was used (Equation 4), but with a chain interval C₂₃ to C₃₃ following Strauss et al. (2015) and Jongejans et al. (2018):

$$ACL = \frac{\sum i \times C_i}{\sum C_i}$$

Equation 4

The CPI (Carbon Preference Index) was originally introduced by Bray & Evans (1961) as the ratio of odd over even numbered alkanes which can be seen as a measure of the alteration of organic matter. (Equation 5) describes the CPI and was altered after Marzi et al. (1993) by using C₂₃₋₃₃ as chain interval.

$$CPI (C_{23} - 33) = \frac{(\sum_{i=n}^m C_{2i+1}) + (\sum_{i=n+1}^{m+1} C_{2i+1})}{2x (\sum_{i=n+1}^{m+1} C_{2i})}$$

Equation 5

With n representing the starting dominating chain length/2, m is the ending dominating chain length/2, i is the carbon number and C is the concentration. Generally, CPI values decrease as microbial degradation occurs (Glombitza et al., 2009). Therefore, degradation of OC would lead to an increasing trend upwards in the profile, as the lower located sediments had more time to degrade (principle of superposition).

NSO compounds

For the neutral fraction of NSO-compounds, the total sum has been calculated for present n -alcohols and n -sterols. The main chain has been identified manually. For the analysis of the acidic fraction of NSO-compounds, first the sum of present n -fatty acids was calculated in the same manner. The main chain has been identified manually.

$$[n\text{-alcohols}/n\text{-sterols}/n\text{-fatty acids}] = \sum C_i$$

Equation 6

As an indicator for chemical degradation of waxy components of organic matter, Poynter (1989) developed the Higher Plant Alkanole (HPA) index. It is used as a measure of the sum of selected n -alkanols/sum of selected n -alkanols and n -alkanes.

The higher plant fatty acids (HPFA) index was introduced by Strauss et al. (2015) and constructed (Equation 7) following the principles of Poynters' HPA index, with only using fatty acids instead of wax alkanols. The general assumption for the HPFA index is that it reflects the preservation degree of organic matter due to the higher lability of n -fatty acids in relation to n -alkanes (Strauss et al., 2015).

$$[HPFA] = \frac{\sum n\text{-fatty acids } C_{24}, C_{26}, C_{28}}{\sum n\text{-fatty acids } C_{24}, C_{26}, C_{28} + \sum n\text{-alkanes } C_{27}, C_{29}, C_{31}}$$

Equation 7

The HPFA ratio cannot be considered an absolute index of degradation but is an indicator of the relative amounts of the more labile fatty acids that remain in a sample (Strauss et al., 2015). n -alkanes are preferentially preserved over n -fatty acids, meaning a decrease in the HPFA index may indicate increased composition. The lower the HPFA index, the more degraded is the organic matter. Additionally, the ACL for n -fatty acids was calculated following the example from Equation 4.

Extraction and fraction separation

As introduced above 28 samples out of 61 were selected for detailed lipid biomarker analyses. Subsamples intended for biomarker analysis were separately put in preburned glass jars during field activities. Unfortunately, a shortage of glass jars led to storage of 9 samples (SOB18-06-09 to SOB18-06-

34) into plastic whirl packs. After freeze-drying and grinding the samples using a Fritsch pulverisette 5 planetary mill (8 min at 360 rotations per minute), all samples were retransferred into glass jars. The method was conducted following Strauss et al. (2015) and Schulte et al. (2000). For a step-by-step overview see Figure 10.

All 28 biomarker samples were processed in two batches of 14. First, 8-11g of grounded and dried sediment sample was weighed in extraction cell bodies for analysis with the ASE 200 Dionex, an accelerated solvent extractor. Dichlormethane/methanol (ratio 99:1) was used as a solvent for organic matter extraction from the samples. At first a static phase was induced for 20 min at 75°C and 5MPa (following 5 min of preheating). After that the dissolved compounds were further concentrated at ~42°C using a TurboVap (Zymark) closed-cell concentrator and the resulting solvent was then evaporated under a stream of nitrogen gas.

The amount of internal standards depended on the TOCwt% content, resulting in 80 µl for all standards with a concentration of 100 µg/ml. The following internal standards were added for respective fractions: 5α-androstane for aliphatics, ehylypyrene for aromatics, 5α-androstan-17-on for alcohols and steroids (NSO-) compounds and erucic acid for the NSO fatty-acid fraction.

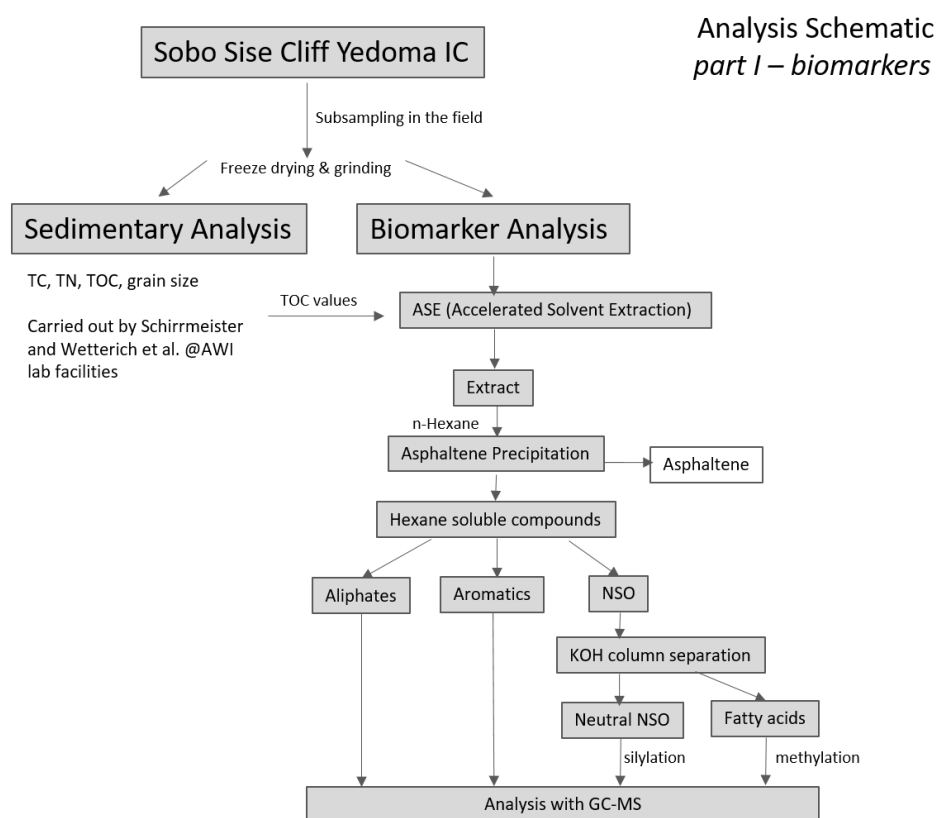


Figure 10: Schematic of Lipid Biomarker Analysis. After extraction and asphaltene precipitation biomarker samples were separated into three fractions: Aliphates, Aromatics and NSO-compounds. Further, the NSO-fraction was split into a neutral and an acidic fraction. All of the fraction were prepared and analysed with GC-MS.

An asphaltene precipitation was performed, to achieve the removal of all n-hexane-insoluble substances. Since the medium pressure liquid chromatography (MPLC; Radke et al., 1980) separation system uses n-hexane as a solvent: the samples were filtered through sodium sulphate combined with a large excess of n-hexane, after which the samples were concentrated again with the TurboVap 500.

The hexane-soluble portion was now separated by a medium-pressure liquid chromatography (MPLC) into three fractions, all having different polarities: aliphatic hydrocarbons, aromatic hydrocarbons and polar hetero compounds (NSO compounds). For this, the extracts were injected into the MPLC system and were led through a pre-column and main column with n-hexane. The pre-columns were filled with silica gel (thermally deactivated silica 100 63-200 μm and 200-500 μm on top with ratio $\sim 7:1$). Lastly, the NSO fraction was split up further into fatty acids and alcohol fraction by performing a KOH-column separation. The samples were led slowly through a KOH-impregnated silica gel column with dichlormethane.

Gas Chromatography-Mass Spectrometry (GC-MS) measurements

The aliphatic fractions were measured using combined gas chromatography and mass spectrometry (GC-MS; GC - Trace GC Ultra and MS - DSQ, both Thermo Fisher Scientific). After injection, the sample is vaporized immediately and mixed with the inert carrier gas helium. The GC uses a temperature vaporization, for which one sample is placed in a cool chamber of 50°C and is heated up to 300°C (heating rate: 10°C per second, isothermal holding time of 10 minutes). The mixture is then led through a capillary column (50 m long, \varnothing 22 μm , film thickness 0.25 μm) (Peters et al., 2007). The oven temperature was programmed from 50°C to 310°C (heating rate: 3°C per minute, isothermal holding time of 30 minutes). To be able to identify compounds, the gas chromatograph is linked to the mass spectrometer (ionization mode at 70 eV, at 230°C). Full scan mass spectra were obtained from m/z 50 to 600 Da (2.5 scans per second). By using the software XCalibur, the peaks in the GC-MS were integrated using the standard 5 α -androstane with a known concentration as a reference. Peak areas of target compounds of n-alkanes and hopanes could be identified. The GC coupled with the MS is producing a fingerprint chromatogram of the respective sample by depicting the compounds in a molecule-mass order over retentions time.

The GDGTs analyses are performed on a Shimadzu LC-10AD high-performance liquid chromatography (HPLC) device coupled to a Finnigan TS 7000 mass spectrometer with an APCI (Atmospheric Pressure Chemical Ionization) interface. The samples were separated in a Prevail Cyano column (2.1x150 mm, 3 μm ; Alltech) with a precolumn filter at 30°C. The mobile phase started with 5 minutes of n-hexane (99:1 v/v), a linear gradient to 1.8% isopropanol within 40 minutes, in 1 minute to 10% isopropanol (held for 5 minutes for cleaning) and finally back to initial conditions in 1 minute (held for 16 minutes for calibration). The device flow rate was set to 200 $\mu\text{l min}^{-1}$. The APCI device has a corona current of 5 μA , voltage of 5 kV, the vaporizer temperature is 350°C and the capillary temperature 200°C. The source operates with nitrogen sheath gas at 60 psi and without auxiliary gas. Full mass spectra were obtained at a scan rate of 0.33 s. Again, XCalibur is used for integration of compound peak areas.

3.4 Dissolved Organic Carbon

The CAC19 water samples for DOC analysis were filtered (0.7 μm) and acidified with 20 μl concentrated (35%) hydrochloric acid (HCl) and were kept cool in a lab refrigerator at 4°C. The DOC was measured as non – purgeable organic carbon (NPOC), which refers to organic carbon that is present in a sample in a non-volatile form.

The DOC measurement was conducted with a Total Organic Analyser TOC-VCPH/CPN from SHIMADZU at AWI Potsdam. 2 ml of water were diluted with 10 ml of distilled water and filled into small test tubes. The tubes were placed into the auto-sampler of the analyser. During the measurement, sparge gas was first bubbled through the sample and hydrochloric acid was added to remove inorganic carbon by converting it to carbon dioxide. The remaining organic carbon is measured by burning the sample at

680°C and measuring the CO₂ concentration. To ensure the accuracy of the measurement, blank samples of ultra-pure water and standards with a known DOC concentrations were run before and after each measurement.

3.5 Denitrifier Method

During various stages in the nitrogen cycle, biological processes favour the light nitrogen isotope (¹⁴N) over the heavy isotope (¹⁵N) because it is more energetically favourable (Sigman et al., 2001). The residual pool is left with heavier isotopes, hence a higher isotopic signature. Transformation between nitrogen pools show specific kinetic isotopic fractionation with fractionation factors unique to each transformation process. The use of the dual isotope technique can distinguish sources of nitrate and determine the relative influence of nitrogen cycling processes (Sigman et al., 2001; Granger et al., 2004; Tuerena, 2015; Casciotti, 2016) such as nitrification, assimilation or denitrification (Thibodeau et al., 2017). Similar to Nitrate, I determine δ¹⁵N of DON to identify possible sources and combine in with isotopic nitrate data to find out about cycling mechanisms.

In this section, the denitrifier method is described, adapted and altered from Sigman et al. (2001), Casciotti (2016) and McIlvin & Casciotti (2011). This method utilises the denitrifying bacteria *Pseudomonas aureofaciens* that lack nitrous oxide (N₂O) reductase activity to convert dissolved inorganic nitrate into N₂O for subsequent analysis by Isotope Ratio Mass Spectrometry (IRMS) (Casciotti et al., 2002; Sigman et al., 2001), by meanwhile maintaining the identical isotopic signature to the original nitrate.

Although the reaction is quantitative for N atoms, O isotopes undergo distinct branching fractionations (Casciotti et al., 2002) between the transition from NO₃⁻ to N₂O because ¹⁶O is preferentially removed, leaving ¹⁸O enriched in the N₂O product, according to Casciotti (2016). These consistent fractionation factors can be corrected by parallel analysis of NO₃ isotope standards after Weigand et al. (2016).

In the following two paragraphs, the method is described for δ¹⁵N of nitrate and δ¹⁵N of TDN, the latter using a triple crystallization of potassium persulphate to oxidize present organic nitrogen in the sample to nitrate for subsequent analysis. The whole analysis scheme is displayed in Figure 11.

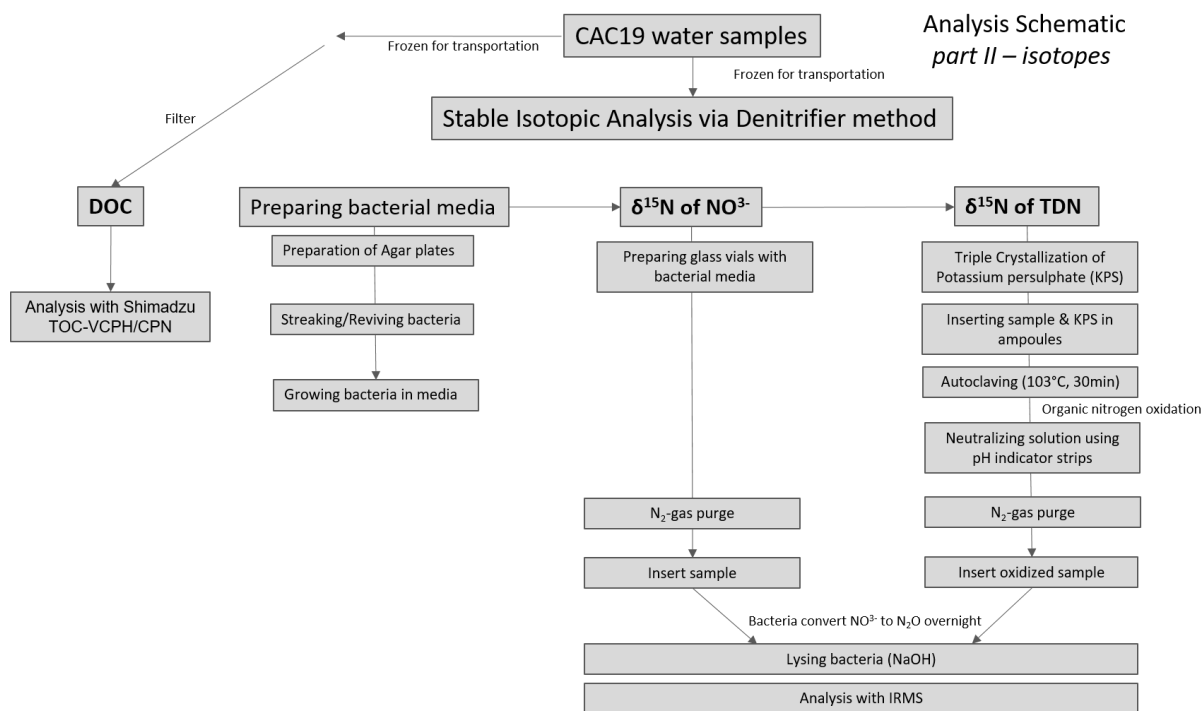


Figure 11: Schematic of water sample analysis. Samples were separately frozen and stored in the field and separately analysed for DOC and nitrogen compounds via denitrifier analysis.

3.5.1 Analysis of $\delta^{15}\text{N}$ of Nitrate (NO_3^-)

Preparation of Agar Plates

For creating Agar culturing plates 500 mL milliQ water, 0,5 g KNO_3 , 0,125 g $(\text{NH}_4)_2\text{SO}_4$, 2,5 g KH_2PO_4 , 15 g Tryptic Soy Broth and 15 g Tryptic Soy Agar are combined in a 2 l conical flask and left on a magnetic stirrer plate (no heating) until all solids have dissolved and liquid is clear. The flask is autoclaved (105 °C for 30 min), cooled down slightly until liquid has thickened enough to allow easy and uniform spreading of agar, but also limiting possible condensation which could encourage bacterial growth. Plates are then stacked to ensure slower cooling and again built up of condensation and stored in a cool, dark place with a desiccant to avoid contamination.

Streaking Plates

For reviving bacteria from frozen stock (-80 °C), working area was cleaned with 70 % ethanol before use. The inoculating loop was sterilised using a blow-torch flame before and after every individual use. The sterilised loop is used to pick up frozen bacteria (Figure 12 a) and touch onto first agar plate at an inoculation point (heat from loop melts ice). The loop was streaked across agar plate (two zig-zag movements, perpendicular to each other) to spread bacteria and ensure their growth in individual colonies. That was repeated for up to 3 more plates, each time using a bacteria culture from a different pot and flame sterilising the inoculating loop. Bacteria are returned to the freezer as soon as possible to ensure minimum exposure to atmosphere. The plates are again stored in a sealed plastic container with desiccant in a dark place at room temperature for 2-4 days to allow bacteria to grow. After distinct individually visible colonies have developed, the sterilised loop was used to pick up one colony and transfer it to another agar plate, again streaking following the above mentioned zig-zag pattern. This procedure was repeated for all plates with sufficiently well-developed colonies and also repeated again after 3-4 days once bacteria had grown in the new plates (Figure 12 b).

Media preparation

2 l milliQ water, 2 g KNO₃, 0.5 g (NH₄)₂ SO₄, 10 g KH₂PO₄, and 60 g Tryptic Soy Broth were mixed together using a magnetic stirrer in a 2l conical flask for preparation of bacterial media. The mix was transferred to clean crimp seal bottles and butyl stoppers are placed lightly on top for autoclaving at 120 °C for 30 min on the media dynamic cycle. After one cycle, they were crimp sealed immediately and stored in a dark place. For the preparation of *nitrate free media* the recipe is altered combining 1L milliQ water, 0.25g (NH₄)₂ SO₄, 5g KH₂PO₄, and 30 g Tryptic Soy Broth, without adding KNO₃. Once mixed, 150 ml are decanted into 250 ml Duran bottles. After a cycle in the autoclave at (105°C for 30 min) bottles are sealed and stored in the dark.

Growing bacteria

When bacterial colonies had grown sufficiently on the agar plates (colony from plate 2, 3 or 4) the sterilised inoculating loop is used to take up a singled out colony and to put it into a starter tube with bacterial media (Figure 12 c). The media containing bacteria was now left overnight at room temperature on the oscillation table to allow bacteria to grow (liquid appears cloudy from bacteria). The following day, 0.7-1 ml of the bacterial liquid in the starter tube was injected into upturned media bottle and placed again on oscillating table and left for 6-10 days until they turn cloudy.

Sample vial preparation

For one batch (40vials), three media bottles have been used. To test bacterial media of presence of nitrite, ~1ml from each used bacterial media bottle was extracted with a sterile needle and place into a vial. 120µl of Sulphanilamide + HCl and NED reagents were pipetted into the 1ml of media. If nitrite present, liquid turns pink, which means the media has been left on the oscillating table for longer; if media did not change its colour, it was used for sample preparation. The media from the 3 bottles were equally distributed into 8 different 60ml centrifuge tubes and centrifuged at 5000 rpm for 10-14 min. Decanting the remains back into the three media tubes is leaving the pinkish-brownish bacteria in tube bottoms. 20ml of nitrate free media from the Duran bottle were then transferred into centrifuge vials with bacteria, adding also 0.1ml of antifoam, to incorporate bacteria into solution. All the liquid from the 8 tubes are now combined in one media bottle. 3 ml of this mixture of bacterial liquid and nitrate free media were pipetted into each of the desired sample vials and crimp sealed. The vials are then put on a nitrogen gas bubbling rag by placing a venting needle in one side of the butyl stopper on each vial for purging with nitrogen gas (3 h). Vials are removed and injected with sample volume or standards respectively. Is the volume exceeding 1 ml, a venting needle is inserted to prevent over pressuring.

Since there had been no previous analysis done on the samples concerning nutrients plus the amount of time spent on the method wanted to be kept to a minimum, I injected a fixed 10ml volume of each sample for the first run. After that, I calculated the amount of nitrate the samples must contain and for a second run, injected duplicates of each sample with a specific sample volume (see Appendix for further details). Three samples were hereby excluded from the analysis because the amount of nitrate was at a minimum. Normally with this method the volume of sample water added to each vial is calculated by dividing the concentration of nitrate required (in nmol) by the nitrate in the water sample (µmol/L). USGS 32, USGS 34 and USGS 35 are used as certified reference materials for mass spectrometric analyses of N₂O gas. They are stored at -20°C and are each of 200 µmol/L made up from stock solution. Vials were then upturned and left overnight in a dark place at room temperature. Bacteria were lysed the morning after by injecting approximately 0.1 ml of 10 N NaOH to kill bacteria.

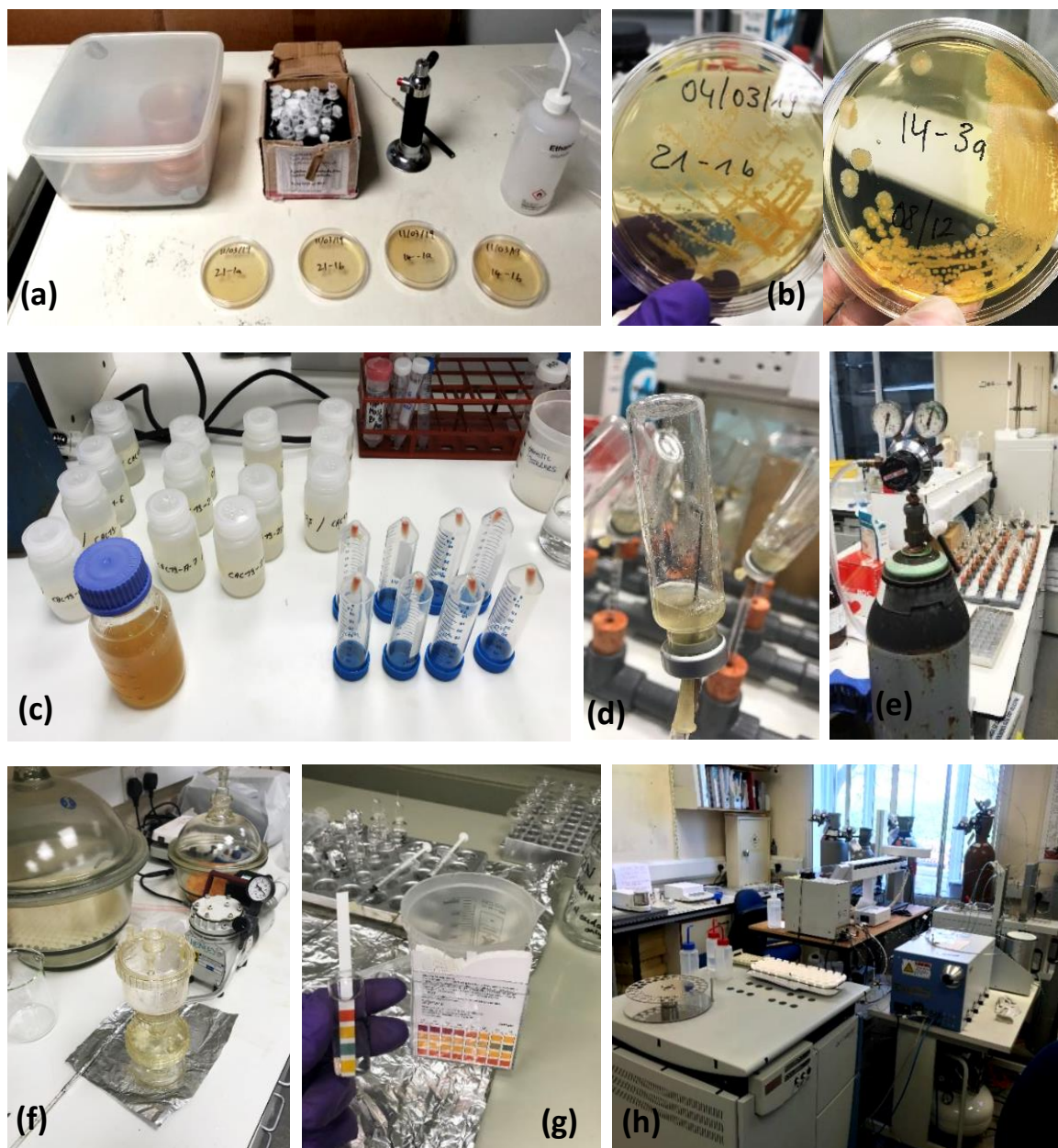


Figure 12: Steps of Denitrifier Method leading to Stable Isotope Analysis: **(a)** Set-up for reviving the bacteria from frozen stock, **(b)** Growing bacteria on agar plates, **(c)** Sample defrosting (left) and pinkish-white bacterial deposit in tubes after centrifuging (right), **(d)** Single vial on purging system, **(e)** N_2 -purge system set-up in the laboratory, **(f)** Triple Crystallization of Potassium persulphate, **(g)** Neutralizing after organic nitrogen oxidation for TDN, **(h)** Samples are lysed and analysed in the IRMS (Isotope Ratio Mass Spectrometry) after a period of ~24h.

Isotope Ratio Mass Spectrometry (IRMS)

The gas in the headspace of the sample vials is analysed using a Combi PAL auto sampler linked through a Thermo Fisher Scientific GasBench II to a Thermo Fisher Scientific Delta V Advantage (Figure 12 h) stable isotope mass spectrometer with a detection limit $> 0.5\text{ppm}$. Output values from the IRMS have been checked for faulty values. Only values with a peak start time of around 1340s were considered because they match the nitrate peak on the IRMS. Eliminated were also samples with a peak area intensity value > 2 from the standards of the run. Values were also corrected after the method described in Sigman et al. (2001) and Weigand et al. (2016). This involves creating a regression line between observed and measures standard values to obtain corrected isotopic values. Fairly low concentration

runs of 15 nmols are corrected by altering the expected concentration value of nitrate from each sample in the spreadsheet. The internal standard IAEA-N3 is used for analytical precision of $\delta^{15}\text{N-NO}_3$ and USGS-34 for $\delta^{18}\text{O-NO}_3$ respectively.

3.5.2 Analysis of $\delta^{15}\text{N}$ of TDN

Triple Crystallization of Potassium persulphate

300ml of milliQ water was heated up to 60°C. 100 g of potassium persulphate (KPS) is mixed into water with a magnetic stirrer. After that, the mixture is cooled down until crystals form (around 10°C, ~1h) in a tub of water that has been previously put in the freezer to cool down. Now, the solution was filtered by using a vacuum pump, leaving the crystallised KPS behind. Repeating the process 3 times ensures that the solution is eliminated of any trace amounts of nitrogen. Each recrystallization round should start with a lower KPS-water ratio and heated gradually until the crystals have just dissolved, which minimises the loss of the KPS with each recrystallization.

Organic nitrogen oxidation

75ml milliQ water, 25ml 2N NaOH and 1g of the triple recrystallized KPS were used to prepare an alkaline potassium persulphate solution. An amount of 1ml was pipetted into ampoules for standards and 0.66ml are used for samples. Standards used in this method were USGS-32 and USGS-34 at 5, 10 and 20 μM concentrations respectively. Ampoules containing standards with KPS solutions were flame sealed using a blowtorch, while ampoules for internal standards U40 and Glycine were injected with 1.5ml of each standard (equivalent to 60 nmols of N) before flame sealing. For the samples, after sample volume was injected using 5ml volume each and immediately flame sealed after that. All ampoules were then autoclaved (105°C for 30 min) before being relabelled.

Afterwards, all TDN in the sample were oxidised into an equivalent amount of nitrate. Ampoules were then opened and neutralized: milliQ-water was added to respective ampoules along with drops of 4N HCl and/or 2N NaOH until the solution was at approximately pH 7 (tested with indicator strips). Samples were now injected into sample vials following the preparation and purging as part of the denitrifier method described in the paragraph above. Internal standards and blanks were split evenly between three sample vials while sample ampoules were split between two. Standards U34 and U32 were injected at volumes corresponding to the required concentrations. Vials were left overnight before lysing with NaOH and analysis with IRMS (see above). The steps for identification for isotopic signal for TDN are shown in Figure 12 f) and g).

3.6 Calculating $d^{15}\text{N}$ of DON

$\delta^{15}\text{N}$ for nitrogen species is calculated using Equation 8. The standard is atmospheric N_2 gas. The oxygen isotopic ratio (between ^{16}O and ^{18}O) is calculated in the same way but with V-SMOW (Vienna Standard Mean Ocean Water) as standard.

$$\delta^{15}\text{N}(\text{‰}) = \left(\frac{(^{15}\text{N}/^{14}\text{N})_{\text{sample}}}{(^{15}\text{N}/^{14}\text{N})_{\text{standard}}} - 1 \right) * 1000$$

Equation 8

The isotopic value of $\delta^{15}\text{N-DON}$ can be calculated using values from $\delta^{15}\text{N-NO}_3^-$ and $\delta^{15}\text{N-TDN}$, because $\delta^{15}\text{N-TDN}$ values represent both isotopic signatures of DON and DIN. Again, the assumption is that

ammonium is negligible and DIN can be seen as NO_3^- : ammonium is unstable in peatland environments and is rapidly converted into nitrate, meaning nitrate makes up the majority of the DIN pool and ammonium is often below detection limits (Holmes et al., 2012).

In order to compare processes of organic and inorganic nitrogen, $\delta^{15}\text{N}$ of DON can be calculated following **Equation 1** that has been adapted from Francis (2019). This equation was only used when values for $\delta^{15}\text{N}$ of nitrate were measured (when samples had $[\text{NO}_3^-] > 1\mu\text{M}$).

$$\delta^{15}\text{N-DON} = (\delta^{15}\text{N-TDN} * \text{weight of [TDN]}) - (\delta^{15}\text{N-NO}_3^- * \text{weight of [NO}_3^-])$$

Equation 9

3.7 Geochronology

Radiocarbon dating is based on the differences between the $^{14}\text{C}/^{12}\text{C}$ ratio in the atmosphere and the organic matter, where the atmospheric ratio is assumed to be constant. When an organism dies, the unstable ^{14}C decays to ^{14}N following a constant rate. The half-time is 5370 ± 40 year, meaning the time it takes for half of the organism to decay. It is possible to calculate the time of death that has passed since death of the organism via the comparison of the decreased $^{14}\text{C}/^{12}\text{C}$ ratio to the original ratio. Changes in production rate (changes in the cosmic-ray flux) as well as changes in the carbon cycle leads to radiocarbon concentration variation in the atmosphere over time. Therefore, radiocarbon dating is limited to samples older than 50 ka BP and a calibration of the obtained ages is required (Reimer et al., 2013). Age determination has been done for selected terrestrial samples of the SOB18-01, SOB18-03 and SOB18-06 sections. Dating took place at AWI Bremerhaven using a Mini Carbon Dating System (MICADAS). The radiocarbon ages were then calibrated using the CALIB 7.1 software and the IntCal13 calibration curve (Stuiver et al., 2017) and expressed as calibrated kilo years before present (cal ka BP). Additionally, an age-depth model was applied to the all samples, using the Bacon package of R environment version 3.3.1. Bacon is an approach to age-depth modelling that uses Bayesian statistics in order to reconstruct Bayesian accumulation histories for deposits, through combining radiocarbon and other dates with prior information (Blaauw & Christen, 2011).

3.8 Data Analysis and Statistics

The software ODV (Ocean Data View) has been used to plot and visualise oceanographic data in section or scatter plots. Given the relatively low amount of sample points, original data points were up-scaled using the DIVA gridding software built-in to achieve neat visualization.

Dependencies were tested using a two sample t-test with unequal variances. This was done using the data-analysis tool for t-tests in excel. Additionally, to test linear dependencies, linear regression were performed. The goal of linear regression analysis is to describe the relationship between two variables based on observed data and to predict the value of the dependent variable based on the value of the independent variable. Therefore a prediction of y from x of the form

$$y = \alpha x + \beta$$

Equation 10

where $\alpha + \beta x$ is the deterministic portion of the model is used to describe the regression analysis. Outputs from regression analysis tool in Excel are further R^2 , the coefficient of determination, the sample number (n) and p-value.

3.8.1 Hierarchical Clustering with R

The data is clustered with the function `chclust` of the `rioja` package in R studio which is able to perform a constrained hierarchical clustering of a distance matrix, with clusters constrained by sample order (Juggins, 2019). Each single observation is assigned its own cluster (see Figure 13). Then the distance between two individual clusters is computed after which the most similar ones are merged into one. This procedure is repeated until there is only one cluster left. The advantage for environmental studies is, that the order is maintained (e.g. over a sediment core). This means, for the terrestrial samples, the three cores SOB18-01, SOB18-03 and SOB18-06 and all aquatic samples over the seaward transect were statistically grouped by maintaining spatial arrangement. This method enables investigation of OM processing in the study area. The code can be viewed in the appendix (8.1).

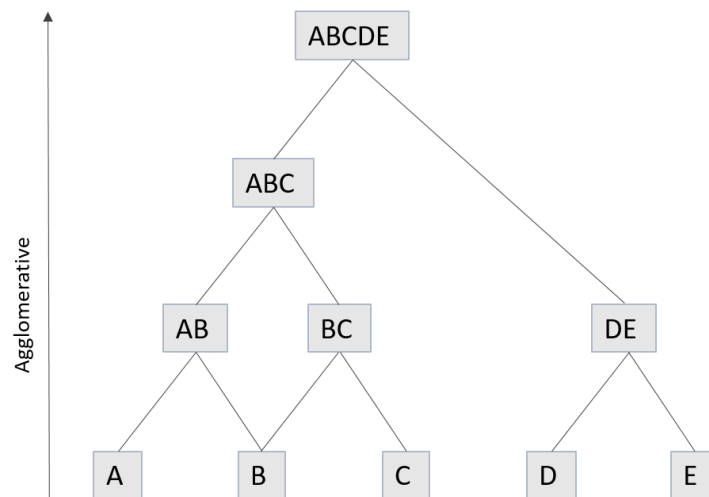


Figure 13: Schematic of hierarchical clustering performed with `chclust` function of `rioja` package in R studio. Agglomerative clusters are constrained by sample order.

3.8.2 Spearman's rank correlation

Spearman's rank correlation is a non-parametric test that is used for calculating the linear relation of two non-specifically distributed data sets. The two dataset to be compared will be ranked internally first. Then the correlation coefficient ρ is calculated in Equation 11:

$$\rho = 1 - \frac{6 * \sum_{i=1}^n (r_i - s_i)^2}{n^3 - n}$$

Equation 11

r_i is the rank within dataset x of the i-variable, s_i represents the rank with in dataset y of the i-variable and n is the amount of data points. Ranking the data means, that the calculation is not done with the actual values but rather with the rank equivalent and therefore the test is based on the order of the data. The rank coefficient rho (ρ) can take on a value between -1 and 1. If the $\rho < 0$, there is a negative correlation, if $\rho > 0$ there is a positive correlation and if $\rho = 0$ there is no correlation.

3.8.3 Kruskal-Wallis-Test

This nonparametric test was designed for comparing multiple populations. In this thesis it is used to test the significant differences for the biogeochemistry of the permafrost sections. After clustering, the Kruskal-Wallis test is applied to the identified groups.

The test statistic H is calculated with Equation 12. All values, independent of group, are ranked. The ranks are added per group, squared and divided by total sample size.

$$H = \frac{12}{n(n+1)} \sum_{j=1}^k \frac{R_j^2}{n_j} - 3(n+1)$$

Equation 12

In this equation k is the number of groups, n_j the size of the j th group, R_j the rank sum for the j th group and n is the total sample size. The null hypothesis H_0 states that there is no differences, alternative hypothesis H_1 is that there occur differences. The p -value is calculated using the right-tailed probability of the chi-squared distribution, using 2 degrees of freedom (Zaiontz, 2013).

4 Results

4.1 Sedimentological parameters

In the following section, the results of the laboratory analyses of lipid biomarkers of the three sections SOB18-01, SOB18-03 and SOB18-06 are shown. Those sections are schematically displayed in Figure 14 as a cross section of sample locations. The cliff top is at 25 marl (25m height = 0 m depth). **Figure 14** displays 8 biomarker samples taken in the field at SOB18-03, but only 5 samples were selected for analysis from that core, because they are most relevant for overlap with adjacent cores.

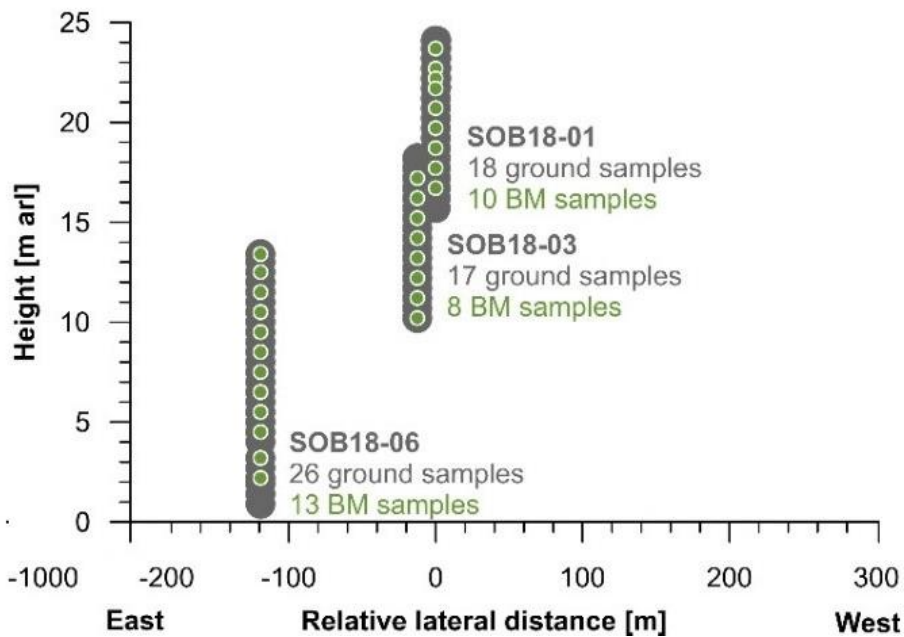


Figure 14: Sobo-Sise cross section SE to NW by Schirrmeyer & Wetterich (2020) and relative locations of sampling sites and locations for SOB18-01, SOB18-03 and SOB18-06. The cores show a distinct overlap. Schematic modified after Expedition Report - (Wetterich et al., 2018).

27 out of 28 samples were within TOC detection limit (exceeding 0.1 wt% TOC). All the sedimentary parameters are displayed in Figure 15. The sample SOB18-01-18 (at 15.7 marl) was under the detection limit (below 0.1 wt%) and therefore excluded from further analysis. TOC ranged from 0.82 wt% to 25.51 wt%, both values within section SOB18-01 and the upper 5.5 m. TOC had an average of 5.13 wt% and shows generally little variation. From the cliff top downwards, TOC values decreased with elevated values at 16.2 marl (SOB18-03-05; 11.31 wt%), 9.5 marl (SOB18-06-09; 6.95 wt%) and 3.2 marl (SOB18-06-30; 5.64 wt%). TN values average 0.35 wt% and the highest value is at 24.1 marl (SOB18-01-01; 0.83 wt%) and the lowest at 18.7 marl (SOB18-01-12; 0.11 wt%). If TOC and TN value was >0.1 wt%, C/N ratio was calculated. C/N ranged from 7.2 to 30.55 (again, both in SOB18-01, same data points as mentioned

above). All C/N values correlated with the TOC values, and appeared relatively steady over the whole profile with a mean of 13.24. The $\delta^{13}\text{C}$ ranges from -25.22 (SOB18-01-12; 18.7 marl) to -29.43 ‰ (SOB18-03-05; 16.2 marl). Highest and lowest $\delta^{13}\text{C}$ match lowest highest TOC values. The lower $\delta^{13}\text{C}$ values roughly match elevated C/N values and vice versa over the profile. An overview of sedimentological parameters is shown in Figure 15.

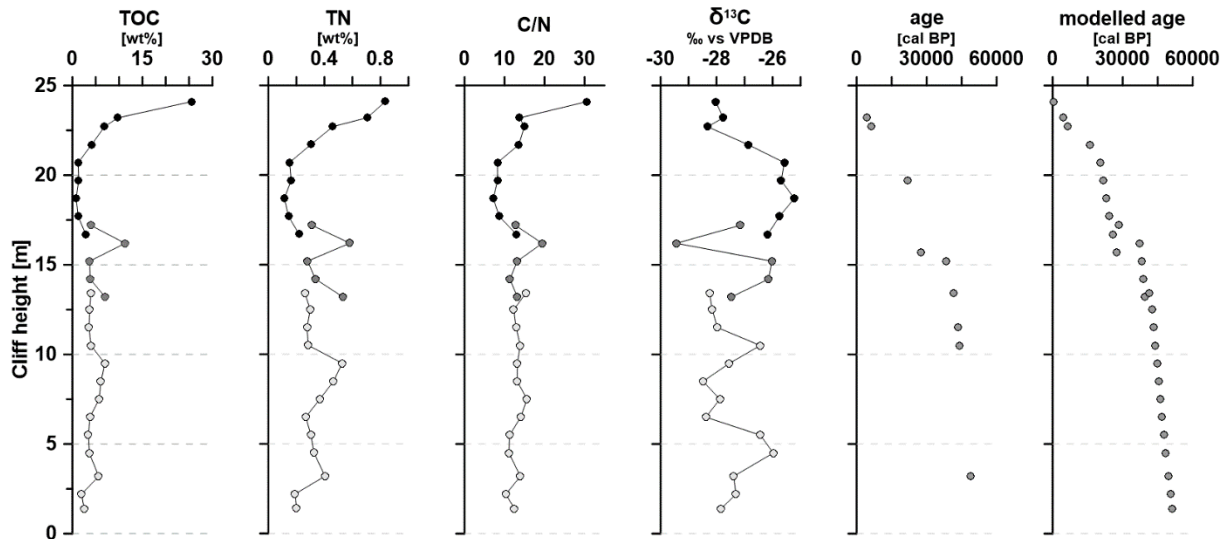


Figure 15: Overview of SOB18-01, SOB18-03 & SOB18-06 samples and their sedimentological parameters: total organic carbon (TOC), total nitrogen (TN), carbon over nitrogen ratio (C/N) and $\delta^{13}\text{C}$. Data points are displayed over cliff depth from cliff top (25m) to cliff bottom (0m) at river level, median ages originally measured and modelled median ages both in cal BP. The three sections of SOB18 are plotted separately for each parameter: SOB18-01 black circle, SOB18-03 dark grey circle and SOB18-06 light grey circle. Graph created with Grapher 9.

Originally, ages were analysed on selected samples (9). Depicted in Figure 15 are median ages of the 9 analysed samples and next to it the modelled ages for the remaining samples. Median ages were youngest 4 443 cal BP (SOB18-01-03; 23.2 m arl) and showed oldest 48 899 cal BP ages (SOB18-06-30; 3.2 m arl). Average values compared to 30 726.22 cal BP (measured) to 34 093.21 cal BP (calculated). There was an age-depth trend visible in measured samples which translate to the extrapolated ages.

4.2 Biomarker parameters

n-alkanes

n-alkanes occurred in all 28 analysed biomarker samples. Figure 16 displays the biomarker parameters relating to *n*-alkanes. Absolute *n*-alkane concentration ranges from 1.46 $\mu\text{g/gSed}$ (SOB18-01-08; 15.7 m arl) to 107.55 $\mu\text{g/gSed}$ (SOB18-06-05; 11.5 m arl). The overall mean was 42.50 $\mu\text{g/gSed}$ and the absolute *n*-alkane concentration increased in the lower part of the cliff, closer to the river level. The dominating chain length for each sample was computed and is unevenly distributed to odd carbon number chains: C_{27} , C_{29} and C_{31} . All main chains had odd carbon numbers and the most abundant is C_{27} . Generally the *n*-alkanes exhibited a strong odd over even preference.

The ACL of *n*-alkanes showed a relatively stable value over all samples with the mean 25.38. Maximum value was at 27.29 (SOB18-01-04; 22.7 m arl) and minimum value at 23.14 (SOB18-06-34; 1.4 m arl). The ACL trend was fairly steady between the cliff top and about 8 m arl where it decreased but spikes up again at 4.5 m arl and then decreased again. The CPI of *n*-alkanes is at a minimum value of 5.76 (SOB18-06-15; 6.5 m arl) and extent to 16.29 (SOB18-06-05; 11.5 m arl) with a mean value of 9.89. The CPI trend was fairly consistent and decreased slightly in the lower part of the cliff.

Figure 17 shows an overview of a typical chromatogram derived from GC-MS analysis showing an *n*-alkane distribution of SOB-03-11. Odd-numbered *n*-alkane compounds appeared at a higher concentration than even-numbered *n*-alkanes. This can be observed throughout all samples.

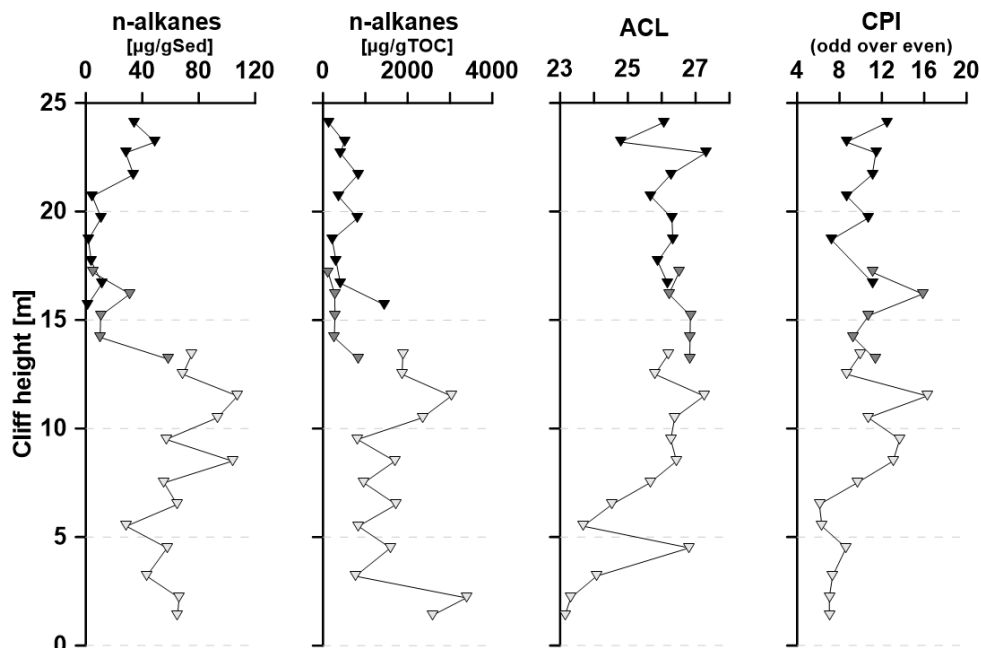


Figure 16: *n*-alkane concentration displayed as $\mu\text{g/gSed}$ and $\mu\text{g/gTOC}$; Average Chain Length (ACL) and Carbon Preference Index (CPI). Data points are displayed over cliff height from cliff top (25m) to cliff bottom (0m) at river level. The three sections of SOB18 are plotted separately for each parameter: SOB18-01 black triangle, SOB18-03 dark grey triangle and SOB18-06 light grey triangle. Graphs have been created with Grapher 9.

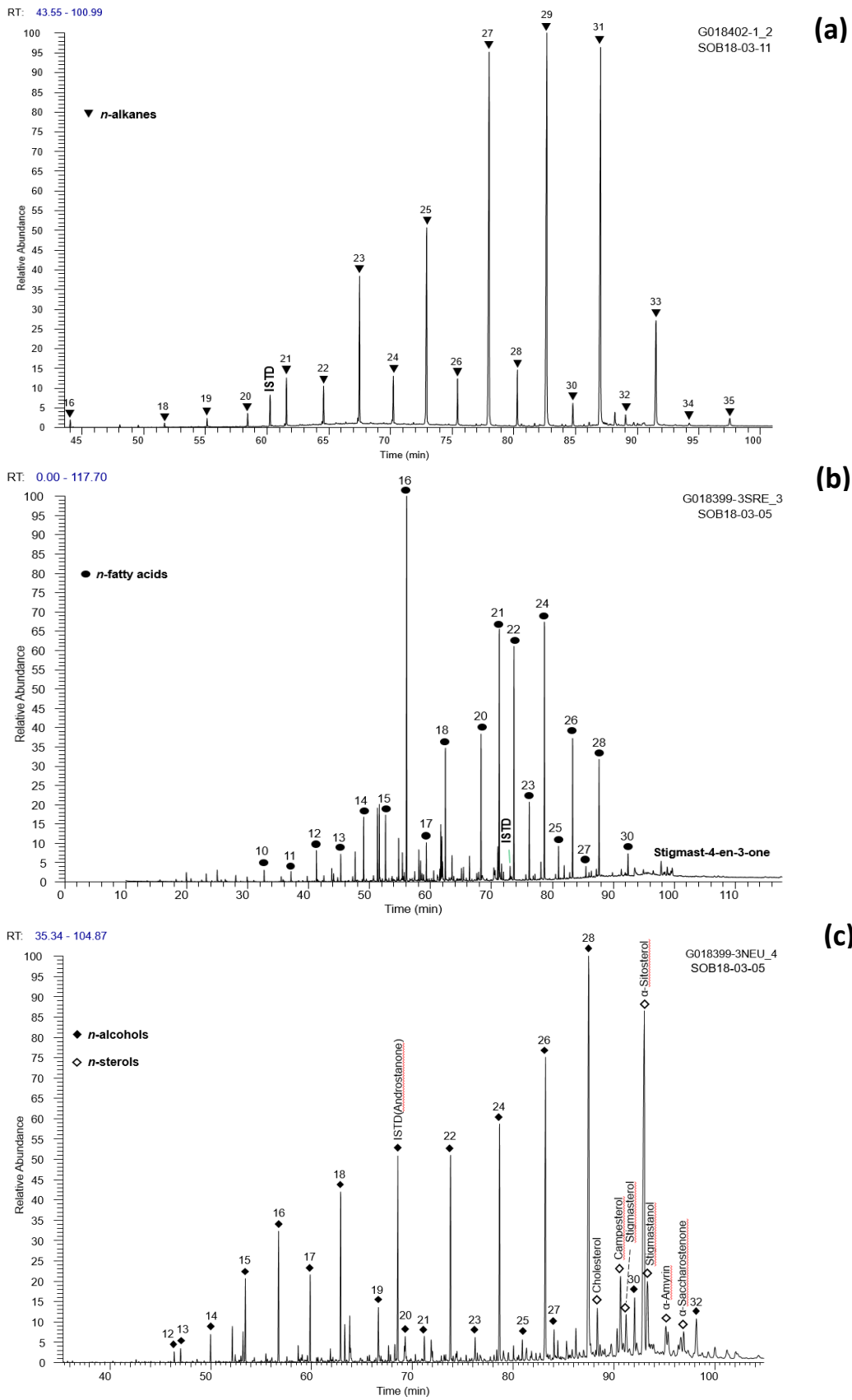


Figure 17: GC-MS chromatograms of analysed biomarker compounds: (a) n-alkanes (b) n-fatty acids and (c) n-alcohols/n-sterols. ISTD = internal standard (alkanes: androstane; fatty acids: erucic acid; alcohol fraction: 5 α -androstan-17-one). Numbers indicate carbon numbers of n-alkanes, n-fatty acids, n-alcohols and n-sterols respectively. Chromatograms extracted from xCalibur.

NSO compounds

Fatty acids, alcohols and sterols occurred in all sub-analysed 13 biomarker samples of the NSO fraction. Figure 17 shows an overview of a typical chromatogram of *n*-fatty acid- and alcohol-/sterol- distributions derived from GC-MS analysis. Values for absolute *n*-fatty acids ranged from 34.27 $\mu\text{g/gSed}$ (SOB18-06-13; 7.5 m arl) to 290.39 $\mu\text{g/gSed}$ (SOB18-01-04; 22.7 m arl) with a mean value of 126.42 $\mu\text{g/gSed}$. Moreover, the *n*-fatty acids were detected with a higher distribution favouring even-numbered carbon chains. C_{24} was detected the most abundant *n*-fatty acid compound, with the lowest being C_{16} and the highest C_{26} . The $\text{ACL}_{n\text{-fatty acid}}$ was not showing a lot of variation ranging from 24.57 to 25.28 and the mean value of 25.01 compared well to the $\text{ACL}_{n\text{-alkane}}$ (mean: 25.83). HPFA index was following the trend of the *n*-fatty acids concentrations as well as minimum 0.25 (SOB18-06-13; 7.5 m arl) and maximum 0.86 (SOB18-01-04; 22.7 m arl) values in the same samples (see Figure 18). The HPFA mean was relatively consistent with a value of 0.60. %

In the neutral part of the NSO fraction, both alcohols and sterols were detected. Mean *n*-alcohol concentration was at 97.66 $\mu\text{g/gSed}$ with spanning from minimum 29.76 $\mu\text{g/gSed}$ (SOB18-06-17; 5.5 marl) to maximum 534.19 $\mu\text{g/gSed}$ (SOB18-01-03; 23.2 m arl). The most abundant chain was $\text{C}_{28}\text{-OH}$ where almost all alcohols are exhibiting this chain. Only in the upper few samples down from the cliff top $\text{C}_{26}\text{-OH}$ was prevalent. Generally, *n*-alcohols were most abundant in the upper cliff part and decrease downwards. Sterol detection was difficult since the GC-MS was detecting a lot of background noise. Only α -Sitosterol and Campesterol were found in most of the samples. The absolute *n*-sterol concentration was at a mean of 51.43 $\mu\text{g/gSed}$. β -sitosterol is the most abundant *n*-sterol in all samples except SOB18-01-10 where *n*-sterol concentrations was generally extremely low. But the variation was quite high ranging from 1.58 $\mu\text{g/gSed}$ (SOB18-01-10; 19.7 m arl) to 278.85 $\mu\text{g/gSed}$. *N*-sterol trends viewed over the cliff section showed more abundance in upper cliff section with less *n*-sterols detected further down to the cliff base. *N*-alcohol and *n*-sterol concentrations showed similar trends. All data relating to the NSO fraction is showed in Figure 18.

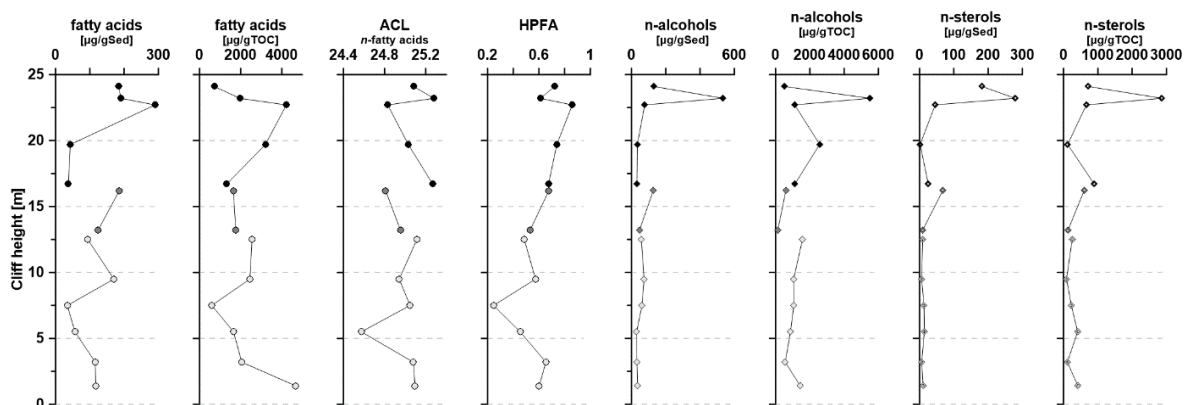


Figure 18: Overview of biomarker NSO fraction: *n*-fatty acids, alcohols and sterol concentration in $\mu\text{g/gSed}$ and $\mu\text{g/gTOC}$. Average Chain Length (ACL) and Higher Plant Fatty Acids (HPFA) indices for *n*-fatty acids. Data points are displayed over cliff depth from cliff top (25m) to cliff bottom (0m) at river level. The three sections of SOB18 are plotted separately for each parameter: SOB18-01 black circle, SOB18-03 dark grey circle and SOB18-06 light grey circle. Graphs have been created with Grapher 9.

With Spearman's rank correlation index, the correlation of selected degradation markers was tested (Figure 19) for TOC, $\delta^{13}\text{C}$ and $\text{CPI}_{\text{n-alkanes}}$ with C/N. A positive linear relationship between TOC wt% and C/N ratios as well as between $\delta^{13}\text{C}$ and C/N is visible, and negative linear relationship between $\delta^{13}\text{C}$ and C/N ratios. Table 2 shows values of Spearman's correlations coefficient ρ .

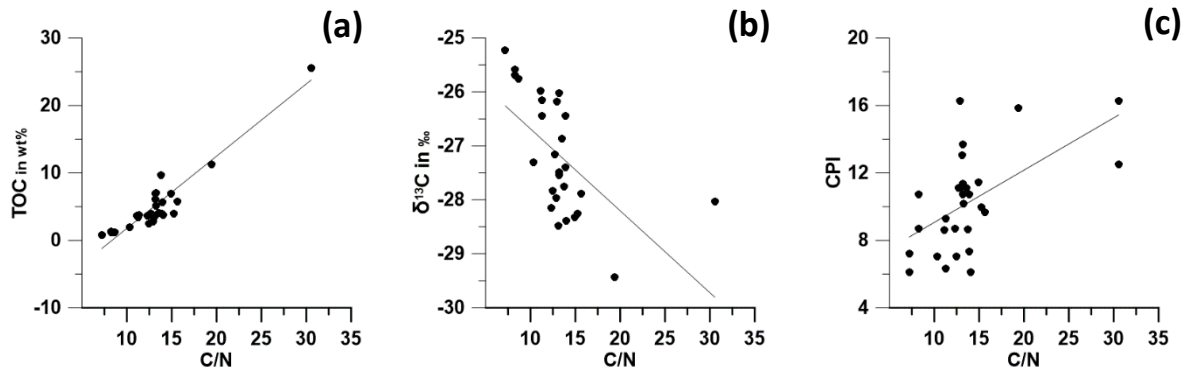


Figure 19: Scatterplots for selected organic matter degradation markers: (a) TOC (b) $\delta^{13}\text{C}$ and (c) CPI of n-alkanes are plotted over C/N ratios. Spearman's correlation test revealed positive relationship between TOC wt% - C/N as well as CPI - C/N and negative relationship between $\delta^{13}\text{C}$ - C/N. Graphs created with Grapher 9.

Table 2: Outcome of statistical testing with Spearman's correlation coefficient ρ for correlations of TOC/C/N, CPI/C/N and $\delta^{13}\text{C}$ /C/N. p-values for all selected degradation markers show statistical significance.

	TOC/C/N	CPI/C/N	$\delta^{13}\text{C}$ /C/N
Spearman's correlation coefficient ρ	0.732	0.526	-0.471
Correlation	Yes(+)	Yes(+)	Yes(-)

4.3 Water parameters

Conductivity, temperature & depth profiles from land-to-ocean

Water depth varied along the transect ranging from 2 to 18 meters and generally showed no consistent pattern moving nearshore. By contrast, water temperature and salinity profiles were similar along the transect, with mean values of 0.08°C and 20.63 PSU (excluding site CAC19-F; Figure 20). Measurements from CAC19-F were anomalously warm (2.17 °C) with unrealistically high salinity values (25.04 PSU) relative to samples collected before and after the site. Comparable CTD data from a second CTD confirmed those outliers. They were therefore excluded from further analysis (Figure 20).

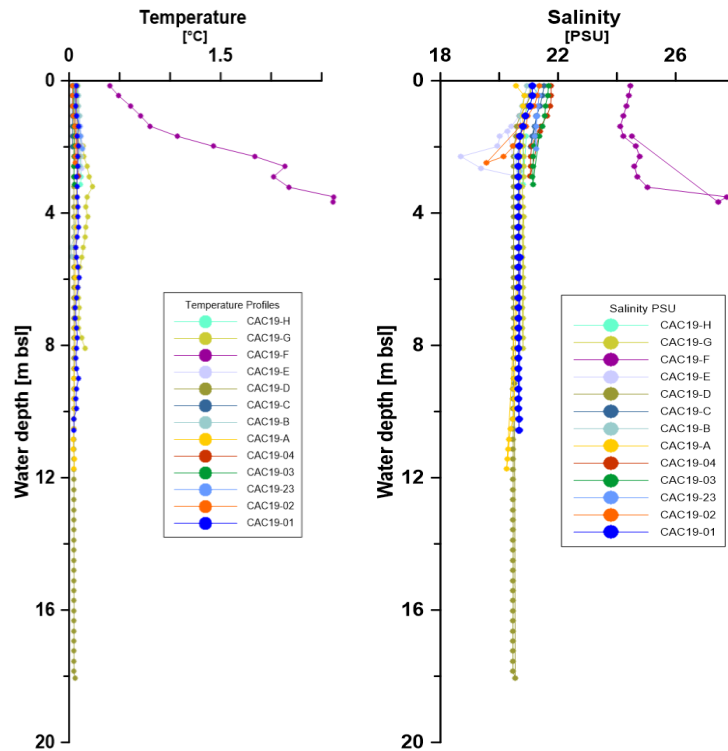


Figure 20: Temperature and Salinity Profiles across all stations from field conductivity, temperature and depth (CTD) measurements. All stations displayed similar temperature and salinity profiles, except CAC19-F, which was higher for both parameters.

4.4 Dissolved Organic matter

Total nitrogen (TDN), dissolved organic nitrogen (DON) and nitrate (NO_3^-) concentrations, determined using the denitrifier method, are displayed in Table 3. Only one depth per station was measured, which is also provided alongside mean hydrologic parameters (CTD) and dissolved organic carbon (DOC) measurements from the site.

All samples contained sufficient NO_3^- and TDN for reliable concentrations to be determined, allowing DON values to be calculated. Station CAC19-F was excluded from the following data analysis because of CTD data evaluation. Values for NO_3^- ranged between 6 $\mu\text{g/l}$ (CAC19-01) and 822 $\mu\text{g/l}$ (CAC19-H) with a mean concentration of 430 $\mu\text{g/l}$. Lowest TDN concentrations were 166.14 $\mu\text{g/l}$ at site CAC19-E and highest 586 $\mu\text{g/l}$ at site CAC19-23, with a mean of 290 $\mu\text{g/l}$. Calculated DON concentrations averaged 193 $\mu\text{g/l}$, with a wide range spanning 51 $\mu\text{g/l}$ (CAC19-E) to 479 $\mu\text{g/l}$ (CAC19-23). DOC concentrations were generally similar across all sites with a mean value of 6406 $\mu\text{g/l}$. Two stations, CAC19-F and CAC19-02 displayed elevated DOC values of 8544 and 7302 $\mu\text{g/l}$ respectively, and concentrations did not fall below 6015 $\mu\text{g/l}$ (CAC19-B).

Table 3: Nitrogen and carbon species in waters along the transect ordered by distance moving to the nearshore. All species concentrations are in $\mu\text{g/l}$ and salinity in PSU. Samples were collected at sample depth displayed below.

Station name	Longitude	Latitude	Sample depth m bsl	Temperature $^{\circ}\text{C}$	Salinity PSU	DOC $\mu\text{g/l}$	NO_3^- $\mu\text{g/l}$	TDN $\mu\text{g/l}$	DON $\mu\text{g/l}$
CAC19-H	128°23'86.5"	72°56'40.7"	3.00	0.11	20.81	6017	822	258	72
CAC19-G	128°35'32.4"	72°53'54.2"	7.50	0.09	20.79	6082	609	191	54
CAC19-F	128°49'21.6"	72°51'87.1"	3.00	2.17	25.04	8544	264	211	151
CAC19-E	128°62'96.8"	72°50'18.2"	2.50	0.13	19.39	5824	505	166	51
CAC19-D	128°69'45.6"	72°46'15.3"	10.00	0.05	20.48	6411	451	179	77
CAC19-C	128°84'44.7"	72°45'56.2"	2.00	0.03	21.07	6125	447	406	305
CAC19-B	128°97'10.8"	72°47'93.9"	5.00	0.02	20.70	6015	781	267	90
CAC19-A	129°10'15.9"	72°50'12.7"	7.00	0.06	20.59	6041	615	564	425
CAC19-01	129°24'79.1"	72°50'90.8"	6.00	0.07	20.66	6167	6	122	120
CAC19-02	129°54'56.8"	72°51'68.5"	2.60	0.06	19.57	7302	388	412	325
CAC19-23	129°69'30.5"	72°52'13.5"	2.30	0.13	21.27	6114	473	586	479
CAC19-03	129°84'20.3"	72°52'53.8"	3.00	0.05	21.14	6023	22	205	200
CAC19-04	129°86'38.5"	72°52'54.8"	3.00	0.10	21.06	6609	37	127	119
Mean						6405	417	284	190
Excluding CAC19-F						6227	430	290	193

Total concentrations of the different nitrogen species NO_3^- , TDN and DON respectively over a land-to-sea gradient spanning west to east are shown in Figure 21. Nitrate concentrations generally decreased from 822 to 37 $\mu\text{g/l}$ moving from the coast to the ocean. TDN concentrations overall showed an increase from the inner delta to outer delta, however few points show very low TDN concentrations in the nearshore that oppose this trend. DON concentrations demonstrated similar patterns to TDN, with generally increasing concentrations in the nearshore, with 72 $\mu\text{g/l}$ to 200 $\mu\text{g/l}$. DOC concentration appeared relatively consistent over the land to sea transect of all samples, except CAC19-F. No clear trend was observable for DOC concentrations across the transect with concentrations staying relatively constant moving from the coast to the ocean. There seems to be no clear relationship of concentration and depth. Low values of NO_3^- , TDN or DON were not associated with a lower or deeper sampling depth (Figure 21). Linear regressions were performed on NO_3^- , TDN, DON and DOC, but only NO_3^- and DON were found to be significant (p-value below 0.05). Linear regression results are shown in each plot respectively.

Therefore, the data was plotted in section plots to investigate depth relationship further in (Figure 22). Nitrate concentrations were elevated at mid-water depths (ca. 4-10 m) under river ice. NO_3^- concentrations were higher in the river interior, but decreased further east, and lower in the water column (as also depicted in Figure 21 a). A zone of higher NO_3^- concentrations of around 600 $\mu\text{g/l}$ was also apparent near the ice-water interface (1-2 m depth).

Values for TDN and DON appeared generally similar to NO_3^- concentrations, with higher concentrations in river waters which generally decreased toward the ocean. A clear increase in both TDN and DON was also observed at the ice-water interface at depths of 2-3 m with a concentration higher than 500 $\mu\text{g/l}$ (TDN) and 400 $\mu\text{g/l}$ (DON) (Figure 22 Fehler! Verweisquelle konnte nicht gefunden werden.).

DOC concentrations were low overall (<7000 $\mu\text{g/l}$) with no pattern in the nearshore or increases at the surface-ice interface (Figure 22). As noted above, two stations CAC19-F and CAC19-02 had elevated DOC values of >7000 $\mu\text{g/l}$. The section plot illustrates, that both stations were located in a water depth 2-4 m.

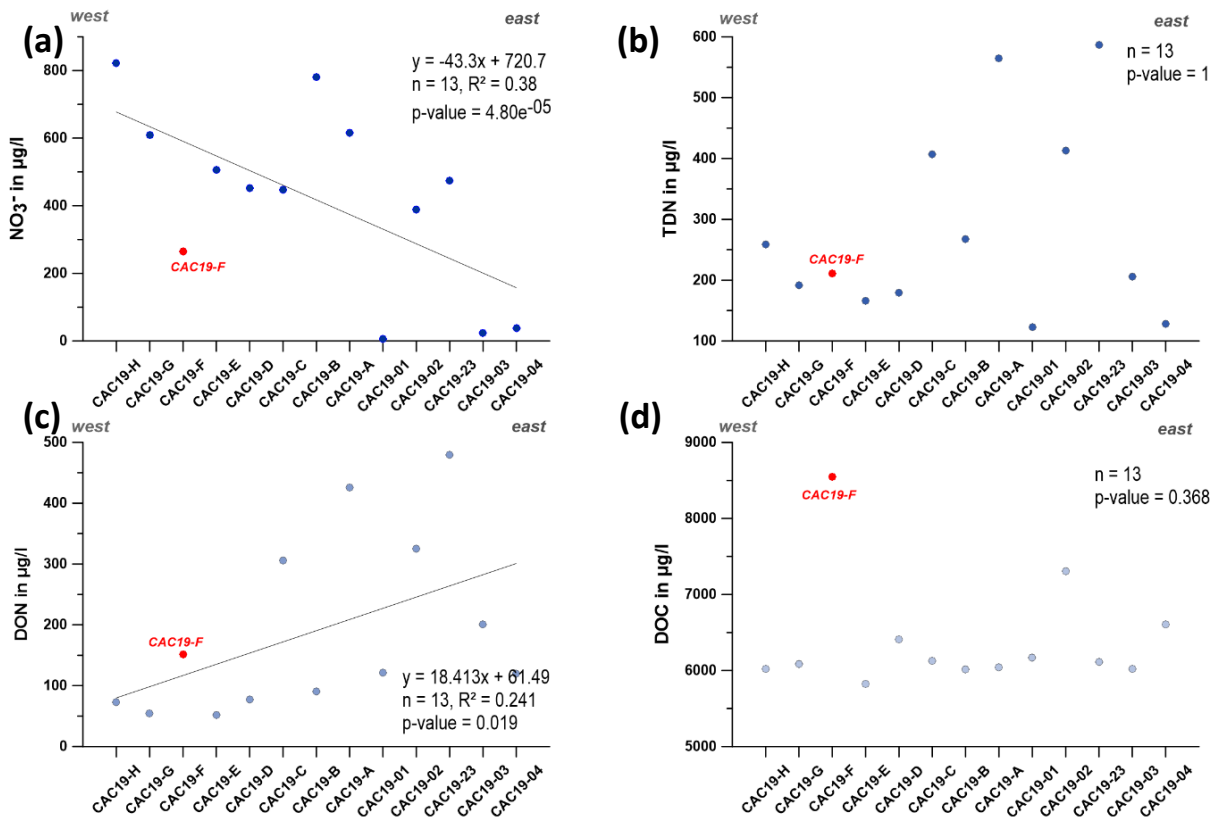


Figure 21: (a) Nitrate (NO_3^-), (b) Total Dissolved Nitrogen (TDN), (c) Dissolved Organic Nitrate (DON) and (d) Dissolved Organic Carbon (DOC) in $\mu\text{g/l}$ are shown geographically from inner delta (CAC19-H) seawards to the outer delta (CAC19-04). Trend lines show a pronounced decrease in nitrate seawards, a slight increase in TDN seawards and an increase of DON seawards. DOC concentrations stay approximately the same over the west-east transect. Each plot shows linear regression results: regression equation, r^2 , sample number (n) and p-value. Graphs were plotted in Grapher 9.

Since DIVA interpolation takes into account coastlines and bathymetry features to structure and subdivide the domain in comparison to other interpolation techniques, plots sometimes do not seem to follow the exact measured data point (e.g. Figure 22a - very high concentrations at 4-8 m with $\sim 20\text{-}35$ km distance but data point is at 5 m at ~ 35 km). It extrapolates zones of higher concentration in greater depth on the basis of one data point. Thus we have to treat those zones of elevated concentrations with caution. One data point might easily be an outlier.

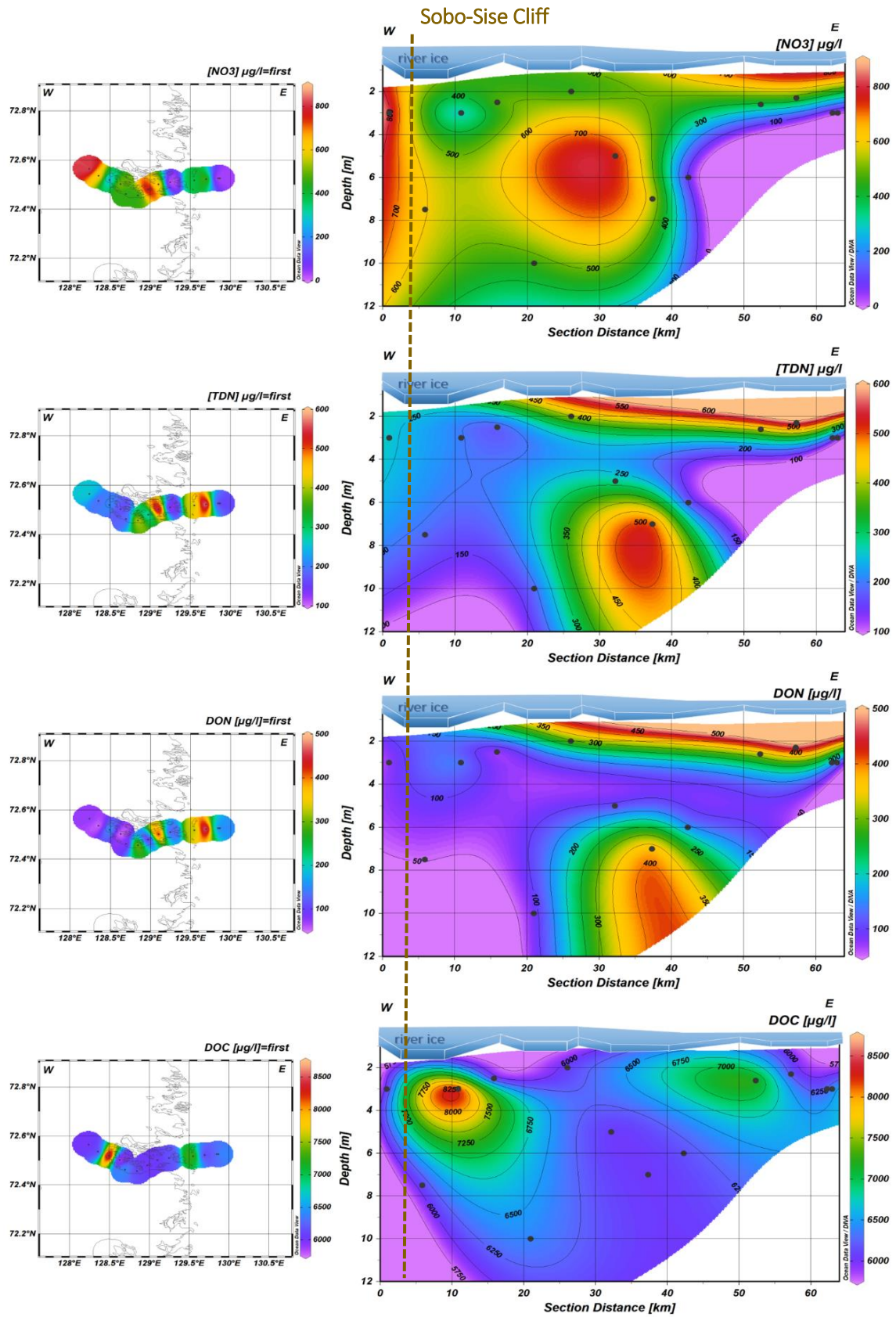


Figure 22: Surface and section plots of (a) NO_3^- , (b) TDN, (c) DON and (d) DOC concentrations in $\mu\text{g/l}$ over water depth in the Lena Delta. Respective section plots show W-E transect in the river channel with a river ice layer on top. In white areas, DIVA exploration did not reach. Maximum water depth is 10 m. Surface and Section Plots were created with ODV.

4.5 Nitrogen Isotopic Signatures

The use of nitrogen isotopes on the samples, analysed as part of this study, will help determine the processes behind nitrogen release from permafrost thaw as well as the in river processing and differentiating it from dilution effects. The results of the dual isotope analysis on the same samples are shown in this section. Different isotopic signatures were identified over the west to east transect (Figure 23). In some cases (Table 4) nitrate isotopic concentrations were $<1 \mu\text{M}$ (BDL-below detection limit) and therefore $\delta^{18}\text{O}-\text{NO}_3^-$ could not be determined in 3 samples. Further, it is important to note that $\delta^{15}\text{N}$ for in CAC19-F and CAC19-23 was not measured accurately in our analysis, which led to excluding it from further analysis.

$\delta^{15}\text{N}$ -TDN and $\delta^{15}\text{N}-\text{NO}_3^-$ values are quite close to each other in many of the sampled points and often within error of each other. Calculating DON from that would result in an extremely low DON-value, when the actual value is likely to be fairly similar to the TDN values (Appendix 8.5). TDN includes the fully dissolved organic and inorganic nitrogen pools (see 2.4). Considering this, it can be assumed that most of the TDN isotopic values are made up by DON isotopic fractionation. Therefore it is assumed here for simplicity reasons, that the nitrogen isotopic signature of DON is roughly equal to the signature of TDN ($\delta^{15}\text{N}-\text{DON} \approx \delta^{15}\text{N}-\text{TDN}$).

Table 4: Overview of isotopic signatures for $\delta^{15}\text{N}-\text{NO}_3^-$, $\delta^{18}\text{O}-\text{NO}_3^-$ and $\delta^{15}\text{N}-\text{TDN}$. BDL – Below detection limit. EX- excluded from analysis. All values are in ‰.

Sampling depth	Station	$\delta^{15}\text{N}-\text{NO}_3^-$	$\delta^{18}\text{O}-\text{NO}_3^-$	$\delta^{15}\text{N}-\text{TDN}$
M BRL		‰	‰	‰
3	CAC19-H	3.27	-12.96	3.05
7	CAC19-G	3.14	-13.15	2.84
3	CAC19-F	2.25	-12.72	EX
2.5	CAC19-E	3.17	-12.99	1.62
10	CAC19-D	3.12	-12.91	2.98
2	CAC19-C	3.44	-12.66	2.69
5	CAC19-B	3.54	-12.68	3.07
7	CAC19-A	3.41	-12.47	1.89
6	CAC19-01	BDL	BDL	2.10
2.6	CAC19-02	3.30	-12.44	2.08
2.3	CAC19-23	3.50	-12.51	EX
3	CAC19-03	BDL	BDL	2.92
3	CAC19-04	BDL	BDL	1.20
MEAN		3.21	-12.75	2.40

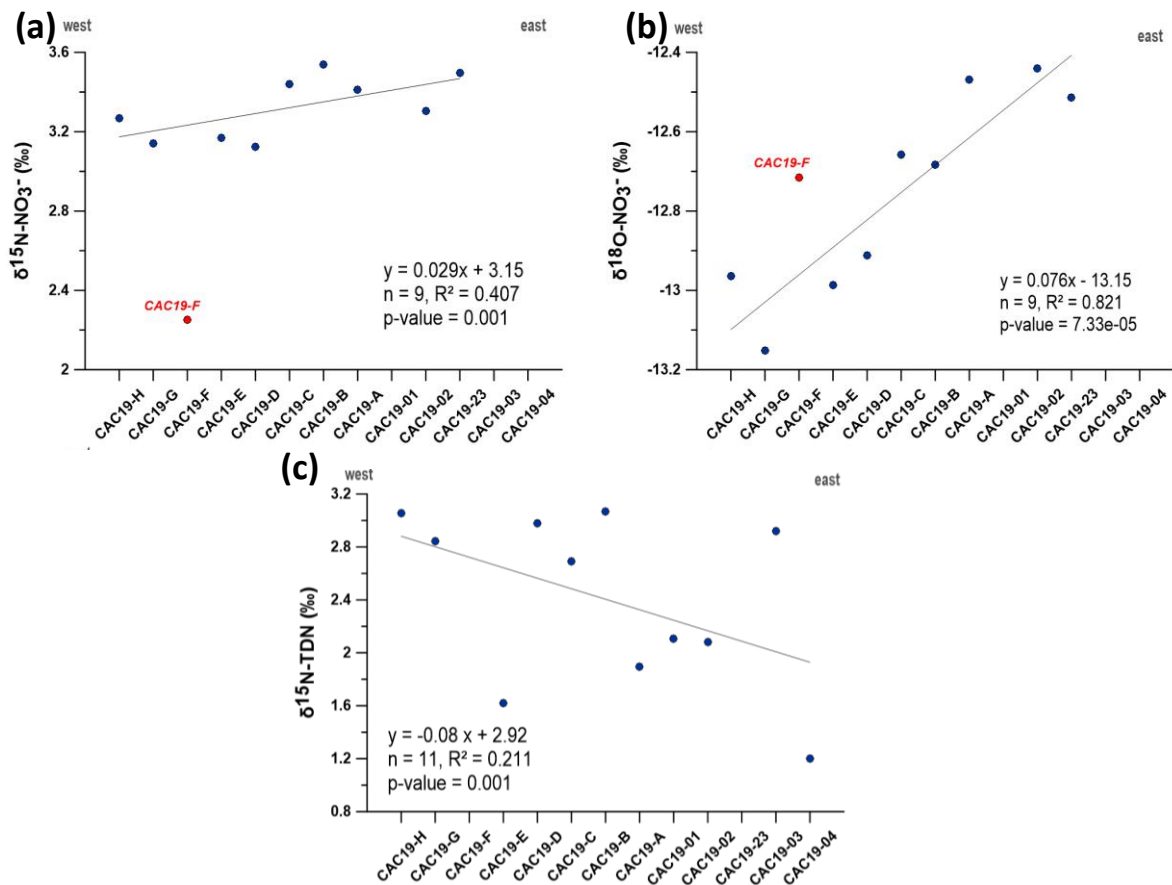


Figure 23: Nitrogen Isotopic Signatures for (a) $\delta^{15}\text{N-NO}_3^-$, (b) $\delta^{18}\text{O-NO}_3^-$ and (c) $\delta^{15}\text{N-TDN}$ in ‰ are shown from west to east. Trend lines show a pronounced overall decrease in $\delta^{15}\text{N-NO}_3^-$ and $\delta^{18}\text{O-NO}_3^-$ to the east and a decrease in $\delta^{15}\text{N-TDN}$ from west to east. CAC19-F is shown in red and not included in the linear regression and excluded for (c). Graphs were plotted in Grapher 9.

Nitrogen isotopes of all species were positive. Values for $\delta^{15}\text{N}$ of NO_3^- ranged between 3.12 to 3.54 ‰, excluding CAC19-F with the only low value of 2.25 ‰. If excluding the latter, values showed a good consistency over the transect, with a lot fluctuation, and a slight increasing trend seawards. Oxygen isotopes were highly negative ranging between -12.44 and -13.15 ‰. The trend line illustrates a steep decrease to less negative values from inner to outer delta. $\delta^{15}\text{N-TDN}$ values were generally slightly lower than values for $\delta^{15}\text{N-NO}_3^-$ with a mean of 2.40 ‰ and a range between 1.20 to 3.07 ‰. The TDN trend line shows a lighter isotopic signature towards the east, although there are a few fluctuations. All linear regression show p-values below 0.05 and are significant.

4.6 Organic Matter processing

To identify how organic matter varied with height over the Sobo-Sise Cliff, and how dissolved organic matter constituents varied during transit to the nearshore, the two datasets were separately grouped into subunits by clustering as described in 3.8.1 for terrestrial and aquatic data separately.

4.6.1 OM of Sobo-Sise Cliff

For permafrost samples agglomerative hierarchical clustering identified two main sub-groups within the 27 samples (Figure 24 a). Group I represented the upper cliff unit from 24 until 14 m.a.r.l and group II, the lower cliff unit from 13 to 0 m.a.r.l. One sample was excluded because it had been below TOC detection limit (<0.1 wt %). Based on the cluster result, boxplots for TOC and absolute *n*-alkane concentrations were produced (Figure 24). TOC values concentrated around 5 wt % for both groups (Figure 24 b). But group II shows less variation compared to group I. Absolute *n*-alkane concentration in $\mu\text{g/gSed}$ was used to represent biomarkers. The groups showed significant difference in concentration. Group I of the upper cliff representing less biomarker concentration compared to group II of the lower cliff.

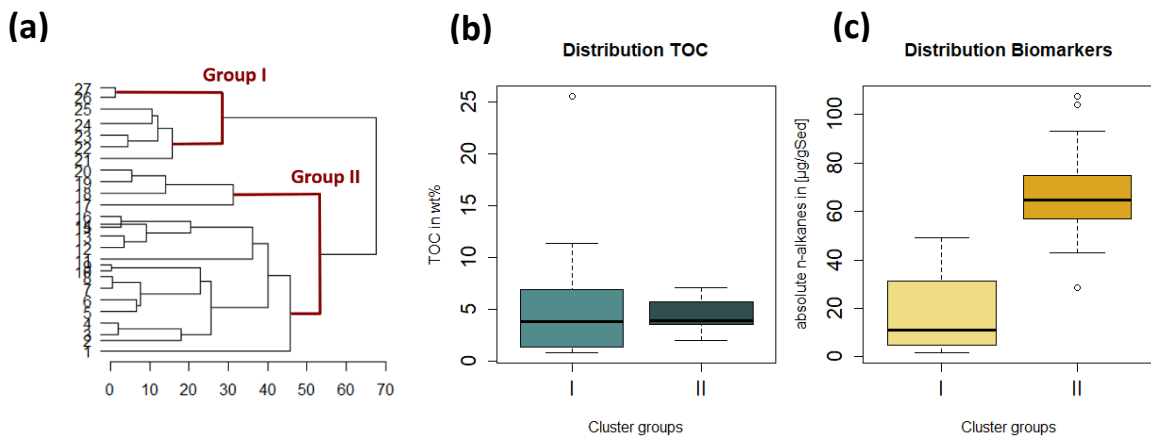


Figure 24: (a) Clustering of permafrost samples with y-axis representing cliff height in m.a.r.l. meaning group I represents the upper cliff part and group II the lower. Resulting boxplots allow better visualisation of organic matter distribution over the height of Sobo Sise Cliff: (b) Total Dissolved Carbon (TOC) in wt% and (c) absolute *n*-alkane concentration in $\mu\text{g/gSed}$ representative for all biomarkers. Boxplots show TOC values for the two groups relatively aligned but with less variation in group II. Biomarker cluster groups show significant difference in concentration, but have similar variation. Graphs were created with R Studio.

Significant differences between the subunits were then identified by the application of the non-parametric Kruskal-Wallis-Test. If p -value is ≤ 0.05 , the difference of medians is statistically significant. We reject the null hypothesis and conclude that medians are not at all equal. If p -value is ≥ 0.05 the difference between the medians are not statistically significant. Medians are equal and we do not have enough evidence to reject the null hypothesis. The Kruskal-Wallis rank sum test revealed significant differences between *n*-alkane medians, but no statistical significance between TOC. Results of the Kruskal-Wallis test can be viewed in Table 5.

Table 5: Results of Kruskal-Wallis rank sum test for terrestrial samples (TOC, n-alkanes) with p-value, degrees of freedom (df) and significance statement.

Kruskal-Wallis rank sum test	TOC	n-alkanes
H-value	0.0995	17.416
p-value	0.3946	3.003e-05
df	1	1
Significance?	no	yes

4.6.2 OM during fluvial transit

Agglomerative hierarchical clustering identified two main sub-groups for water samples as well. This approach helps to achieve greater resolution into how OM processing varied moving to the nearshore. Boxplots were created for NO_3^- and DON distribution (Figure 25). DOC and TDN have not been plotted because they did not prove to be significant. All plots exclude CAC19-F. Cluster shows grouping into two groups (Figure 25), where group I represents the first 8 samples from the inner delta, and group II the last 4 in the nearshore zone. This can be viewed in Figure 7. In accordance with findings from Figure 21, where NO_3^- concentration decreased and DON concentration increased seawards, we see in the boxplots that the last 4 samples form cluster II and pose a significant impact on the overall transect in terms of difference from cluster I. A two sample t-test with unequal variances has been performed to test significance of cluster analysis. Results can be found in Table 6.

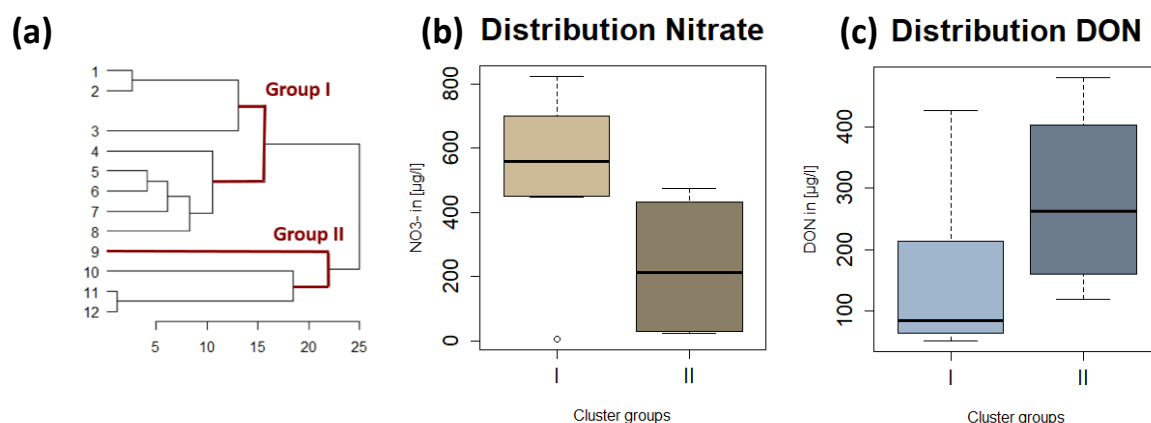


Figure 25: Boxplots allow better visualisation of organic matter distribution: (a) Clustering result for water samples with y-axis representing sample number and at the same time the geographical order from west to east. Resulting boxplots allow better visualisation of organic matter distribution in 2 groups: (b) Nitrate (NO_3^-) in $\mu\text{g/l}$ (c) Dissolved Organic Nitrogen (DON) in $\mu\text{g/l}$. Graphs were created with R Studio.

Boxplots were also created for $\delta^{15}\text{N}-\text{NO}_3^-$, $\delta^{15}\text{N}-\text{TDN}$ and $\delta^{18}\text{O}-\text{NO}_3^-$ distribution (Figure 25) since all isotopes proved significant in Figure 23. All plots exclude CAC19-F.

Table 6: Results of two sample t-test with unequal variances for N species (Nitrate, DON) and all N isotopes, p-value. T-statistic and significance statement.

Two parametric t-test	NO_3^-	DON	$\delta^{15}\text{N}-\text{NO}_3^-$	$\delta^{18}\text{O}-\text{NO}_3^-$	$\delta^{15}\text{N}-\text{TDN}$
Mean I	530.05	149.86	3.29	-12.83	2.53
Mean II	230.29	281.17	3.40	-12.47	2.06
t-statistic	2.032	-1.417	-0.859	-3.728	0.863
p-value	0.040	0.1078	0.240	0.003	0.225
Significance?	yes	no	No	yes	no

Nitrogen isotope species results are covered in section 4.5. Boxplots resulting from cluster analysis help to shed light on their distribution over the different proximity to Sobo-Sise Cliff. $\delta^{18}\text{O}$ of NO_3^- values showed an increasing trend to less negative values, with the most negative values closest to the cliff, meaning an enrichment in the heavy $\delta^{18}\text{O}$ from cluster I to cluster II. The dominant pool in cluster I was $\delta^{15}\text{N}$ of Nitrate ($\sim 3.28\text{‰}$), whereas the median of $\delta^{15}\text{N}$ of TDN ($\sim 2.5\text{‰}$) was lower. Cluster II exhibited increased $\delta^{15}\text{N}$ values for the nitrate cluster median ($\sim 3.4\text{‰}$) and a decrease of $\delta^{15}\text{N}$ -TDN ($\sim 2\text{‰}$), where nitrate isotopes were again the dominant pool.

Applying a two sample t-test with unequal variances for the clusters concerning N species and also isotopic signatures yielded statistical significance for Nitrate and $\delta^{18}\text{O}$ - NO_3^- , but no significance for DON, TDN, $\delta^{15}\text{N}$ - NO_3^- and $\delta^{15}\text{N}$ - TDN.

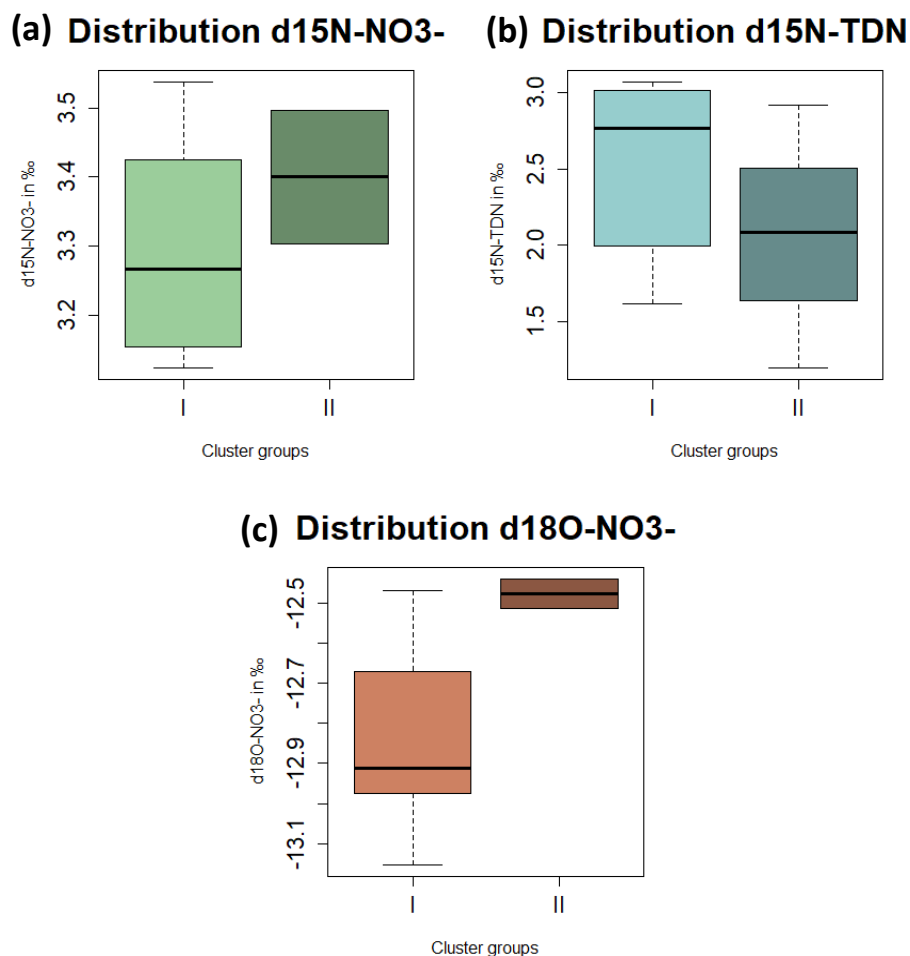


Figure 26: Boxplots resulting from cluster analysis of (a) $\delta^{15}\text{N}$ - NO_3^- ; (b) $\delta^{15}\text{N}$ -TDN and (c) $\delta^{18}\text{O}$ - NO_3^- all in ‰ over west to east transect different proximity from Sobo-Sise Cliff. The absence of variation bars in graphs are due to low sample number. Graphs were created with R Studio.

5 Discussion

In the following section, the three main foci of the thesis will be discussed in detail: In 5.1, I will characterise the terrestrial organic matter of permafrost using lipid biomarker and sedimentological proxies to define (i) potential source and (ii) quality of stored carbon in Sobo-Sise Cliff yedoma exposure. In 5.2, nitrogen isotope signals in the river waters close to the studied permafrost are discussed to (iii) assess a seasonal snapshot, (iv) to relate carbon and nitrogen compounds to permafrost as potential source and (v) to identify nitrogen cycling pathways in permafrost thaw zones.

5.1 Terrestrial Focus

5.1.1 Depositional environment

The Sobo Sise Cliff shows distinct geomorphological features (Figure 5): Yedoma sites alternating with thermoerosional valleys or thermoerosional depressions. Combined with the presence of ice wedges that are exposed at the cliff, it appears that organic matter accumulation and preservation are most likely caused by syngenetic permafrost formation in polygonal tundra landscapes over long periods in the Quaternary (Jongejans et al., 2018; Strauss et al., 2015; Schirrmeister et al., 2011, 2020).

Schirrmeister et al., (2011) attributed parts of the third delta sedimentological unit in the western and southern parts of the Lena River Delta to be remnants of a Yedoma Ice Complex accumulation plain that formed during the LGP in the Late Pleistocene when the river had its delta much farther north (Schirrmeister et al., 2011). Radiocarbon ages of this study confirmed that time line holds true for Sobo-Sise Cliff with 48899 cal BP in the lower cliff parts, where the main part of the cliff most likely formed. Much younger ages for the upper cliff (4443 to 6373 cal BP) reveal ages from the late/mid Holocene.

TOC, TN and C/N variation are the result of changes in bioproductivity, character of cryosol formation, different degrees of organic matter deposition or point to different plant sources. TOC, TN, C/N, and $\delta^{13}\text{C}$ overall show little variation ranging from 0.82 to 25.51 wt %, 0.11 to 0.83 wt %, 7.2 to 30.55 and -29.43 to -25.22 ‰, respectively. I suggest relatively stable depositional environment for the studied deposits. It is likely, grain size is similar to surrounding areas belonging to the same units as described by Wetterich et al. (2008) for Lena Delta and Fuchs et al. (in prep.) for Sobo-Sise Cliff.

High TOC contents and high C/N ratios associated with low $\delta^{13}\text{C}$ values reflect less-decomposed organic matter (Schirrmeister et al., 2011, 2013). TOC values are partially high (5.12 wt %; ranging from 0.82 to 25.51 wt %, Figure 18) and as well as C/N (13.24, ranging from 7.2 to 30.55, Figure 15). The following sites were cryolithologically analysed by (Schirrmeister et al., 2011): Khardang Sise, Ebe Basyn Sise and Kurungnakh Sise. They yield similar results for TOC (0.1-8.6, 0.1-22.8, and 1.1-11.7 wt % respectively) and also C/N values for respective sites (7.6-32.7, 2.9-18.8, and 5.2-23.2), which reflects a variable degree of organic matter decomposition. Figure 27 puts Sobo Sise Cliff in relation to other yedoma sites across Siberia and Alaska by considering TOC values. It is significant that Sobo Sise Cliff shows the highest mean TOC (5.12 wt %), especially in respect to other sites from the central Lena Delta (Kurungnakh, Ebe Basyn and Khardang Island); here Kurungnakh Island shows mean TOC (4.8 wt %) that matches Sobo Sise the most.

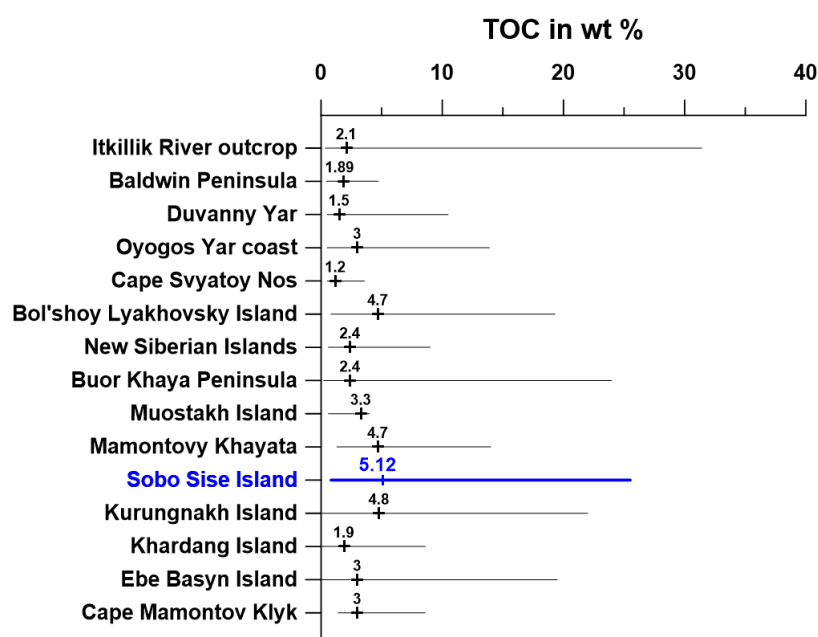


Figure 27: TOC variations from different yedoma study sites in Siberia and Alaska in comparison to Sobo Sise Cliff data from this study (in blue). Sites sorted from east (Itkillik River outcrop, Alaskan North Slope) to west (Cape Mamontov Klyk, western Laptev Sea). Data compiled from (Jongejans et al., 2018; Schirrmeister et al., 2011; Schirrmeister, Grosse, et al., 2008; Schirrmeister, Kunitsky, et al., 2008; Strauss et al., 2015; Strauss et al., 2013). Graph was created with Grapher 9.

Very high values of TOC (25.51 wt %), TN and C/N and low $\delta^{13}\text{C}$ (-28.03 ‰) in the top most samples are attributed to recent OM quality presence and is most probable influenced by the active layer. Here the organic material is freshest and of best quality.

High $\delta^{13}\text{C}$ and corresponding low TOC and C/N values are typical for yedoma exposures (Dutta et al., 2006; Vonk et al., 2013) and evidence for cold stages, during which TOC was less variable and generally low, indicating more stable environments with reduced bioproductivity and therefore low C/N ratios. This signature is characteristic of stadial periods with decreased productivity and a dry climate (Schirrmeister et al., 2011, 2013). A local TOC peak has 11.31 wt% (16.2 marl, SOB18-03-05), where $\delta^{13}\text{C}$ ratio is lowest (-29.43 ‰). This is likely one of the palaeosoil layers with peat occurring in yedoma (Strauss et al., 2012) rather than a sign of a shift in the depositional environment. Having in mind not putting too much weight on a single sample but considering a paleoenvironmental study by Wetterich et al., (2008), this phenomenon could be affected by relatively warm summers, climate optimisation and also be indication for the presence of small ponds during the Kargin climate optimum between 40 and 32 kyr BP.

5.1.2 Organic matter quality

Organic matter is preserved in permafrost, which in turn preserves the organic matter decomposition state. When analysing the OM composition of sediments, the OM quality can be determined. The source of OM influences both the quantity as well as the quality of OM (Jongejans et al., 2018).

n-alkanes exhibit strong odd over even predominance and long over short predominance. Most abundant chains are *n*-C₂₇, *n*-C₂₉ and *n*-C₃₁ (Figure 17 a). The analysis showed high values for the ACL₂₃₋₃₃ (>25.8), both statements suggests that the organic matter is primarily derived from terrestrial higher plants (Eglinton & Hamilton, 1967; Killips & Killips, 2013). The CPI₂₃₋₃₃ (mean 10, maximum 16) when compared to other yedoma sites (Jongejans et al., 2018; Stapel et al., 2016) can be classified as quite high. The high CPI is characteristic for yedoma deposits and indicates fresh and less degraded terrigenous organic matter (Brassell et al., 1978). The overall low amounts of short-chain homologues

($n\text{-C}_{17}\text{--C}_{20}$) indicate minor contributions of *n*-alkanes from algae and bacteria (Cranwell et al., 1987). Several paleo-botanical analyses (Andreev et al., 2002; Schirrmeister, Grosse, et al., 2008; Schirrmeister, Kunitsky, et al., 2008; Wetterich et al., 2008) attribute the organic matter composition of Yedoma in north eastern Siberia to be dominated by plant material derived from herbs (such as Artemisia, Carophyllaceae and Asteraceae), grasses (Poaceae, Cyperaceae) and to a smaller portion dwarf shrubs (e.g. Salix, Alnus, Betula).

Although only half of the samples that were analysed for aliphatics were also analysed for NSO compounds, *n*-fatty acids as well as *n*-alcohols and *n*-sterols appear on average at a higher concentration than *n*-alkanes. Some argue (Routh et al., 2014) that more labile compounds like *n*-alcohols and *n*-fatty acids are degraded to *n*-alkanes and hence an increased amount of *n*-alkanes would be an indicator for cumulative decay (Strauss et al., 2015). Since this is not the case here, I argue, that OM has been preserved well. The $ACL_{n\text{-fatty-acid}}$ (25.0) aligns with $ACL_{n\text{-alkanes}}$ (>25.8) as does the dominance of long chain *n*-fatty acids over short chain *n*-fatty acids with those of *n*-alkanes respectively. This also supports the statement that OM is very little degraded.

The HPFA index was introduced by Strauss et al., (2015), derived from the HPA index by Poynter, (1989) which has been tested for the Arctic environment (Routh et al., 2014), is a viable index of the relative amount of the labile fatty acids that remain in a sample. It shows quite a range (0.25 - 0.86) and a slight decreasing trend over the profile. This means lower HPFA values in the lower cliff translate to less abundant fatty acids and therefore a higher degradation state. Therefore, higher HPFA in the upper cliff means organic matter is less degraded. In general the HPFA values of this study compare well to values from Strauss et al., (2015) (0.15-0.69) which seem to be characteristic for yedoma deposits. Lower values in uppermost samples just below the cliff top might be caused by very recent degradation of organic matter. This might be caused by Holocene fluctuations in temperature or influenced by the active layer. *n*-alcohols are dominated by even chains *n*-C₂₆ and *n*-C₂₈ which is an indicator for land plant input (Rielley et al., 1991; Zheng et al., 2007). Moreover, the presence of *n*-sterols such as β -sitosterol, stigmasterol, campesterol, and brassicasterol indicates the origin of OM from higher plants and mosses (Lehtonen & Ketola, 1993; Rielley et al., 1991). *n*-alcohols and *n*-sterols follow the same trend over cliff height but pose an inverse relationship to that of *n*-alkanes. It has been discussed that proportion of even chain *n*-alkanes increased in oxygen-poor conditions (Lehtonen & Ketola, 1993). Since *n*-alkanes show the opposite trend and the one-carbon atom loss is not happening here, subsequent degradation of *n*-alkanes is not evident and together with good preservation of all NSO compounds, it can be concluded that OM quality is high.

During the assessment of OM quality with different biomarker indices in this study, it has been found, that overall OM quality of Sobo-Sise Cliff is high and shows little to no degradation trends. Statistical testing via clustering and application of Kruskal-Wallis test for TOC median values over the identified cluster groups (equally distributed on average, Figure 24) confirmed this. Further, indices such as CPI which is a measure of alteration of organic matter, exhibit no distinct depth trend. CPI and ACL were also plotted and did yield results supporting freeze-locking (Appendix 8.7 **Fehler! Verweisquelle konnte nicht gefunden werden.**): mean values for upper and lower cliff are relatively the same, but with high variation. Thus minimal or no decomposition has occurred before or after the OM was incorporated into the permafrost, meaning its high quality was maintained (Jongejans et al., 2018; Stapel et al., 2016; Strauss et al., 2015). When OM was initially incorporated in the Yedoma deposit, it was literally frozen in place. This has been previously described for ice rich yedoma deposits (Jongejans et al., 2018; Stapel

et al., 2016; Strauss et al., 2015) and resulting in the assumption that the OM is protected against microbial alteration.

However, the Kruskal-Wallis test yields a different result for *n*-alkanes. Different medians for *n*-alkanes were proved significant and lead to assumed higher *n*-alkane abundance in the lower cliff which in turn indicates lower OM quality. The explanation for this is not straight forward. Keeping in mind the principle of superposition, it seems likely the reason is the organic matter degradation state. Meaning lower cliff parts formed earlier had more time to degrade and therefore yield higher *n*-alkane concentrations.

A study from Kurungnakh Island in the Lena Delta confirmed the presence of living bacteria and archaea in yedoma deposits of the Siberian Arctic by looking at microbial life marker signals in order to investigate the link between the methane dynamics in permafrost deposits and climate change (Bischoff et al., 2013), hence proved the presence of microbial activity. Nevertheless, this would oppose the above mentioned instant freeze-locking of the OM in the permafrost.

Holding both statements true, this leads to the assumption, that although OM has been frozen in situ, it was either exposed to extremely slow degradation over time in the lower cliff, since *n*-alkane concentration is higher and OM quality is lower here. Or there has been fluctuating OM input during initial deposition of sediments and organic matter. All the same, this would oppose the original assumption of a stable depositional environment.

5.1.3 OM at the permafrost to river interface

Grosse et al. (2011) supposed an increasing occurrence in and magnitude of disturbance processes, because of ongoing climate warming in the Arctic, especially for fire and thermokarst accelerating permafrost degradation. Sedimentological as well as biomarker analysis of this study proved that Sobo Sise Cliff has a low degradation state of organic matter and definitely is an OM source. This means the vulnerability of OM to microbial degradation after permafrost thaw is expected to be significant.

Organic matter becomes available with thaw and is exported in dissolved form by suprapermafrost and river systems. Dissolved OC (<0.45 µm) in ancient Yedoma is exceptionally bioavailable (Mann et al., 2014; Vonk et al., 2013). Organic matter parts that are not dissolved can occur as suspended particulate organic matter (> 0.45 µm). Eroded ancient organic matter could be protected from extensive degradation by organo-mineral bonds, which are most important for organic matter stabilization (Höfle et al., 2013) and have the ability to weight down OM and promote their rapid settling in aquatic environments (Vonc et al., 2010). The study by Vonk et al. (2010) investigated degradation proxies of terrestrial organic carbon in respect to radiocarbon ages and their signature as dissolved carbon. They suggest that degraded but young terrestrial OC pool in surface waters is underlain by a less degraded but old terrestrial OC pool in bottom sediments. Surface water signatures are attributed to surface soil erosion and recent vegetation fluvially released as buoyant organic-rich aggregates (e.g., humics), which are subjected to extensive processing during coastal transport (Vonc et al., 2010). The terrestrial OC in the underlying was postulated to originate predominantly from erosion of mineral-rich Yedoma coasts of Pleistocene age and inland mineral soils. Although this study was conducted in the Kolyma River, with evidence provided by this thesis, I can see similarities for the Lena Delta.

Erosion rates for Sobo-Sise yedoma cliff were calculated for a mean long-term (1965-2018): 9.1 m/yr with locally and temporally varying rates of up to 22.3 m/yr (Fuchs et al., in review). The latter exceeds all previously reported rates for Arctic rivers and is among the highest for permafrost river and coastal shoreline stretches. The dominant erosion mechanism is fluvio-thermal, especially during summer; warm water from the river catchment triggers the formation of thermo-erosional niches at the base of

the cliff. Specific configuration of river flow direction and cliff shore orientation enhances local erosion intensity.

Kurungnakh Island for comparison has much smaller erosion rates with 4.1 to 6.9 m/yr (Stettner et al., 2018) with most of the erosion taking place by thaw slumping (Fuchs et al., in review). The Olenekskaya channel that flows around Kurungnakh Island has a low runoff rate and therefore weaker river currents compared to the Sardakhskaya channel (Fedorova et al., 2015). It is important to highlight that those erosional mechanisms acting in a river setting are different than the ones in a coastal environment. Here, erosion mechanisms are mainly thermo-denudation (thawing of exposed permafrost with propagation of a retreating headwall influenced by insolation and heat flux) and thermo-abrasion (defined as the combined action of mechanical and thermal energy of sea water at water level (Günther et al., 2015)). In particular, the moving river water of the Sardakhskaya channel leads to fast removal of eroded debris at the cliff base, allowing continuous erosion at the base by the warm river water in summer.

The Lena River is ice covered during winter and very little erosion happens compared to the spring ice break up. Ice thickness is up to 2 m while the water depth around 11 meters in front of the cliff allowing constant water flow underneath also in winter (Fuchs et al., in review). Presumably erosion is present also in winter, but erosion rates are not specifically known.

Fuchs et al. (in review) further finds that up to 41.3×10^3 kg DOC is eroded annually (2015-2018) into the Sardakhskaya channel posing potentially bioavailable C, which is released into the riverine ecosystem and transported to the nearshore area of the Laptev Sea.

This study was conducted in a winter scenario, thus a DOC signal of that magnitude and annuality is not recorded here. However there was a constant but low DOC signal detected, which is most likely a residual summer signal. Another possibility could be, that reported DOC stems from resuspension of OC deposited in the river bank during summer.

5.2 Aquatic Focus

5.2.1 Winter Signal in the Lena River

The presented biogeochemical investigation of the west to east transect in the Sardakhskaya channel of the Lena Delta has been done during late March to early April in 2019. This means the study represents a seasonal snapshot when the river is covered with ice. It is a snapshot, but one in a season with sparse field data.

Juhls et al. (2020) investigated drivers of seasonal hydrochemistry in the Lena River and found strong seasonal variations of biogeochemical parameters. Although a mean annual discharge of $21\,885 \text{ m}^3 \text{ s}^{-1}$, the winter discharge of the Lena River is low ($<6\,000 \text{ m}^3 \text{ s}^{-1}$) (Juhls et al., 2020). A distinct sign for steady winter discharge is the open water segment in front of the Sobo Sise Cliff, as recorded in the field (Figure 29). Mean temperatures (0.08°C) and salinity (20.63 PSU) of this study are in accordance of their seasonal mean river water signature during ice-cover (slightly below 0°C ; -0.2 Juhls et al., 2020). Dissolved organic matter values being consistently low overall ($6405.83 \mu\text{g/l} = 6.4 \text{ mg/l}$), are typical for a winter signal ($\sim 6\text{--}7 \text{ mg/l DOC}$; Juhls et al., 2020). Relatively stable $\delta^{18}\text{O}$ values in river water around -21 ‰ and high d-excess values (10.5) confirm the winter signal as described in Juhls et al. (2020).

The concentrations of nitrate and DON represent the dissolved inorganic and the dissolved organic species of TDN respectively, both were detected in all samples. Nitrate concentrations decrease over the west to east transect and nitrate is the dominant species close to the cliff (cluster I) where its concentration is almost 6x greater than DON (Figure 25 c compared to d). Further downstream marking

the shelf area with cluster II, nitrate medians decrease while DON increases. The dominant species is now DON, exceeding NO_3^- by ~ 80 $\mu\text{g/l}$. A single outlier of extremely low NO_3^- in cluster I seems anomalous in comparison to the rest of the samples.

Currently degrading permafrost facilitates the release of large amounts of both nitrate and DON from the soil (Francis, 2019), resulting in high concentrations of both nitrogen species in the dissolved phase. In this study however, the dissolved phase shows different relative amounts of both N species in respective clusters. Cluster analysis divided the water transect into two environments (Figure 28): delta interior (cluster I) and river nearshore (cluster II). From Figure 25 and Figure 26, a unique permafrost thaw signal can be detected using concentrations and isotopic signatures of nitrogen species:

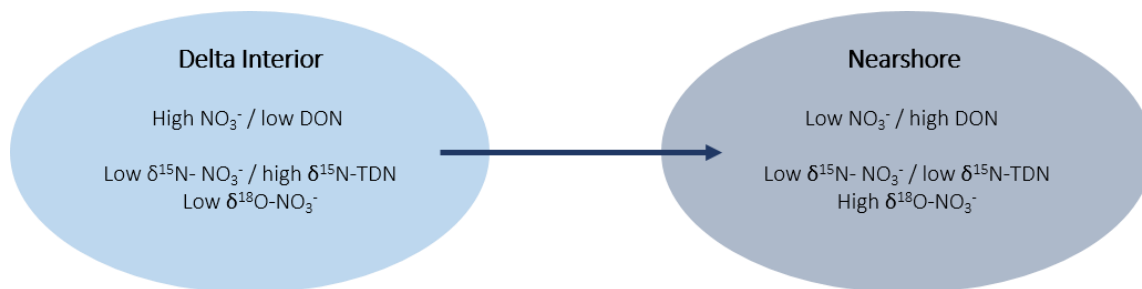


Figure 28: Permafrost thaw signal for organic N species (DON) and inorganic N species (NO_3^-) and corresponding isotope signals grouped for the delta interior and nearshore in relative abundance.

From delta interior to nearshore of the Laptev Sea, measured $\delta^{15}\text{N-NO}_3^-$ showed only slight increase (from ~ 3.3 to ~ 3.4 ‰) and decrease for $\delta^{15}\text{N-TDN}$ (~ 2.5 ‰ to ~ 2 ‰). This indicates a well-mixed winter environment. As discussed earlier in 4.5, isotopic signatures for TDN are roughly assumed to account for DON ($\delta^{15}\text{N-DON} \approx \delta^{15}\text{N-TDN}$). From here forth they are referred to as isotopic signals of DON ($\delta^{15}\text{N-DON}$).

The presence of both DON and NO_3^- in the Lena during winter, is also confirmed by a study done on seasonal nitrogen species trends on large river catchments in the Arctic (Francis, 2019). Here greatest nitrate fluxes for the Lena were found to be during the winter in contrast to other Arctic rivers (e.g. the Kolyma).

CAC19-F has been excluded from most of analysis since it showed much higher temperatures and salinity values when comparing data from both CTDs from the field. When sampling at site CAC19-F, pictures recorded many bubbles in the ice (Figure 29 c), pointing to the presence of gas. Previous studies record subsea permafrost being present in the Laptev Sea (Delisle, 2000; Overduin et al., 2020) as well as the possibility of pathways for migration of gas hydrates in the Lena Delta (Delisle, 2000).

Analysis showed that CAC19-F is an outlier especially for nitrogen isotopic data (Figure 23) and shows elevated or smaller values for DON and nitrate concentration respectively when compared to surrounding samples. Because of the locally warmer temperatures, presumably induced by gas hydrates, activity for utilizing nitrate is higher and it is converted to DON. This would explain the locally different N species. However, one should be careful building a theory based on only one sample point.

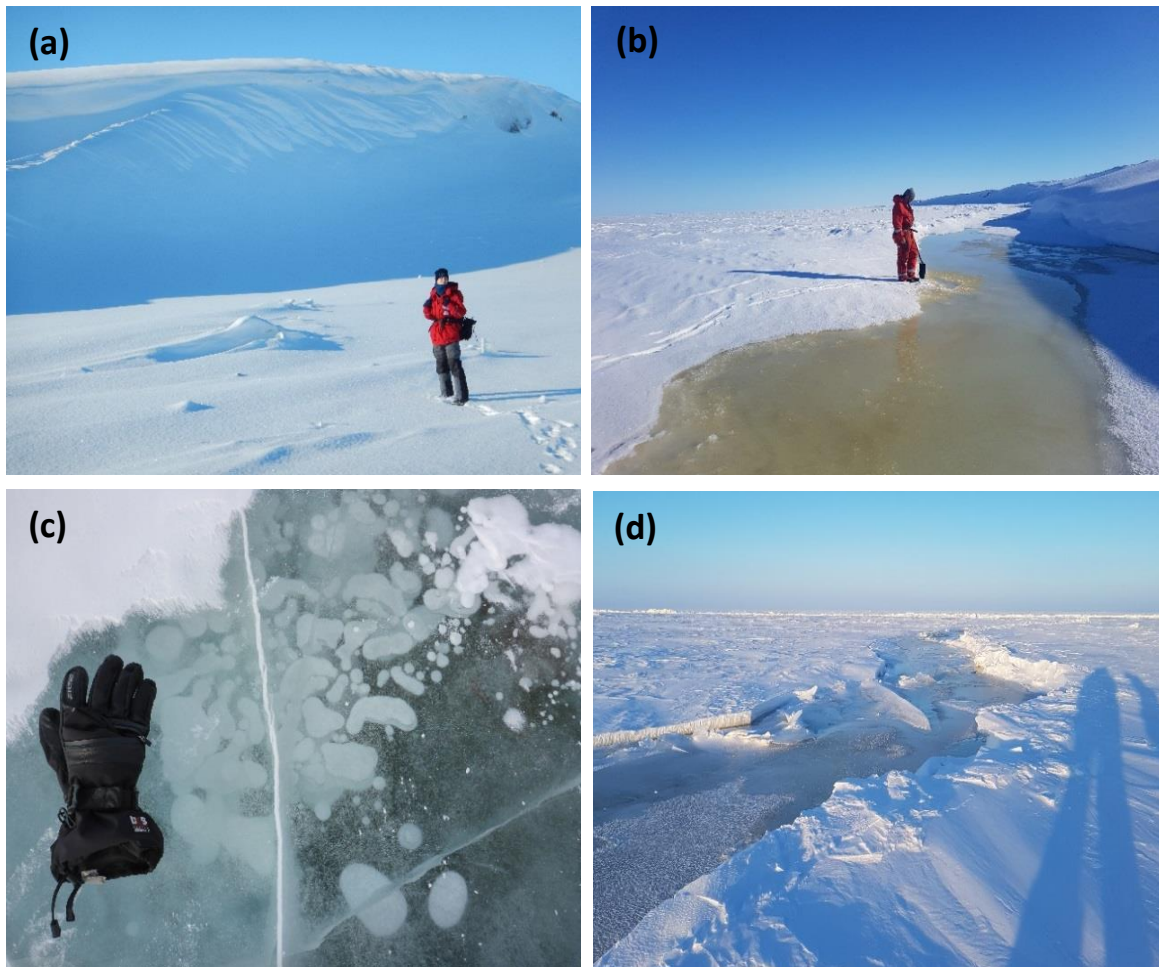


Figure 29: Impressions of the field during the CACOON on Ice field campaign in March/April 2019: **(a)** Sobo-Sise Cliff in Winter (photo: M. Fuchs, 4. April 2019), **(b)** J. Strauss in front of an open water segment just below Sobo-Sise Cliff (photo: J. Palmtag, 5. April 2019), **(c)** bubbles inside the ice at CAC19-F (photo: J. Strauss, 8. April 2019) and **(d)** crack in the sea ice blocking the way with water behind it (photo: J. Palmtag, 5. April 2019).

5.2.2 Nitrogen pathways

Looking at concentration and fluxes is useful to see inputs of nitrogen species in the river water but does not show which biochemical processes occur. Isotopic measurements in this study are used to facilitate and determine nitrogen pathways and shed light on changes in the riverine biogeochemistry.

Nitrogen export Hypothesis

As discussed in 5.1.1, organic material is freshest or least degraded within the active layer and exhibits a high C:N ratio. Harms & Jones (2012) propose that nitrogen export to rivers changes with active layer deepening as a result of permafrost thaw. This process is summarized in Figure 30.

In the active layer, biotic assimilation of nitrate occurs along with denitrification under anaerobic conditions. During winter, frozen ground is likely to emit thin overland or snowpack flow (Juhls et al., 2020). This flow path facilitates the transit of N from organic horizons of permafrost sites to the river. Under intact permafrost conditions/during winter the nitrogen export from the active layer will largely be in the form of DON with a limited nitrate signal (Figure 30 a). The hypothesis further entails that with warming and active layer deepening into mineral horizons that show low C:N ratios, the hydrological flow path also penetrates deeper. In those mineral horizons, adsorption of DON is increased and mineralization and nitrification are dominant processes (Figure 30 b). Therefore nitrogen export to

rivers in thaw-zones during summer would largely be in the form of nitrate with DON being retained Harms & Jones (2012).

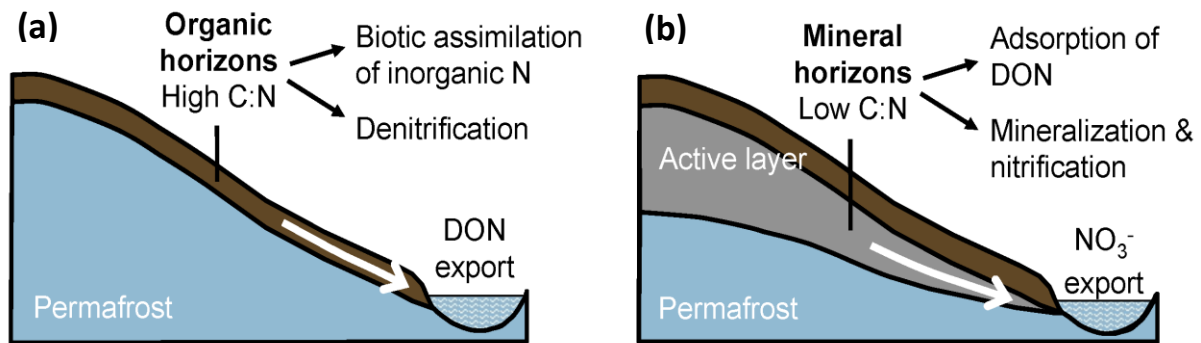


Figure 30: Changing nitrogen export to Arctic Rivers with active layer deepening as a result of permafrost thaw. (A) Intact permafrost condition/winter condition – N export largely in form of DON and (B) permafrost thaw conditions/late summer or autumn signal with degraded permafrost allows interaction with mineral soils and promotes production of inorganic N – N export largely in form of NO₃⁻ with DON retained. Modified from Harms et al. (2013).

This study shows a high DON signal in the nearshore (cluster II) with a low NO₃⁻ signature, which supports the winter scenario (a) in this thesis. Low nitrate in the shelf area/nearshore might be caused by nitrate being more readily removed and used for remineralization rather than DON. Both δ¹⁵N of nitrate are low (~3 ‰) and DON (~2 ‰) representative for a winter environment. With too few data points and lacking spatial and depth distribution, it is hard to speculate how the N species behave further over the shelf.

However, the DON signal in the delta interior (cluster I) was very low with a 6x higher NO₃⁻ signal. Two explanations are possible for this trend. Firstly, there might be a scenario presents resembling Figure 30 b). Although it is attributed rather to summer or a thaw-setting when both river discharge and nutrient load are high. In this case, a high nitrate signal could stem from the central Lena Delta characterized by yedoma deposits where flow paths could reach into active layer adsorbing DON by mineralization or nitrification. However, hydrological flow paths during winter are believed to stem from subsurface flows (groundwater, soil and pore water) (Juhls et al., 2020) and C:N ratios from yedoma deposits are rather high (5.1.2) instead of low. This opposes this theory. Secondly, high nitrate concentration in the delta interior might not necessarily in contrast to the nitrogen export hypothesis for a winter scenario (Figure 30 a). But rather the released DON could be quickly transported to the Laptev Sea, which is supported by isotopic signatures for DON and NO₃⁻ having the same range in the delta interior. Although the second scenario seems more likely, the stable isotopic analysis cannot clearly prove or deny either ones.

For the Lena River winter nitrate concentrations have been reported to be generally high and decrease during the spring freshet (Kattner et al., 1999; Holmes et al., 2012; Le Fouest et al., 2012). Further, previous studies suggested winter DON concentrations do not differ greatly from summer, but slowly decrease along the salinity gradient (Cauwet & Sidorov, 1996; Holmes et al., 2012).

Likely Processing of Nitrogen Species

Large amounts of organic matter and organic nitrogen is released from permafrost soils during thaw and degradation via dissolved organic nitrogen. It undergoes rapid mineralization, firstly to ammonium which is very reactive so is quickly converted into nitrite and nitrate via nitrification (Voigt et al., 2017). Due to kinetic fractionation, the lighter isotopes of nitrogen are preferred for the reactions (Mariotti et al., 1981). However the first part of nitrification, during ammonification (Figure 4), only minimal fractionation takes place (Swart et al., 2008). Therefore most of the fractionation of $\delta^{15}\text{N}$ must be happening when converting available DON to nitrate via nitrification in the delta interior. An overview of nitrogen cycling with fractionation processes is given in Figure 31.

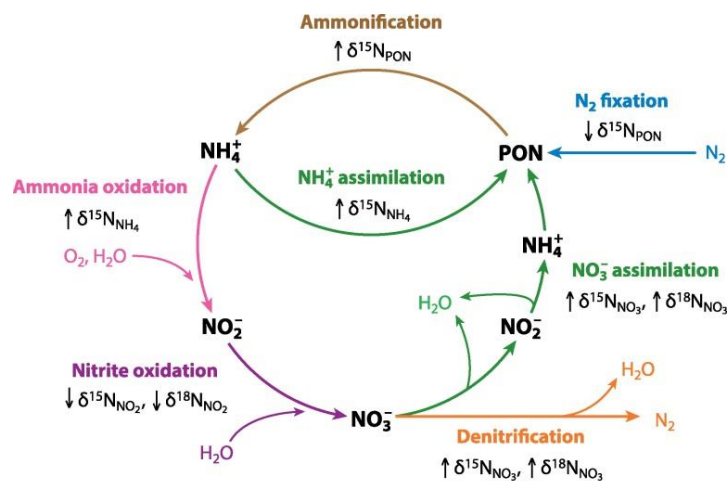


Figure 31: Overview of Nitrogen cycling pathways and fractionation processes in the microbial N-cycle. PON = Particulate organic Nitrogen, not analysed in this study. PON and DON have a close relationship and for simplicity reasons it can be assumed that in this cycle, PON =DON. Adapted from Casciotti (2016).

Denitrifying bacteria can convert readily available nitrate to atmospheric N_2 via denitrification, which produces much stronger kinetic fractionation than nitrification (Swart et al., 2008).

The residual pools of nitrogen and oxygen are enriched in the heavy isotopes equally (Granger et al., 2004) during this nitrate consumption processes of denitrification or assimilation, which converts nitrate back into DON. The fractionation of the two isotopes are “coupled” resulting in a near 1:1 relationship between them (Botrel et al., 2017). In comparison, nitrate producing processes, nitrification and fixation causes decoupled fractionation between the isotopes due to different nitrogen and oxygen sources. Nitrogen comes from ammonium after organic matter remineralisation (with a supply of atmospheric nitrogen if fixation occurs) while oxygen comes from water and dissolved oxygen. Each of these pathways has different fractionation extents. This ultimately leads to a deviation from the 1:1 line (Sigman et al., 2005). Figure 32 shows expected relationships of stable isotopes $\delta^{15}\text{N}$ and $\delta^{18}\text{O}$ of nitrate through dominant nitrogen pathways after (Botrel et al., 2017) next to a plot of samples of this study for Lena samples. The green dashed trend line has a slope of 1.2, suggesting denitrification as dominant processes for nitrate removal.

$\delta^{15}\text{N}-\text{NO}_3^-$ measurements were relatively homogenous with a slight increasing trend towards the nearshore. This means they are river influenced because they show lighter $\delta^{15}\text{N}-\text{NO}_3^-$ values than for marine influence. No significant difference between the samples suggest a well-mixed signal.

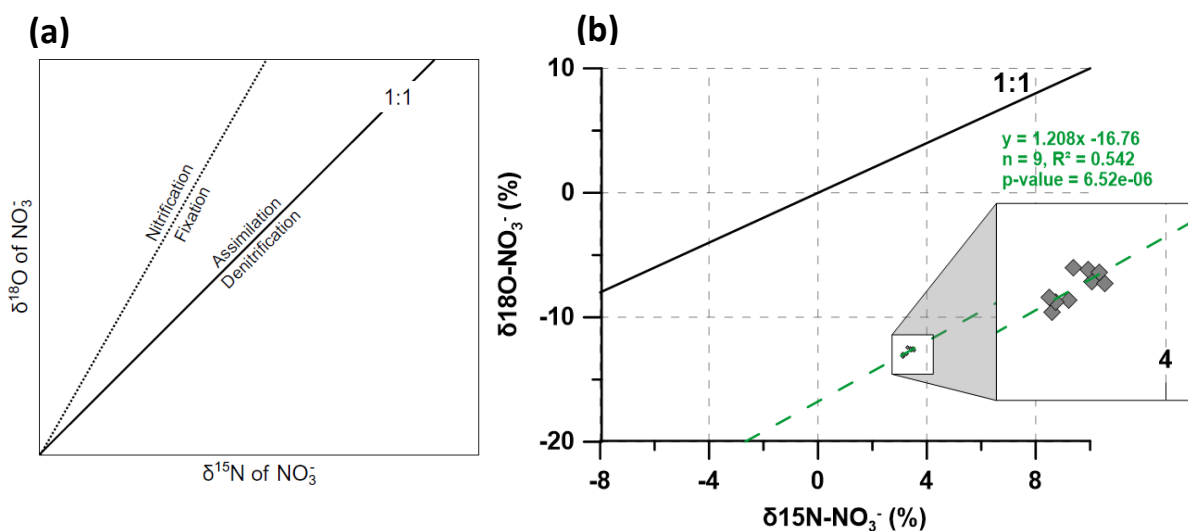


Figure 32: (a) Nitrogen cycling pathways inferred by expected relationships between stable isotopes $\delta^{15}\text{N}$ and $\delta^{18}\text{O}$ of nitrate through dominant nitrogen pathways (Botrel et al., 2017). (b) Correlations of stable isotopes from the Lena river in relation to 1:1 trend (black). Trend line for Lena samples (dashed green line) and data points (grey diamonds) suggesting denitrification. Graph created with Grapher 9.

Therefore, nitrogen processing in the permafrost thaw zone not only involves nitrate removal by heterotrophic remineralisation involving anaerobic processes such as denitrification (Figure 32), but also active release of DON to the river system. This means, there is an exchange between nitrogen pools still in the permafrost. Thaw released DON shows light isotopic signatures in the river water indicating fresh DON. A change of signal from lighter to heavier ($\delta^{15}\text{N-TDN}$) and vice versa ($\delta^{15}\text{N}-\text{NO}_3^-$) occurs but does not prove significant when moving from the delta into the nearshore zone (Table 6). A more pronounced change would indicate uptake and assimilation of nitrate rather than DON even during winter. It is important to note that dilution processes from other sources of nitrate could influence the signal in the water column, although in a winter scenario this is not very likely.

While inorganic nutrients are directly available for uptake by primary producers, organic nutrients must typically be remineralized to their inorganic forms before they can be assimilated by autotrophs (Tank et al., 2012). Nitrate as an inorganic compound is more bioavailable for consumption or assimilation by primary consumers than DON, which is reflected in their respective concentrations. These findings are important to better understand the biogeochemistry of the Lena Delta and shelf area.

5.2.3 Implications for the ecosystem

A range of studies have previously estimated the flux of C and N from the Lena River. Wild et al. (2019) estimated an OC flux of 0.9 Tg C/yr coming from permafrost and peat deposits for the Lena River. In particular Sobo Sise cliff as an important erosional feature has an average loss of 5.2×10^6 kg C (SOC and DOC) and 0.4×10^6 kg N per year (2015-2018) (Fuchs et al., in review). This study ties in with those findings by confirming the high quality of organic matter stored in a yedoma cliff with very high erosion rates. All of this is evidence of the magnitude of biogeochemical fluxes eroding from permafrost features in the Lena Delta, carried by the river and finally flowing into the Laptev Sea shelf.

Thibodeau et al. (2017) showed, the Lena River current discharging into the Laptev Sea mostly affects the surface water, while the bottom water is influenced by the Atlantic-derived water flowing along the continental slope and branching onto the shelf. Consequently most ecosystem implication like an increase in annual primary production would take place in the upper ocean and the photic zone first

and then affect other parts of the shelf by physical, chemical and biological mechanisms of redistribution. Secondary advective processes by currents can be responsible for alongshore drift of suspended organic matter once discharges into the shelf area. There is also evidence, that a large amount of permafrost C might become re-buried in marine sediments of the Laptev and East Siberian Sea shelf (Bröder et al., 2019; Vonk & Gustafsson, 2013).

Assimilation of organic matter and changes to vertebrate and invertebrate food webs of the nearshore zone of Arctic Ocean have been reported in several studies (Casper et al., 2015; Dunton et al., 2006). Especially the availability of N in the coastal Arctic is a limiting factor for primary productivity. A large portion of N is released from rivers by the spring freshet and completely consumed during the following summer (Thibodeau et al., 2017). Rapid uptake of dissolved inorganic nitrogen (DIN) coupled with relatively high rates of DON regeneration in N-limited nearshore regions could potentially lead to high rates of localized riverine-supported photosynthesis (Tank et al., 2012). However, others also report the mean riverine NO_3^- contribution to ocean primary production to be generally low in the Arctic with about 5% in the Laptev Sea (Le Fouest et al., 2013). Because riverine DON is remineralized slowly, riverine N is available for uptake well into the open ocean (Tank et al., 2012).

Factors limiting primary productivity can be different in the nearshore zone compared to the Arctic Ocean. Measurements from the Arctic Ocean show N to be the primary limiting nutrient further offshore (Dittmar et al., 2001; Simpson et al., 2008). For shelf regions in the Arctic there have been different observations. The inner Mackenzie Shelf of the Beaufort Sea appears P limited, whereas near-complete summertime inorganic N consumption occurs as salinities rise (Simpson et al., 2008). Throughout the Eurasian Shelf region, rapid summertime depletion of NO_3^- across the full estuarine gradient in the Laptev Sea indicates N limitation (Kattner et al., 1999). Following Tank et al. (2012), riverine nutrients do not support a large proportion of primary production in the Arctic Ocean. But rather it is in nearshore regions that riverine nutrients have the greatest influence on production. Here Tank et al. (2012) estimated in a modelling approach that nearshore primary production supported by terrigenous N may range as high as 5.2 mol C m/yr, whereas the total nearshore production is at 8–12 mol C m/yr (Pabi et al., 2008). Therefore increased N supply in this region specifically would enhance nearshore primary productivity, but this might not necessarily be true for all Arctic coastal waters.

As a particular bioavailable component DOC can potentially play a big role for microbial use. For example Vonk et al. (2013) showed that yedoma ice wedge meltwater can increase the degradation of organic matter due to co-metabolizing effects.

Another change in biochemical properties can be increased ocean acidification driven by the degradation of terrestrial organic matter and discharge of Arctic river water rather than anthropogenic carbon dioxide uptake from the atmosphere (Semiletov et al., 2016) on East Siberian Arctic Shelf waters. Shelf water turns acidic due to higher CO_2 concentrations from river water input. The study by Semiletov et al. (2016) estimated 57% of the terrestrial organic C in the East Siberian Shelf originates from old Pleistocene age permafrost C, such as the deposits in Sobo Sise Cliff.

5.2.4 Further studies

To evaluate the source of river water samples, additional data for water stable isotopes δD and $\delta^{18}O$ was measured and provided by Paul Mann from Northumbria University. Full data can be viewed in Appendix (8.6).

The distribution of water isotopes varies spatially and temporally in the atmosphere, in precipitation and consequently in the hydro- and cryosphere (Jouzel, 2003). Lighter water isotopes evaporate more easily, whereas heavier isotopes remain behind. Fractioning processes occur, due to the different physical properties of the molecules and the resulting different impact of evaporation and precipitation on lighter and heavier isotopes (Jouzel, 2003). Because of the modification by fractionation processes, waters in a particular environment will have a characteristic isotope signature. To determine excess deuterium, the following equation was used (Dansgaard, 1964): $\delta 2H = 8 * \delta 18O + 10$.

δD and $\delta^{18}O$ stable isotopes are plotted in relation to the Global Meteoric Water line (GMWL: $y=8x+10$) (Craig, 1961). The GMWL correlates with the mean hydrogen and oxygen isotope composition of fresh terrestrial water on a global scale. It is a global average of many local meteoric water lines, each determined by local climatic factors, e.g. the origin of the vapour masses, secondary evaporation during rainfall and the seasonality of precipitation (Clark and Fritz, 1997). These factors affect the deuterium excess (Dansgaard, 1964) and thus the slope in the isotope diagram (Figure 33).

Values for δD ranged from -158.58 to -159.79 ‰ and $\delta^{18}O$ from -21.05 to -21.31 ‰. Values for d-excess were between 11.47 and 9.51. Overall, samples show enrichment in $\delta^{18}O$ which means less recent freshwater. This expectantly fits well, since I was observing a nearshore moving transect, with western values showing poorer isotopic signatures and increasing eastwards. Freshwater input decreases as expected when investigating a river mouth.

$\delta^{18}O$ and δD values compare well to other studies carried out in the Lena Delta (Bonne et al., 2020; Juhls et al., 2020) for the winter season. D-excess values have been determined as highest in the winter season (10.90 ‰, Juhls et al., 2020) which correlates well.

Additionally two separate trends were visible. One shows groundwater input moving to the nearshore (orange, and the other one showing possible input from river ice melt water (dark blue, values for $\delta^{18}O$ are slightly higher). Groundwater in that sense has been called supra-permafrost (Lebedeva, 2019) or subsurface water (Juhls et al., 2020). Both slopes are intercepting the GMWL in Figure 33. The slope for groundwater influenced samples is 2.53 in comparison to ice melt influenced samples with a slope of -2.8. Both significantly differ from the GMWL with a slope of 8. Previous studies suggest the Lena River being mainly fed by groundwater in during winter (Cauwet & Sidorov, 1996).

In a recent paper by Juhls et al. (2020) investigated samples from both Lena river water and Lena river ice. They found that the ice core samples compared to the river water had higher mean $\delta^{18}O$ and δD values, but with a shift to lower δD for similar $\delta^{18}O$. We can see that trend reflected in our data: ice melt influenced samples show higher $\delta^{18}O$ values. It is striking, that $\delta^{18}O$ is highest in furthest samples moving to the nearshore (CAC19-23, CAC19-03, CAC19-04), which are in near vicinity of the ice cracks. Photos from the expedition proof that behind ice cracks small melt water ponds formed, which could cause melting and would explain the ice melt signal observed. Additionally, CAC19-F is in line with the fit line of ice melt water input in Figure 33 b) even though the sampling point lies further west inside the delta.

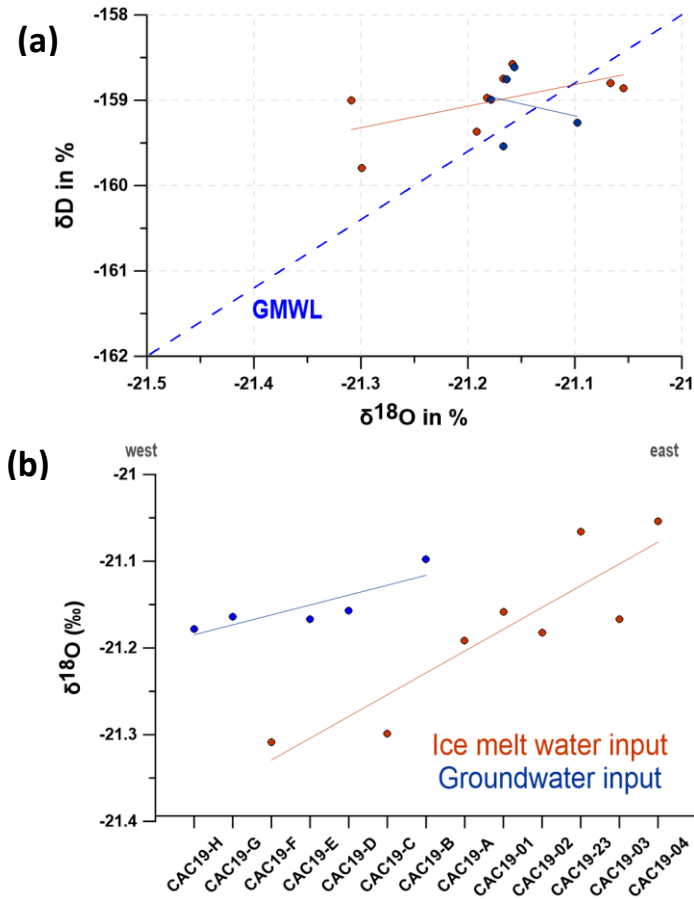


Figure 33: (a) δD over $\delta^{18}O$ diagram of river water samples. Orange data points represent influence of ice melt water, dark blue stands for groundwater influence. GMWL – Global Meteoric Water Line (b) $\delta^{18}O$ isotopic signatures over transect showing two separate trends seawards. Graph was created in Grapher 9.

However, DON and NO_3^- concentrations follow the trend expressed, when plotted following the grouping from stable isotope data (Figure 34). Higher concentrations are observed for DON and lower for NO_3^- . CAC19-F again stands out elevated or lower than surrounding samples, for DON and NO_3^- respectively. However, this confirms the theory described in 5.2.1.

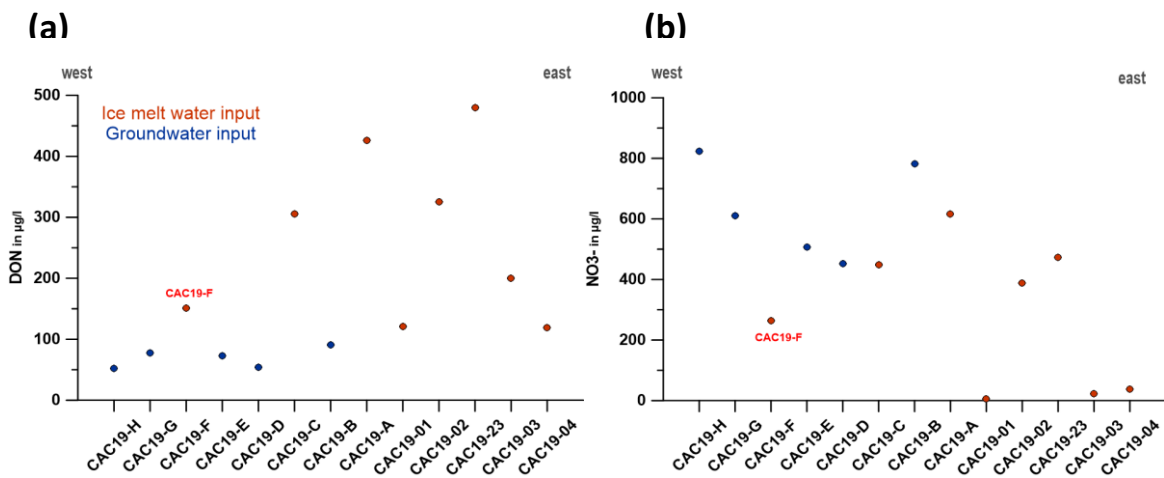


Figure 34: (a) DON in $\mu g/l$ and (b) Nitrate in $\mu g/l$ over transect moving seawards. Each of them showing two separate trends: orange data points = influence of ice melt water, dark blue = groundwater influence. Graph created in Grapher 9.

6 Conclusion

This study represents organic matter characteristics from the yedoma deposit from Sobo-Sise Cliff in the central Lena Delta as well as an investigation of dissolved organic matter endmember dynamics. Sedimentological and biogeochemical analysis showed Sobo-Sise Cliff holds exceptionally high TOC values (mean 5.12 wt %) in comparison to nearby sites. Biomarker distribution proved mainly high quality OM has been freeze-locked since deposition since the late Pleistocene.

The dominant water flow during winter is attributed mainly to supra permafrost flow with local influence from river ice melt. Winter nitrogen dynamics between Lena Delta interior and nearshore Laptev Sea entail both NO_3^- and TDN, made up primarily of DON. DON is the dominant nitrogen species in winter actively released from permafrost with nitrate removal in the permafrost before reaching the river. Low nitrogen stable isotope signatures indicate a well-mixed winter environment. Slight increase and decrease for NO_3^- and DON respectively do not prove statistically significant. It would indicate uptake and assimilation of nitrate rather than DON in the nearshore and point out low nitrogen turnover even during winter. Nitrate as a more bioavailable inorganic compound is favoured for consumption or assimilation by primary consumers rather than DON.

The Denitrifier technique led to isotopic analysis identifying nitrogen pathways in the winter during river transit. Sobo-Sise Cliff as an example of the most readily erodible permafrost features of the Lena Delta holds high quality OM which poses high vulnerability and possibility to alter the biogeochemistry and ecosystem of the Laptev Sea Shelf surface waters.

This data set represents an investigation of winter C and N dynamics at the land to sea interface and can be used as a reference to facilitate further investigation of both lipid biomarker studies of yedoma sites in Northern Siberia and nitrogen species and their processing in the water column.

7 References

- Andreev, A., Schirrmeister, L., Siegert, C., Bobrov, A. A., Demske, D., Seiffert, M., & Hubberten, H.-W. (2002). Paleoenvironmental changes in Northeastern Siberia during the Late Quaternary—evidence from pollen records of the Bykovsky Peninsula. *Polarforschung*, *70*, 13–25.
- Bischoff, J., Mangelsdorf, K., Gattinger, A., Schloter, M., Kurchatova, A. N., Herzsuh, U., & Wagner, D. (2013). Response of methanogenic archaea to Late Pleistocene and Holocene climate changes in the Siberian Arctic. *Global Biogeochemical Cycles*, *27*(2), 305–317.
- Blaauw, M., & Christen, J. A. (2011). Flexible paleoclimate age-depth models using an autoregressive gamma process. *Bayesian Analysis*, *6*(3), 457–474.
- Boike, J., Kattenstroth, B., Abramova, K., Bornemann, N., Chetverova, A., Fedorova, I., Fröb, K., Grigoriev, M., Grüber, M., & Kutzbach, L. (2012). Baseline characteristics of climate, permafrost, and land cover from a new permafrost observatory in the Lena River Delta, Siberia (1998- 2011). *Biogeosciences Discussions*, *9*(10), 13627. <https://doi.org/10.5194/bg-10-2105-2013>
- Bonne, J.-L., Meyer, H., Behrens, M., Boike, J., Kipfstuhl, S., Rabe, B., Schmidt, T., Schöncke, L., Steen-Larsen, H. C., & Werner, M. (2020). Moisture origin as a driver of temporal variabilities of the water vapour isotopic composition in the Lena River Delta, Siberia. *Atmos. Chem. Phys. Discuss. Rev. Doi*, *10*.
- Botrel, M., Bristow, L. A., Altabet, M. A., Gregory-Eaves, I., & Maranger, R. (2017). Assimilation and nitrification in pelagic waters: Insights using dual nitrate stable isotopes ($\delta^{15}\text{N}$, $\delta^{18}\text{O}$) in a shallow lake. *Biogeochemistry*, *135*(3), 221–237.
- Brassell, S. C., Eglinton, G., Maxwell, J. R., & Philp, R. P. (1978). Natural background of alkanes in the aquatic environment. In *Aquatic pollutants* (pp. 69–86). Elsevier.
- Bray, E. E., & Evans, E. D. (1961). Distribution of n-paraffins as a clue to recognition of source beds. *Geochimica et Cosmochimica Acta*, *22*(1), 2–15. [https://doi.org/10.1016/0016-7037\(61\)90069-2](https://doi.org/10.1016/0016-7037(61)90069-2)
- Bröder, L., Andersson, A., Tesi, T., Semiletov, I., & Gustafsson, Ö. (2019). Quantifying degradative loss of terrigenous organic carbon in surface sediments across the Laptev and East Siberian Sea. *Global Biogeochemical Cycles*, *33*(1), 85–99.
- Brown, J., Ferrians Jr, O. J., Heginbottom, J. A., & Melnikov, E. S. (1997). *Circum-Arctic map of permafrost and ground-ice conditions*. US Geological Survey Reston, VA.
- Casciotti, K. L., Sigman, D. M., Hastings, M. G., Böhlke, J. K., & Hilkert, A. (2002). Measurement of the oxygen isotopic composition of nitrate in seawater and freshwater using the denitrifier method. *Analytical Chemistry*, *74*(19), 4905–4912. <https://doi.org/10.1021/ac020113w>
- Casciotti, Karen L. (2016). Nitrogen and oxygen isotopic studies of the marine nitrogen cycle. *Annual Review of Marine Science*, *8*, 379–407.
- Casciotti, Karen L., McIlvin, M., & Buchwald, C. (2010). Oxygen isotopic exchange and fractionation during bacterial ammonia oxidation. *Limnology and Oceanography*, *55*(2), 753–762.
- Casper, A. F., Rautio, M., Martineau, C., & Vincent, W. F. (2015). Variation and assimilation of Arctic riverine seston in the pelagic food web of the Mackenzie River Delta and Beaufort Sea Transition Zone. *Estuaries and Coasts*, *38*(5), 1656–1663.
- Cauwet, G., & Sidorov, I. (1996). The biogeochemistry of Lena River: Organic carbon and nutrients distribution. *Marine Chemistry*, *53*(3–4), 211–227.
- Christopherson, R. W. (1997). *Glacial and Periglacial Processes and Landforms, in Geosystems: An introduction to physical geography*.

- Craig, H. (1961). Standard for reporting concentrations of deuterium and oxygen-18 in natural waters. *Science*, 133(3467), 1833–1834.
- Cranwell, P. A., Eglinton, G., & Robinson, N. (1987). Lipids of aquatic organisms as potential contributors to lacustrine sediments—II. *Organic Geochemistry*, 11(6), 513–527.
- Dansgaard, W. (1964). Stable isotopes in precipitation. *Tellus*, 16(4), 436–468.
- Delisle, G. (2000). Temporal variability of subsea permafrost and gas hydrate occurrences as function of climate change in the Laptev Sea, Siberia. *Polarforschung*, 68, 221–225.
- Dittmar, T., Fitznar, H. P., & Kattner, G. (2001). Origin and biogeochemical cycling of organic nitrogen in the eastern Arctic Ocean as evident from D- and L-amino acids. *Geochimica et Cosmochimica Acta*, 65(22), 4103–4114.
- Dunton, K. H., Weingartner, T., & Carmack, E. C. (2006). The nearshore western Beaufort Sea ecosystem: Circulation and importance of terrestrial carbon in arctic coastal food webs. *Progress in Oceanography*, 71(2–4), 362–378.
- Dutta, K., Schuur, E. A. G., Neff, J. C., & Zimov, S. A. (2006). Potential carbon release from permafrost soils of Northeastern Siberia. *Global Change Biology*, 12(12), 2336–2351.
- Eglinton, G., & Hamilton, R. J. (1967). Leaf epicuticular waxes. *Science*, 156(3780), 1322–1335.
- Everdingen, R. van. (1976). Geocryological terminology. *Canadian Journal of Earth Sciences*, 13(6), 862–867.
- Fedorova, I., Chetverova, A., Bolshiyarov, D., Makarov, A., Boike, J., Heim, B., Morgenstern, A., Overduin, P. P., Wegner, C., & Kashina, V. (2015). Lena Delta hydrology and geochemistry: Long-term hydrological data and recent field observations. *Biogeosciences*, 12(2), 345–363. <https://doi.org/10.5194/bg-12-345-2015>
- Francis, A. (2019). *Stable Isotope Tracing of Dissolved Nitrogen from Permafrost Degradation in Arctic Rivers*. [Master Thesis]. The University of Edinburgh.
- French, H. M. (2017). *The Periglacial Environment*. John Wiley & Sons.
- Frey, K. E., McClelland, J. W., Holmes, R. M., & Smith, L. C. (2007). Impacts of climate warming and permafrost thaw on the riverine transport of nitrogen and phosphorus to the Kara Sea. *Journal of Geophysical Research: Biogeosciences*, 112(G4). <https://doi.org/10.1029/2006JG000369>
- Fuchs, M., Grosse, G., Strauss, J., Günther, F., Grigoriev, M., Maximov, G. M., & Hugelius, G. (2019). *Carbon and nitrogen pools in thermokarst-affected permafrost landscapes in Arctic Siberia*.
- Fuchs, M., Nitze, I., Strauss, J., & Wetterich, S. (in review). Rapid fluvio-thermal erosion of a yedoma permafrost cliff in the Lena River Delta. *Frontiers in Environmental Science*.
- Glombitza, C., Mangelsdorf, K., & Horsfield, B. (2009). Maturation related changes in the distribution of ester bound fatty acids and alcohols in a coal series from the New Zealand Coal Band covering diagenetic to catagenetic coalification levels. *Organic Geochemistry*, 40(10), 1063–1073. <https://doi.org/10.1016/j.orggeochem.2009.07.008>
- Gordeev, V. V., & Shevchenko, V. P. (1995). Chemical composition of suspended sediments in the Lena river and its mixing zone. *Berichte Zur Polar-Und Meeresforschung*, 176, 154–169.
- Granger, J., Sigman, D. M., Needoba, J. A., & Harrison, P. J. (2004). Coupled nitrogen and oxygen isotope fractionation of nitrate during assimilation by cultures of marine phytoplankton. *Limnology and Oceanography*, 49(5), 1763–1773.
- Grigoriev, M. N. (1993). *Criomorphogenesis in the Lena Delta*. Permafrost Institute Press, 176pp.
- Grosse, G., Romanovsky, V., Jorgenson, T., Anthony, K. W., Brown, J., & Overduin, P. P. (2011). Vulnerability and feedbacks of permafrost to climate change. *Eos, Transactions American Geophysical Union*, 92(9), 73–74.

- Gruber, N. (2008). The marine nitrogen cycle: Overview and challenges. *Nitrogen in the Marine Environment*, 2, 1–50.
- Günther, F., Overduin, P. P., Sandakov, A. V., Grosse, G., & Grigoriev, M. N. (2013). Short-and long-term thermo-erosion of ice-rich permafrost coasts in the Laptev Sea region. *Biogeosciences*, 10, 4297–4318.
- Günther, F., Overduin, P. P., Yakshina, I. A., Opel, T., Baranskaya, A. V., & Grigoriev, M. N. (2015). Observing Muostakh disappear: Permafrost thaw subsidence and erosion of a ground-ice-rich island in response to arctic summer warming and sea ice reduction. *The Cryosphere*, 9(1), 151–178.
- Harms, T. K., Abbott, B., Balsler, A., Jones, J., Olsson, A., & Rinehart, A. (2013). *Permafrost thaw and a changing nitrogen cycle*. 64.
- Harms, T. K., & Jones Jr, J. B. (2012). Thaw depth determines reaction and transport of inorganic nitrogen in valley bottom permafrost soils: Nitrogen cycling in permafrost soils. *Global Change Biology*, 18(9), 2958–2968.
- Höfle, S., Rethemeyer, J., Mueller, C. W., & John, S. (2013). Organic matter composition and stabilization in a polygonal tundra soil of the Lena Delta. *Biogeosciences*, 10(5), 3145.
- Holmes, R. M., McClelland, J. W., Peterson, B. J., Tank, S. E., Bulygina, E., Eglinton, T. I., Gordeev, V. V., Gurtovaya, T. Y., Raymond, P. A., & Repeta, D. J. (2012). Seasonal and annual fluxes of nutrients and organic matter from large rivers to the Arctic Ocean and surrounding seas. *Estuaries and Coasts*, 35(2), 369–382.
- Hugelius, G., Strauss, J., Zubrzycki, S., Harden, J. W., Schuur, E. A. G., Ping, C.-L., Schirmer, L., Grosse, G., Michaelson, G. J., & Koven, C. D. (2014). Estimated stocks of circumpolar permafrost carbon with quantified uncertainty ranges and identified data gaps. *Biogeosciences (Online)*, 11(23).
- Jongejans, L. L., Strauss, J., Lenz, J., Peterse, F., Mangelsdorf, K., Fuchs, M., & Grosse, G. (2018). Organic matter characteristics in yedoma and thermokarst deposits on Baldwin Peninsula, west Alaska. *Biogeosciences*, 15(20), 6033–6048.
- Jouzel, J. (2003). Water stable isotopes: Atmospheric composition and applications in polar ice core studies. *TrGeo*, 4, 347.
- Juggins, S. (2019). *rioja: Analysis of Quaternary Science Data (0.9-21)* [Computer software]. <https://CRAN.R-project.org/package=rioja>
- Juhls, B., Stedmon, C. A., Morgenstern, A., Meyer, H., Hölemann, J., Heim, B., Povazhnyi, V., & Overduin, P. P. (2020). Identifying Drivers of Seasonality in Lena River Biogeochemistry and Dissolved Organic Matter Fluxes. *Frontiers in Environmental Science*, 8, 53.
- Kanevskiy, M., Shur, Y., Fortier, D., Jorgenson, M. T., & Stephani, E. (2011). Cryostratigraphy of late Pleistocene syngenetic permafrost (yedoma) in northern Alaska, Ikillik River exposure. *Quaternary Research*, 75(3), 584–596. <https://doi.org/10.1016/j.yqres.2010.12.003>
- Kattner, G., Lobbes, J. M., Fitznar, H. P., Engbrodt, R., Nöthig, E.-M., & Lara, R. J. (1999). Tracing dissolved organic substances and nutrients from the Lena River through Laptev Sea (Arctic). *Marine Chemistry*, 65(1–2), 25–39.
- Killops, S. D., & Killops, V. J. (2013). *Introduction to organic geochemistry*. John Wiley & Sons.
- Kim, S., Stanford, L. A., Rodgers, R. P., Marshall, A. G., Walters, C. C., Qian, K., Wenger, L. M., & Mankiewicz, P. (2005). Microbial alteration of the acidic and neutral polar NSO compounds revealed by Fourier transform ion cyclotron resonance mass spectrometry. *Organic Geochemistry*, 36(8), 1117–1134. <https://doi.org/10.1016/j.orggeochem.2005.03.010>

- Kitover, D. C., Van Balen, R. T., Vandenberghe, J., Roche, D. M., & Renssen, H. (2016). LGM permafrost thickness and extent in the Northern Hemisphere derived from the Earth System Model iLOVECLIM. *Permafrost and Periglacial Processes*, 27(1), 31–42.
- Lachenbruch, A. H. (1963). Contraction theory of ice-wedge polygons: A qualitative discussion. *Permafrost International Conference: Proceedings*, 11–15.
- Le Fouest, V., Babin, M., & Tremblay, J.-É. (2012). The fate of riverine nutrients on Arctic shelves. *Biogeosciences Discussions*, 9(10). <https://doi.org/10.5194/bgd-9-13397-2012>
- Le Fouest, V., Babin, M., & Tremblay, J.-É. (2013). *The fate of riverine nutrients on Arctic shelves*.
- Lebedeva, L. (2019). Tracing surface and ground water with stable isotopes in a small permafrost research catchment. *E3S Web of Conferences*, 98, 12011.
- Lehtonen, K., & Ketola, M. (1993). Solvent-extractable lipids of Sphagnum, Carex, Bryales and Carex-Bryales peats: Content and compositional features vs peat humification. *Organic Geochemistry*, 20(3), 363–380. [https://doi.org/10.1016/0146-6380\(93\)90126-V](https://doi.org/10.1016/0146-6380(93)90126-V)
- Mackay, J. R. (1990). Some observations on the growth and deformation of epigenetic, syngenetic and anti-syngenetic ice wedges. *Permafrost and Periglacial Processes*, 1(1), 15–29.
- Mann, P. J., Eglinton, T. I., McIntyre, C. P., Zimov, N., Davydova, A., Vonk, J. E., Holmes, R. M., & Spencer, R. G. (2015). Utilization of ancient permafrost carbon in headwaters of Arctic fluvial networks. *Nature Communications*, 6(1), 1–7.
- Mann, P. J., Sobczak, W. V., LaRue, M. M., Bulygina, E., Davydova, A., Vonk, J. E., Schade, J., Davydov, S., Zimov, N., & Holmes, R. M. (2014). Evidence for key enzymatic controls on metabolism of Arctic river organic matter. *Global Change Biology*, 20(4), 1089–1100.
- Mariotti, A., Germon, J. C., Hubert, P., Kaiser, P., Letolle, R., Tardieux, A., & Tardieux, P. (1981). Experimental determination of nitrogen kinetic isotope fractionation: Some principles; illustration for the denitrification and nitrification processes. *Plant and Soil*, 62(3), 413–430.
- Marzi, R., Torkelson, B. E., & Olson, R. K. (1993). A revised carbon preference index. *Organic Geochemistry*, 20(8), 1303–1306. [https://doi.org/10.1016/0146-6380\(93\)90016-5](https://doi.org/10.1016/0146-6380(93)90016-5)
- McCrackin, M. L., Harrison, J. A., & Compton, J. E. (2014). Factors influencing export of dissolved inorganic nitrogen by major rivers: A new, seasonal, spatially explicit, global model. *Global Biogeochemical Cycles*, 28(3), 269–285. <https://doi.org/10.1002/2013GB004723>
- McIlvin, M. R., & Casciotti, K. L. (2011). Technical updates to the bacterial method for nitrate isotopic analyses. *Analytical Chemistry*, 83(5), 1850–1856. <https://doi.org/10.1021/ac1028984>
- Meyers, P. A. (2003). Applications of organic geochemistry to paleolimnological reconstructions: A summary of examples from the Laurentian Great Lakes. *Organic Geochemistry*, 34(2), 261–289. [https://doi.org/10.1016/S0146-6380\(02\)00168-7](https://doi.org/10.1016/S0146-6380(02)00168-7)
- Morgenstern, A., Grosse, G., Günther, F., Fedorova, I., & Schirrmeister, L. (2011). Spatial analyses of thermokarst lakes and basins in Yedoma landscapes of the Lena Delta. *The Cryosphere Discussions*, 5, 1495–1545.
- Murton, J. B., Goslar, T., Edwards, M. E., Bateman, M. D., Danilov, P. P., Savvinov, G. N., Gubin, S. V., Ghaleb, B., Haile, J., Kanevskiy, M., Lozhkin, A. V., Lupachev, A. V., Murton, D. K., Shur, Y., Tikhonov, A., Vasil'chuk, A. C., Vasil'chuk, Y. K., & Wolfe, S. A. (2015). Palaeoenvironmental Interpretation of Yedoma Silt (Ice Complex) Deposition as Cold-Climate Loess, Duvanny Yar, Northeast Siberia. *Permafrost and Periglacial Processes*, 26(3), 208–288. <https://doi.org/10.1002/ppp.1843>
- Nitze, I., & Grosse, G. (2016). Detection of landscape dynamics in the Arctic Lena Delta with temporally dense Landsat time-series stacks. *Remote Sensing of Environment*, 181, 27–41. <https://doi.org/10.1016/j.rse.2016.03.038>

- Olefeldt, D., Goswami, S., Grosse, G., Hayes, D., Hugelius, G., Kuhry, P., McGuire, A. D., Romanovsky, V. E., Sannel, A. B. K., & Schuur, E. A. G. (2016). Circumpolar distribution and carbon storage of thermokarst landscapes. *Nature Communications*, 7(1), 1–11.
- Overduin, P. P., Schneider von Deimling, T., Miesner, F., Grigoriev, M. N., Ruppel, C. D., Vasiliev, A. A., Lantuit, H., Juhls, B., Westermann, S., & Laboor, S. (2020). *Submarine Permafrost Map (SuPerMap), modeled with CryoGrid 2, Circum-Arctic* [Miscellaneous]. EPIC3. <https://doi.org/10.1594/PANGAEA.910540>
- Pabi, S., van Dijken, G. L., & Arrigo, K. R. (2008). Primary production in the Arctic Ocean, 1998–2006. *Journal of Geophysical Research: Oceans*, 113(C8).
- Pachauri, R. K., Allen, M. R., Barros, V. R., Broome, J., Cramer, W., Christ, R., Church, J. A., Clarke, L., Dahe, Q., & Dasgupta, P. (2014). *Climate change 2014: Synthesis report. Contribution of Working Groups I, II and III to the fifth assessment report of the Intergovernmental Panel on Climate Change*. Ipcc.
- Peel, M. C., Finlayson, B. L., & McMahon, T. A. (2007). *Updated world map of the Köppen-Geiger climate classification*. <https://doi.org/10.5194/hess-11-1633-2007>
- Peters, K. E., Walters, C. C., & Moldowan, J. M. (2007). *The Biomarker Guide: Volume 1, Biomarkers and Isotopes in the Environment and Human History*. Cambridge University Press.
- Poynter, J. (1989). Molecular stratigraphy: The recognition of palaeoclimatic signals in organic geochemical data. *PhD, School of Chemistry, University of Bristol, Bristol*.
- Poynter, J., & Eglinton, G. (1990). 14. Molecular composition of three sediments from hole 717c: The Bengal fan. *Proceedings of the Ocean Drilling Program: Scientific Results*, 116, 155–161.
- Radke, M., Willsch, H., & Welte, D. H. (1980). Preparative hydrocarbon group type determination by automated medium pressure liquid chromatography. *Analytical Chemistry*, 52(3), 406–411.
- Reimer, P. J., Bard, E., Bayliss, A., Beck, J. W., Blackwell, P. G., Ramsey, C. B., Buck, C. E., Cheng, H., Edwards, R. L., & Friedrich, M. (2013). IntCal13 and Marine13 radiocarbon age calibration curves 0–50,000 years cal BP. *Radiocarbon*, 55(4), 1869–1887.
- Rielley, G., Collier, R. J., Jones, D. M., & Eglinton, G. (1991). The biogeochemistry of Ellesmere Lake, UK—I: Source correlation of leaf wax inputs to the sedimentary lipid record. *Organic Geochemistry*, 17(6), 901–912.
- Routh, J., Hugelius, G., Kuhry, P., Filley, T., Tillman, P. K., Becher, M., & Crill, P. (2014). Multi-proxy study of soil organic matter dynamics in permafrost peat deposits reveal vulnerability to climate change in the European Russian Arctic. *Chemical Geology*, 368, 104–117.
- Schäfer, I. K., Lanny, V., Franke, J., Eglinton, T. I., Zech, M., Vysloužilová, B., & Zech, R. (2016). *Leaf waxes in litter and topsoils along a European transect*. 14. <https://doi.org/10.5194/soil-2-551-2016>
- Schirrmeister, L. (2012). Late Glacial to Holocene landscape dynamics of Arctic coastal lowlands in NE Siberia. *Quaternary International*, 279, 434. <https://doi.org/10.1016/j.quaint.2012.08.1413>
- Schirrmeister, L., Dietze, E., Matthes, H., Grosse, G., Strauss, J., Laboor, S., Ulrich, M., Kienast, F., & Wetterich, S. (2020). The genesis of Yedoma Ice Complex permafrost–grain-size endmember modeling analysis from Siberia and Alaska. *E&G Quaternary Sci. J.*, 69, 33–53.
- Schirrmeister, L., Froese, D., Tumskey, V., Grosse, G., & Wetterich, S. (2013). Yedoma: Late Pleistocene ice-rich syngenetic permafrost of Beringia. In *Encyclopedia of Quaternary Science. 2nd edition* (pp. 542–552). Elsevier.
- Schirrmeister, L., Grosse, G., Kunitsky, V., Magens, D., Meyer, H., Dereviagin, A., Kuznetsova, T., Andreev, A., Babiy, O., & Kienast, F. (2008). Periglacial landscape evolution and environmental

- changes of Arctic lowland areas for the last 60 000 years (western Laptev Sea coast, Cape Mamontov Klyk). *Polar Research*, 27(2), 249–272.
- Schirrmeister, L., Kunitsky, V., Grosse, G., Wetterich, S., Meyer, H., Schwamborn, G., Babiy, O., Derevyagin, A., & Siegert, C. (2011). Sedimentary characteristics and origin of the Late Pleistocene Ice Complex on north-east Siberian Arctic coastal lowlands and islands—A review. *Quaternary International*, 241(1–2), 3–25.
- Schirrmeister, L., Kunitsky, V. V., Grosse, G., Kuznetsova, T. V., Derevyagin, A. Y., Wetterich, S., & Siegert, C. (2008). *The Yedoma Suite of the Northeastern Siberian Shelf Region characteristics and concept of formation*.
- Schirrmeister, L., Schwamborn, G., Overduin, P. P., Strauss, J., Fuchs, M. C., Grigoriev, M., Yakshina, I., Rethemeyer, J., Dietze, E., & Wetterich, S. (2017). Yedoma Ice Complex of the Buor Khaya Peninsula (southern Laptev Sea). *Biogeosciences*, 14(5), 1261–1283. <https://doi.org/10.5194/bg-14-1261-2017>
- Schirrmeister, L., & Wetterich, S. (2020). *TBD*.
- Schneider von Deimling, T., Grosse, G., Strauss, J., Schirrmeister, L., Morgenstern, A., Schaphoff, S., Meinshausen, M., & Boike, J. (2015). Observation-based modelling of permafrost carbon fluxes with accounting for deep carbon deposits and thermokarst activity. *Biogeosciences*, 12(11), 3469–3488.
- Schulte, S., Mangelsdorf, K., & Rullkötter, J. (2000). Organic matter preservation on the Pakistan continental margin as revealed by biomarker geochemistry. *Organic Geochemistry*, 31(10), 1005–1022. [https://doi.org/10.1016/S0146-6380\(00\)00108-X](https://doi.org/10.1016/S0146-6380(00)00108-X)
- Schuur, E. A., Bockheim, J., Canadell, J. G., Euskirchen, E., Field, C. B., Goryachkin, S. V., Hagemann, S., Kuhry, P., Laflour, P. M., & Lee, H. (2008). Vulnerability of permafrost carbon to climate change: Implications for the global carbon cycle. *BioScience*, 58(8), 701–714. <https://doi.org/10.1641/B580807>
- Schwamborn, G., Rachold, V., & Grigoriev, M. N. (2002). Late Quaternary sedimentation history of the Lena Delta. *Quaternary International*, 89(1), 119–134.
- Semiletov, I., Pipko, I., Gustafsson, Ö., Anderson, L. G., Sergienko, V., Pugach, S., Dudarev, O., Charkin, A., Gukov, A., & Bröder, L. (2016). Acidification of East Siberian Arctic Shelf waters through addition of freshwater and terrestrial carbon. *Nature Geoscience*, 9(5), 361–365.
- Sigman, D. M., Casciotti, K. L., Andreani, M., Barford, C., Galanter, M., & Böhlke, J. K. (2001). A Bacterial Method for the Nitrogen Isotopic Analysis of Nitrate in Seawater and Freshwater. *Analytical Chemistry*, 73(17), 4145–4153. <https://doi.org/10.1021/ac010088e>
- Simpson, K. G., Tremblay, J.-É., Gratton, Y., & Price, N. M. (2008). An annual study of inorganic and organic nitrogen and phosphorus and silicic acid in the southeastern Beaufort Sea. *Journal of Geophysical Research: Oceans*, 113(C7).
- Stapel, J. G., Schirrmeister, L., Overduin, P. P., Wetterich, S., Strauss, J., Horsfield, B., & Mangelsdorf, K. (2016). Microbial lipid signatures and substrate potential of organic matter in permafrost deposits: Implications for future greenhouse gas production. *Journal of Geophysical Research: Biogeosciences*, 121(10), 2652–2666.
- Stettner, S., Beamish, A. L., Bartsch, A., Heim, B., Grosse, G., Roth, A., & Lantuit, H. (2018). Monitoring inter-and intra-seasonal dynamics of rapidly degrading ice-rich permafrost riverbanks in the Lena Delta with TerraSAR-X time series. *Remote Sensing*, 10(1), 51.
- Strauss, J., Schirrmeister, L., Mangelsdorf, K., Eichhorn, L., Wetterich, S., & Herzschuh, U. (2015). Organic-matter quality of deep permafrost carbon – a study from Arctic Siberia. *Biogeosciences*, 12(7), 2227–2245. <https://doi.org/10.5194/bg-12-2227-2015>

- Strauss, Jens, & Mann, P. J. (2018). *CACOON-Project-Proposal* (p. 8) [Project Proposal].
- Strauss, Jens, Ogneva, O., Palmtag, J., Aksenov, A., & Fuchs, M. (2019). *CACOON ice: Spring campaign NERC-BMBF project 'Changing Arctic Carbon cycle in the cOastal Ocean Near-shore' (CACOON)* [Expedition Report]. Alfred-Wegener-Institute for Polar and Marine Science.
- Strauss, Jens, Schirrmeister, L., Grosse, G., Fortier, D., Hugelius, G., Knoblauch, C., Romanovsky, V., Schädel, C., Schneider von Deimling, T., Schuur, E. A. G., Shmelev, D., Ulrich, M., & Veremeeva, A. (2017). Deep Yedoma permafrost: A synthesis of depositional characteristics and carbon vulnerability. *Earth-Science Reviews*, *172*, 75–86. <https://doi.org/10.1016/j.earscirev.2017.07.007>
- Strauss, Jens, Schirrmeister, L., Grosse, G., Wetterich, S., Ulrich, M., Herzschuh, U., & Hubberten, H.-W. (2013). The deep permafrost carbon pool of the Yedoma region in Siberia and Alaska. *Geophysical Research Letters*, *40*(23), 6165–6170.
- Strauss, Jens, Schirrmeister, L., Wetterich, S., Borchers, A., & Davydov, S. P. (2012). Grain-size properties and organic-carbon stock of Yedoma Ice Complex permafrost from the Kolyma lowland, northeastern Siberia. *Global Biogeochemical Cycles*, *26*(3).
- Stuiver, M., Reimer, P. J., & Reimer, R. W. (2017). *Calib 7.1 [www program]*.
- Swart, P., Evans, S., & Capo. (2008). *The Origin of Nitrogen Isotope Values in Algae*.
- Tank, S. E., Manizza, M., Holmes, R. M., McClelland, J. W., & Peterson, B. J. (2012). The processing and impact of dissolved riverine nitrogen in the Arctic Ocean. *Estuaries and Coasts*, *35*(2), 401–415. <https://doi.org/10.1007/s12237-011-9417-3>
- Thibodeau, B., Bauch, D., & Voss, M. (2017). Nitrogen dynamic in Eurasian coastal Arctic ecosystem: Insight from nitrogen isotope. *Global Biogeochemical Cycles*, *31*(5), 836–849. <https://doi.org/10.1002/2016GB005593>
- Tuerena, R. E. (2015). *Nitrogen and Carbon Cycling in the South Atlantic Ocean: A stable isotope study along a 40° s transect (UK GEOTRACES)*.
- Van Everdingen, R. (2005). Multi-language glossary of permafrost and related ground-ice terms. National Snow and Ice Data Center/World Data Center for Glaciology, Boulder, CO. *World Wide Web Address: Http://Nsidc. Org/Fgdc/Glossary*.
- Voigt, C., Marushchak, M. E., Lamprecht, R. E., Jackowicz-Korczyński, M., Lindgren, A., Mastepanov, M., Granlund, L., Christensen, T. R., Tahvanainen, T., Martikainen, P. J., & Biasi, C. (2017). Increased nitrous oxide emissions from Arctic peatlands after permafrost thaw. *Proceedings of the National Academy of Sciences*, *114*(24), 6238–6243. <https://doi.org/10.1073/pnas.1702902114>
- Vonk, J. E., & Gustafsson, Ö. (2013). Permafrost-carbon complexities. *Nature Geoscience*, *6*(9), 675–676.
- Vonk, J. E., Mann, P. J., Davydov, S., Davydova, A., Spencer, R. G., Schade, J., Sobczak, W. V., Zimov, N., Zimov, S., & Bulygina, E. (2013). High biolability of ancient permafrost carbon upon thaw. *Geophysical Research Letters*, *40*(11), 2689–2693. <https://doi.org/10.1002/grl.50348>
- Vonk, J. E., Sánchez-García, L., Semiletov, I. P., Dudarev, O. V., Eglinton, T. I., Andersson, A., & Gustafsson, Ö. (2010). Molecular and radiocarbon constraints on sources and degradation of terrestrial organic carbon along the Kolyma paleoriver transect, East Siberian Sea. *Biogeosciences*, *7*(10), 3153–3166.
- Weigand, M. A., Foriel, J., Barnett, B., Oleynik, S., & Sigman, D. M. (2016). Updates to instrumentation and protocols for isotopic analysis of nitrate by the denitrifier method. *Rapid Communications in Mass Spectrometry*, *30*(12), 1365–1383.

- Wetterich, S., Kizyakov, A., Fritz, M., Aksenov, A., Schirrmeister, L., & Opel, T. (2018). *Expedition Report: Permafrost research on Sobo-Sise Island (Lena Delta)*.
- Wetterich, S., Kuzmina, S., Andreev, A. A., Kienast, F., Meyer, H., Schirrmeister, L., Kuznetsova, T., & Sierralta, M. (2008). Palaeoenvironmental dynamics inferred from late Quaternary permafrost deposits on Kurungnakh Island, Lena Delta, northeast Siberia, Russia. *Quaternary Science Reviews*, 27(15–16), 1523–1540.
- Wild, B., Andersson, A., Bröder, L., Vonk, J., Hugelius, G., McClelland, J. W., Song, W., Raymond, P. A., & Gustafsson, Ö. (2019). Rivers across the Siberian Arctic unearth the patterns of carbon release from thawing permafrost. *Proceedings of the National Academy of Sciences*, 116(21), 10280–10285.
- Zaiontz, C. (2013). *Mann-Whitney Test Independent Samples | Real Statistics Using Excel*. <http://www.real-statistics.com/non-parametric-tests/mann-whitney-test/>
- Zhang, T., Heginbottom, J. A., Barry, R. G., & Brown, J. (2000). Further statistics on the distribution of permafrost and ground ice in the Northern Hemisphere. *Polar Geography*, 24(2), 126–131. <https://doi.org/10.1080/10889370009377692>
- Zheng, Y., Zhou, W., Meyers, P. A., & Xie, S. (2007). Lipid biomarkers in the Zoigê-Hongyuan peat deposit: Indicators of Holocene climate changes in West China. *Organic Geochemistry*, 38(11), 1927–1940. <https://doi.org/10.1016/j.orggeochem.2007.06.012>
- Zimov, S. A., Davydov, S. P., Zimova, G. M., Davydova, A. I., Schuur, E. A. G., Dutta, K., & Chapin III, F. S. (2006). Permafrost carbon: Stock and decomposability of a globally significant carbon pool. *Geophysical Research Letters*, 33(20). <https://doi.org/10.1029/2006GL027484>

8 Appendix

8.1 R-Code for Clustering

```
# copy data from excel sheet and load into R:
install.packages("readxl")
library("readxl")
library("BBmisc")
library("rioja")
library("ggplot2")
library("ggfortify")

setwd("...")
data_perma <- read_excel("dataforResults_perma.xlsx", na="NA", sheet = 2)

### Clustering Perma
# normalize data
a<-normalize(data_perma[,3:12],method="standardize",range=c(0,1))
# calculate differences
ad<-dist(a)
# cluster
ac<-chclust(ad,method="coniss")
bstick(ac,7)
# plot dendrogram
plot(ac,hang=-1,xvar=data_perma$depth,horiz=TRUE,x.rev=TRUE)

## Perma samples
#reload data with cluster
data_perma <- read_excel("dataforResults_perma.xlsx", na="NA", sheet = 2)
#boxplot for clustered groups-TOC
boxplot(data_perma$TOC~data_perma$Cluster, main = "Distribution TOC",
        col = (c("darkslategray4","darkslategray")), xlab="Cluster groups",
        cex.axis=1.4, ylab="TOC in wt%")

#boxplot for clustered groups-biomarkers
boxplot(data_perma$[n-alkane]...9~data_perma$Cluster, main = "Distribution Biomarkers",
        col = (c("lightgoldenrod","goldenrod")), xlab="Cluster groups",
        cex.axis=1.4, ylab="absolute n-alkanes in [??g/gSed]")
# Kruskal-Wallis test perma
kruskal.test(data_perma$TOC~data_perma$Cluster)

# Kruskal-Wallis test perma
kruskal.test(data_perma$[n-alkane]...9~data_perma$Cluster)

#CAC19-water
setwd("...")
data_water <- read_excel("CAC19_water.xlsx", na="NA", sheet = 8)

### Clustering Water
# normalize data
b<-normalize(data_water[,5:15],method="standardize",range=c(0,1))
# calculate differences
bd<-dist(b)
# cluster
bc<-chclust(bd,method="coniss")
bstick(bc,10)
# plot dendrogram
plot(bc,hang=-1,xvar=data_water$`sample number`,horiz=TRUE,x.rev=TRUE)
```

```

## Water samples
#reload data with cluster
data_water <- read_excel("CAC19_water.xlsx", na="NA", sheet = 8)
#boxplot for clustered groups-DOC
boxplot(data_water$`DOC [µg/l]`~data_water$Cluster, main = "Distribution DOC", cex.main = 2,
        col = (c("snow3", "snow4")), xlab="Cluster groups",
        cex.axis=1.4, ylab="Dissolved Organic Carbon in [µg/l]")

#boxplot for clustered groups-DON
boxplot(data_water$`DON [µg/l]`~data_water$Cluster, main = "Distribution DON", cex.main = 2,
        col = (c("slategray3", "slategray4")), xlab="Cluster groups",
        cex.axis=1.4, ylab="DON in [µg/l]")

#boxplot for clustered groups-NO3
boxplot(data_water$`[NO3] µg/l`~data_water$Cluster, main="Distribution Nitrate", cex.main=2,
        col = (c("wheat3", "wheat4")), xlab="Cluster groups",
        cex.axis=1.4, ylab="NO3- in [µg/l]")
#boxplot for clustered groups-TDN
boxplot(data_water$`[TDN] µg/l`~data_water$Cluster, main = "Distribution TDN", cex.main = 2,
        col = (c("wheat3", "wheat4")), xlab="Cluster groups",
        cex.axis=1.4, ylab="NO3- in [µg/l]")

##Isotopes
#boxplot for clustered groups-d15N-no3
boxplot(data_water$`d15N-NO3`~data_water$Cluster, main = "Distribution δ15N-NO3-", cex.main = 2,
        col = (c("darkseagreen3", "darkseagreen4")), xlab="Cluster groups",
        cex.axis=1.4, ylab="δ15N-NO3- in ‰")

#boxplot for clustered groups-d15N-DON
boxplot(data_water$`d15N-DON`~data_water$Cluster, main = "Distribution δ15N-DON", cex.main = 2,
        col = (c("mistyrose3", "mistyrose4")), xlab="Cluster groups",
        cex.axis=1.4, ylab="δ15N-DON in ‰")

#boxplot for clustered groups-d18O-no3
boxplot(data_water$`d18O-NO3`~data_water$Cluster, main = "Distribution δ18O-NO3-", cex.main = 2,
        col = (c("lightsalmon3", "lightsalmon4")), xlab="Cluster groups",
        cex.axis=1.4, ylab="δ18O-NO3- in ‰")

#boxplot for clustered groups-d15N-TDN
boxplot(data_water$`d15N-TDN`~data_water$Cluster, main = "Distribution δ15N-TDN", cex.main = 2,
        col = (c("paleturquoise3", "paleturquoise4")), xlab="Cluster groups",
        cex.axis=1.4, ylab="δ15N-TDN in ‰")

```

8.2 n-alkane parameters

Sample ID	depth	median age	modelled Bacon age	TOC	TN	C/N	d ¹³ C	[n-alkane]	[n-alkane]	ACL	CPI	Max [n-alkanes]	Main chain	Assigned Cluster
	<i>m arl</i>	<i>cal BP</i>	<i>cal BP</i>	<i>wt%</i>	<i>wt%</i>		<i>‰</i>	<i>µg/gSed</i>	<i>µg/gTOC</i>	<i>(n-alkanes)</i>	<i>(n-alkanes)</i>	<i>µg/gSed</i>		
SOB18-01-01	24.1		500	25.51	0.83	30.55	-28.04	34.12	133.75	26.05	12.52	10.47	29	I
SOB18-01-03	23.2	4443	4440	9.73	0.71	13.78	-27.76	49.08	504.52	24.78	8.65	11.69	29	I
SOB18-01-04	22.7	6373	6360	6.88	0.46	14.94	-28.32	28.21	410.01	27.29	11.43	8.28	31	I
SOB18-01-06	21.7		16028	4.11	0.30	13.55	-26.87	33.83	822.33	26.26	11.09	11.69	27	I
SOB18-01-08	20.7		20419	1.24	0.15	8.24	-25.58	4.56	366.12	25.68	8.70	1.12	27	I
SOB18-01-10	19.7	21935	21819	1.34	0.16	8.24	-25.69	10.94	816.65	26.30	10.71	3.26	27	I
SOB18-01-12	18.7		22836	0.82	0.11	7.20	-25.22	1.79	217.77	26.33	7.23	0.41	29	I
SOB18-01-14	17.7		24203	1.24	0.14	8.66	-25.75	3.87	311.41	25.88	6.66	0.94	29	I
SOB18-01-16	16.7		25876	2.84	0.22	12.97	-26.17	11.61	409.49	26.17	11.16	3.71	27	I
SOB18-01-18	15.7	27544	27555	< 0.1	< 0.1	na	na	1.46	1455.49	na	5.76	0.31	29	I
SOB18-03-03	17.2		28406	3.94	0.31	12.71	-27.16	4.80	121.98	26.51	11.09	1.25	29	I
SOB18-03-05	16.2		37176	11.31	0.58	19.42	-29.43	31.23	276.21	26.21	15.86	8.27	27	I
SOB18-03-07	15.2	38262	38119	3.68	0.28	13.16	-26.02	10.43	283.35	26.85	10.74	2.57	29	I
SOB18-03-09	14.2		38878	3.80	0.34	11.32	-26.15	10.15	267.38	26.84	9.30	2.62	29	I
SOB18-03-11	13.2		39641	7.03	0.53	13.22	-27.48	58.16	827.55	26.83	11.36	13.55	31	II
SOB18-06-01	13.4	41419	41449	3.98	0.26	15.27	-28.25	74.98	1886.10	26.19	9.95	16.23	29	II
SOB18-06-03	12.5		42534	3.68	0.30	12.29	-28.16	68.73	1868.68	25.80	8.69	15.60	29	II
SOB18-06-05	11.5	43534	43306	3.55	0.28	12.87	-27.97	107.55	3029.59	27.25	16.29	28.44	27	II
SOB18-06-07	10.5	44127	44079	3.97	0.29	13.93	-26.44	93.30	2349.04	26.38	10.71	29.20	27	II
SOB18-06-09	9.5		44815	6.95	0.53	13.19	-27.55	56.83	817.84	26.27	13.69	13.85	29	II
SOB18-06-11	8.5		45536	6.12	0.47	13.15	-28.48	103.91	1698.14	26.44	13.06	35.17	27	II
SOB18-06-13	7.5		46223	5.74	0.37	15.63	-27.89	55.48	965.90	25.65	9.67	13.96	27	II
SOB18-06-15	6.5		46832	3.74	0.27	14.03	-28.38	64.71	1729.35	24.53	6.09	15.35	27	II
SOB18-06-17	5.5		47635	3.42	0.30	11.26	-26.44	28.66	837.17	23.68	6.34	6.77	31	II

Sample ID	depth	median age	modelled Bacon age	TOC	TN	C/N	d ¹³ C	[n-alkane]	[n-alkane]	ACL	CPI	Max [n-alkanes]	Main chain	Assigned Cluster
	<i>m arl</i>	<i>cal BP</i>	<i>cal BP</i>	<i>wt%</i>	<i>wt%</i>		<i>‰</i>	<i>µg/gSed</i>	<i>µg/gTOC</i>			<i>µg/gSed</i>		
SOB18-06-19	4.5		48455	3.61	0.33	11.10	-25.98	57.55	1592.88	26.82	8.62	15.72	31	II
SOB18-06-30	3.2	48899	49555	5.64	0.40	13.94	-27.39	43.12	765.23	24.08	7.34	9.51	27	II
SOB18-06-32	2.2		50564	1.95	0.19	10.34	-27.30	66.13	3386.23	23.31	7.03	14.24	27	II
SOB18-06-34	1.4		51371	2.51	0.20	12.46	-27.84	64.96	2591.35	23.14	7.05	14.23	27	II
MEAN		30726.22	34093.21	5.12	0.34	13.24	-27.17	42.15	1097.91	25.83	9.89	11.02	28	
MAX		48899	51371	25.51	0.83	30.55	-25.22	107.55	3386.23	27.29	16.29	35.17	31	
MIN		4443	500	0.82	0.11	7.20	-29.43	1.46	121.98	23.14	5.76	0.31	27	

8.3 n-fatty acid parameters

Sample ID	depth	Modelled Bacon age	TOC	[n-fatty acids]	[n-fatty acids]	Max [n-fatty acids]	main chain (n-fatty acids)	HPFA (n-fatty acids)	ACL (n-fatty acids)
	<i>m arl</i>	<i>cal BP</i>	<i>wt%</i>	<i>µg/gSed</i>	<i>µg/gTOC</i>	<i>µg/gSed</i>	<i>manually</i>	<i>µg/gSed</i>	
SOB18-01-01	24.1	500	25.51	183.63	719.79	183.63	C24	0.72	25.08
SOB18-01-03	23.2	4440	9.73	190.96	1962.82	190.96	C22	0.61	25.28
SOB18-01-04	22.7	6360	6.88	290.39	4220.93	290.39	C24	0.86	24.83
SOB18-01-10	19.7	21819	1.34	42.95	3206.32	42.95	C24	0.74	25.03
SOB18-01-16	16.7	25876	2.84	37.36	1317.52	37.36	C26	0.67	25.27
SOB18-03-05	16.2	37176	11.31	185.88	1643.86	185.88	C16	0.68	24.81
SOB18-03-11	13.2	39641	7.03	124.03	1764.95	124.03	C24	0.53	24.95
SOB18-06-03	12.5	42534	3.68	93.91	2553.19	93.91	C24	0.49	25.11
SOB18-06-09	9.5	44815	6.95	170.19	2449.14	170.19	C24	0.57	24.94
SOB18-06-13	7.5	46223	5.74	34.27	596.60	34.27	C24	0.25	25.05
SOB18-06-17	5.5	47635	3.42	56.65	1654.81	56.65	C16	0.45	24.57
SOB18-06-30	3.2	49555	5.64	115.72	2053.54	115.72	C24	0.65	25.08
SOB18-06-34	1.4	51371	2.51	117.42	4683.99	117.42	C24	0.60	25.10
MEAN			7.12	126.41	2217.50	126.41		0.60	25.01
MAX			25.51	290.39	4683.99	290.39	26.00	0.86	25.28
MIN			1.34	34.27	596.60	34.27	16.00	0.25	24.57

8.4 n-alkohol parameters

Sample ID	[n-alkohols]	[n-alkohols]	Max [n-alkohols]	main chain - alcohols	[n-sterols]	[n-sterols]	Max [n-sterols]	max n-sterol component
	<i>µg/gSed</i>	<i>µg/gTOC</i>	<i>µg/gSed</i>	<i>manually</i>	<i>µg/gSed</i>	<i>µg/gTOC</i>	<i>µg/gSed</i>	<i>manually</i>
SOB18-01-01	129.28	506.75	33.72	C26	181.96	713.24	121.78	α -Sitosterol
SOB18-01-03	534.19	5490.87	134.39	C26	278.85	2866.26	211.37	α -Sitosterol
SOB18-01-04	76.85	1117.09	15.45	C26	45.64	663.41	31.44	α -Sitosterol
SOB18-01-10	34.44	2571.06	9.96	C30	1.58	117.85	1.14	α -Amyrin
SOB18-01-16	31.89	1124.34	11.08	C26	25.28	891.50	20.38	α -Sitosterol
SOB18-03-05	126.83	1121.60	34.88	C28	67.65	598.26	46.07	α -Sitosterol
SOB18-03-11	46.36	659.66	15.79	C28	8.99	127.92	8.99	α -Sitosterol
SOB18-06-03	57.74	1569.67	16.63	C28	9.13	248.30	7.41	α -Sitosterol
SOB18-06-09	73.32	1055.10	22.46	C28	6.04	86.86	2.45	α -Sitosterol
SOB18-06-13	61.23	1066.16	21.24	C28	12.94	225.34	10.17	α -Sitosterol
SOB18-06-17	29.76	869.25	7.61	C26	14.03	409.66	13.06	α -Sitosterol
SOB18-06-30	31.73	563.12	9.82	C28	6.15	109.15	5.59	α -Sitosterol
SOB18-06-34	36.00	1436.04	9.91	C28	10.39	414.60	5.66	α -Sitosterol
MEAN	97.66	1473.13	26.38	28.00	51.43	574.80	37.35	
MAX	534.19	5490.87	134.39	30.00	278.85	2866.26	211.37	α -Sitosterol
MIN	29.76	506.75	7.61	26.00	1.58	86.86	1.14	

8.5 Water parameters, nitrogen species and nitrogen stable isotopes

BDL – below detection limit, EX – excluded from further analysis

Nr	Station	Sample name	Longitude	Latitude	Sample depth	Temperature	Salinity	DOC	[NO ₃]	[TDN]	DON	δ ¹⁵ N-NO ₃ ⁻	SD	δ ¹⁸ O-NO ₃ ⁻	SD	δ ¹⁵ N-TDN	SD	Assigned cluster
					<i>m bsl</i>	°C	<i>PSU</i>	<i>µg/l</i>	<i>µg/l</i>	<i>µg/l</i>	<i>µg/l</i>							
1	CAC19-H	CAC19-H-3	128.23865	72.56407	3.0	0.11	20.81	6017.00	822.57	258.54	72.80	3.27	0.16	-12.96	0.36	3.05		I
2	CAC19-G	CAC19-G-7.5	128.35324	72.53542	7.5	0.09	20.79	6082.50	609.59	191.78	54.13	3.14	0.12	-13.15	0.05	2.84		I
3	CAC19-F	CAC19-F-3	128.49216	72.51871	3.0	2.17	25.04	8544.00	264.35	211.02	3700.84	2.25	0.18	-12.72	0.34	<i>EX</i>		I
4	CAC19-E	CAC19-E-2.5	128.62968	72.50182	2.5	0.13	19.39	5824.00	505.81	166.14	51.92	3.17	0.10	-12.99	0.11	1.62	0.79	I
5	CAC19-D	CAC19-D-10	128.69456	72.46153	10.0	0.05	20.48	6411.33	451.47	179.02	77.08	3.12	0.20	-12.91	0.07	2.98		I
6	CAC19-C	CAC19-C-2	128.84447	72.45562	2.0	0.03	21.07	6125.00	447.74	406.89	305.78	3.44	0.09	-12.66	0.10	2.69	0.72	I
7	CAC19-B	CAC19-B-5	128.97108	72.47939	5.0	0.02	20.70	6015.00	781.12	267.08	90.70	3.54	0.00	-12.68	0.03	3.07		I
8	CAC19-A	CAC19-A-7	129.10159	72.50127	7.0	0.06	20.59	6041.33	615.97	564.70	425.61	3.41	0.53	-12.47	1.08	1.89		I
9	CAC19-01	CAC19-01-6	129.24791	72.50908	6.0	0.07	20.66	6167.67	6.20	122.30	120.90	<i>BDL</i>		<i>BDL</i>		2.10		I
10	CAC19-02	CAC19-02-2.6	129.54568	72.51685	2.6	0.06	19.57	7302.00	388.08	412.98	325.35	3.30	0.47	-12.44	0.88	2.08	0.06	II
11	CAC19-23	CAC19-23-2.3	129.69305	72.52135	2.3	0.13	21.27	6114.00	473.56	586.71	479.78	3.50	0.08	-12.51	0.41	<i>EX</i>		II
12	CAC19-03	CAC19-03-3	129.84203	72.52538	3.0	0.05	21.14	6023.00	22.51	205.38	200.29	<i>BDL</i>		<i>BDL</i>		2.92		II
13	CAC19-04	CAC19-04-3	129.86385	72.52548	3.0	0.10	21.06	6609.00	37.04	127.63	119.27	<i>BDL</i>		<i>BDL</i>		1.20	0.31	II
					MEAN	0.24	20.97	6405.83	417.39	284.63	190.38	3.21		-12.75		2.40		
		Excl CAC19-F			4.49	0.08	20.63	6227.65	430.14	290.76	193.63							
					MIN	0.02	19.39	5824.00	6.20	122.30	51.92	2.25		-13.15		1.20		
					MAX	0.13	21.27	7302.00	822.57	586.71	479.78	3.54		-12.44		3.07		

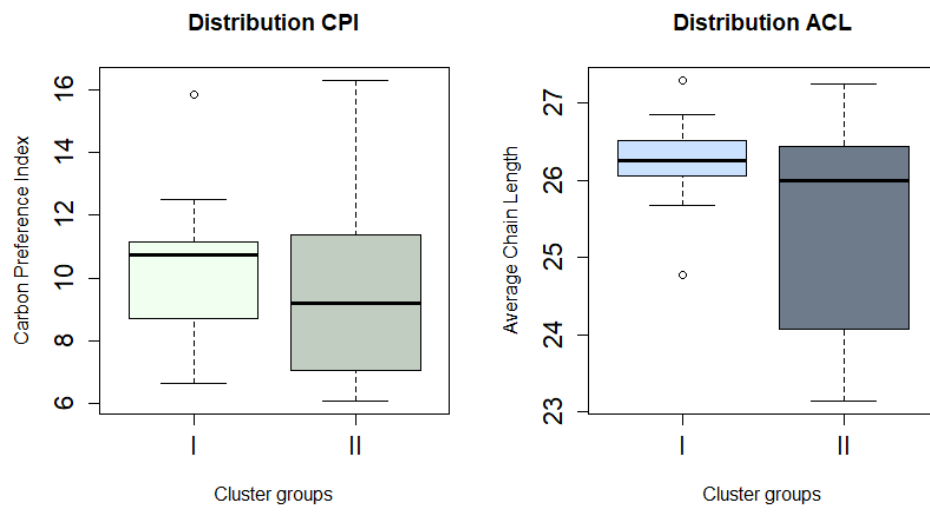
8.6 Stable Water isotope data

Raw data for **Ice melt water input** and **Groundwater input**.

Sample depth	sample number	Station	Processed Delta 2H	Processed Delta 18O	Processed Delta 17O	Deuterium excess
<i>m brl</i>			‰	‰	‰	‰
3	3	CAC19-F	-159.00	-21.31	-11.17	11.47
2	6	CAC19-C	-159.80	-21.30	-11.10	10.60
7	8	CAC19-A	-159.37	-21.19	-11.06	10.17
6	9	CAC19-01	-158.58	-21.16	-11.07	10.69
2.6	10	CAC19-02	-158.97	-21.18	-11.14	10.48
2.3	11	CAC19-23	-158.80	-21.07	-11.09	9.73
3	12	CAC19-03	-158.75	-21.17	-11.09	10.59
3	13	CAC19-04	-158.86	-21.05	-11.11	9.58
		MEAN	-159.80	-21.31	-11.17	9.58
		MAX	-158.58	-21.05	-11.06	11.47
		MIN	-159.01	-21.18	-11.10	10.41

Sample depth	sample number	Station	Processed Delta 2H	Processed Delta 18O	Processed Delta 17O	Deuterium excess
<i>m brl</i>			‰	‰	‰	‰
2.5	4	CAC19-E	-159.54	-21.17	-11.13	9.79
10	5	CAC19-D	-158.61	-21.16	-11.06	10.64
3	1	CAC19-H	-158.99	-21.18	-11.08	10.43
7	2	CAC19-G	-158.76	-21.16	-11.11	10.56
5	7	CAC19-B	-159.27	-21.10	-11.08	9.51
		MEAN	-159.03	-21.15	-11.09	10.19
		MAX	-158.61	-21.10	-11.06	10.64
		MIN	-159.54	-21.18	-11.13	9.51

8.7 Distribution CPI and ACL over cliff height in cluster groups



9 Certificate of good Conduct

I declare that I have authored this thesis independently, that I have not used other than the declared sources/references and that I have explicitly marked all material which has been quoted either literally or by content from the used sources.

Images or figures have been either created independently or marked with a respective reference.

Furthermore I declare that this thesis has not been submitted for any other exam.

Potsdam, 28.06.2020,

A handwritten signature in black ink, appearing to be 'C. J. B.', written on a light-colored background.

Eidesstattliche Erklärung zur Masterarbeit

Ich versichere, diese Arbeit selbständig und lediglich unter Benutzung der angegebenen Quellen und Hilfsmittel verfasst zu haben.

Alle Stellen, die wörtlich oder sinngemäß aus veröffentlichten oder noch nicht veröffentlichten Quellen entnommen sind, sind als solche kenntlich gemacht.

Die Zeichnungen oder Abbildungen in dieser Arbeit sind von mir selbst erstellt worden oder mit einem entsprechenden Quellennachweis versehen.

Ich erkläre weiterhin, dass die vorliegende Arbeit noch nicht im Rahmen eines anderen Prüfungsverfahrens eingereicht wurde.

Potsdam, den 28.06.2020,

A handwritten signature in black ink, appearing to be 'C. J. B.', written on a light-colored background.

10 Acknowledgements

This master's thesis was carried out at the Alfred-Wegener-Institute in Potsdam. First of all, I would like to thank all my colleagues of the Permafrost Research Section at the AWI Potsdam for making the thesis and everything around it possible.

I thank my supervisor Jens Strauss for listening to my big and small problems and carefully directing me towards a wiser path. Also, my second supervisor Guido Grosse who supported me all the way. I am grateful to you both for the scientific discussions and enriching my knowledge.

I thank Lutz Schirrmeister and Sebastian Wetterich from AWI Potsdam for the cooperation with Sobo Sise samples as well as the sedimentary data later on, not to forget Aleksander Kizyakov, for repelling down Sobo Sise Cliff and retrieving the terrestrial samples in the first place. Also from AWI, I want to give special thanks to my biomarker-mentor Loeka Jongejans, without her guidance I would not have found the magic key to the world of biomarkers. Thank you for all the conversations and support with calculations.

Writing this thesis as a part of the CACOON project has not only been a privilege but also a great opportunity for me. Taking part in conferences and being able to present my work in an international audience has been of great value personally and to my thesis. CACOON is a German-British co-funded project within the Changing Arctic Ocean project by NERC and BMBF (#03F0806A). Within CACOON, I thank Paul Mann and Juri Palmtag from Northumbria University in Newcastle, UK who made the initial contact to Edinburgh and most of all the sample transport possible and helped with interpretation of the results. Further Matthias Fuchs who helped me with maps and shared vital information with me. I am grateful for all members of the CACOON on Ice Expedition 2019 who collected the water samples in the field.

Also I thank the nitrogen-isotope-guru Robyn Tuerena from Edinburgh University, where the major part of the stable nitrogen isotope analysis took place within the Oceans Research group at the Edinburgh Global Change Research Institute under the supervision of Raja Ganeshram. I want to give thanks my office mates Adam Francis, Antonia Doncila and Margot Debyser in Edinburgh for helping me in the lab and with understanding the link between nitrogen processes and stable isotope geochemistry.

The lipid biomarker analysis took place at GFZ laboratories of section 3.2 Organic Chemistry in Potsdam under supervision of Kai Mangelsdorf. Here, I want to especially thank Anke Kaminsky and Cornelia Karger from the GFZ laboratory for assisting with all the laboratory work and making biomarkers more accessible to me.

Finally, I thank my loving friends and family who cared for me and always supported me. I especially thank Frederic for your universal positive energy and for all the adventures we got to and will experience together.